Plate Tectonics, Mantle Convection and D” Seismic Structures

Thesis by

Lianxing Wen

In Partial Fulfillment of the Requirements
for the Degree of
Doctor of Philosophy

California Institute of Technology
Pasadena, California

1998
(Submitted January 15, 1998)

Acknowledgements

My stay at Caltech has been the turning point of my professional and personal life. I am grateful to the Seismo Lab students, faculty and staff for creating such a wonderful research environment. The Seismo Lab has constantly been the source of help, inspiration and encouragement to me.

Along the way of my study, I am indebted to the Seismo Lab faculty and staff for their help. I would like to express my deepest gratitude to my thesis advisors: Don L. Anderson and Donald V. Helmberger. They are great teachers and have been very supportive in every way possible and provided thoughtful guidance. They shaped me as a scientist in a variety of ways. I also benefited tremendously from my academic advisor Rob Clayton for his good advice on taking courses and assistance in the finite difference code and from Michael Gurnis and David Stevenson for their encouragement and constructive criticism. Discussions with Hiroo Kanamori, Joann Stock, Tom Ahrens, Mark Simons and Tom Heaton were also very helpful. I would also like to thank the Seismo Lab staff, particularly Gayle Hampton and Evelina Cui.

I also benefited enormously from discussions and assistance from other fellow students and postdocs in the Seismo Lab. Among them are: Weishi Huang, Xiaodong Song, Shingo Watada, Wenbo Yang, Xi Song, Xiaoming Ding, Guangqing Chen, Ed Garnero, Lupei Zhu, Laura Jones, Monica Kohler, Tim Melbourne. Special thanks go to Lian-she Zhao, the big "brother," Craig Scrivner, Shijie Zhong and my officemates. Lian-she helped me to settle down; Craig has been very helpful in many aspects of my research; Shijie inspired me in many ways; my officemates: Igor Sidorin, Bill Keller, Deborah Dauger, Jane Heinemann, Hong-kie Thio, Jascha Polet and Blair Zajac brought fun to my daily life. I would also like to thank Zhenxing Yao for introducing me to Caltech.

Finally, I dedicate this thesis to my wife, Mei-Lan. She has been unfailingly supportive and very understanding of the inevitable disruptions to family life.

Abstract

This thesis is directed at understanding dynamics of the Earth's mantle. I adopt multidisciplinary approaches toward the problem: geodynamical and seismological.

My approach in geodynamics is directed at understanding the relationship between large scale surface observables (geoid, topography, plate motions) and mantle rheology and convection of the present-day Earth. In chapter 2, I do best-fit correlations of shallow mantle structure with various tectonic features and remove them to generate what we call "residual tomography." In chapter 3, I show that the pattern, spectrum and amplitude of the "residual topography" are consistent with shallow origin of the "Earth surface dynamic topography;" the very long wavelength geoid and topography ($l = 2 - 3$) are successfully explained by density models inferred from the "residual tomography," assuming layered mantle convection stratified at the "920 km seismic discontinuity." In chapter 4, I develop a new method to calculate mantle flow in the spherical coordinates with lateral variation of viscosity. The viscosity contrast between continental and oceanic regions is identified to have dominating effects on both the observed poloidal/toroidal ratio and pattern of toroidal motions at long wavelengths. I show convection models with lateral variation of viscosity are capable of producing long wavelength plate motions observed in plate tectonics.

My approach in seismology is focused on exploring fine structures near the core-mantle boundary and developing new techniques for computing synthetic seismograms. I discuss the method development and strategies to explore fine structures near the core-mantle boundary region in the following chapters. In chapter 5, I develop a hybrid method which can handle the seismic wave propagation in heterogeneous regions at large distances. The hybrid method is a combination of analytical and numerical methods, with numerical methods applied in heterogeneous regions only and analytical methods outside. In chapter 6, I discuss wave propagation of SKS and SPdKS phases through ultra-low velocity zones near the core-mantle boundary and constrain the general structures of ultra low velocity zones near the core-mantle boundary under Fiji subduction zone and Iceland. The long period SKS-SPdKS data are explained by ultra low velocity zones with P velocity reduction of 10% and horizontal length scales of about 250 km and height of about 40 km. S velocity reduction of 30% is consistent with the data, although the trade-offs between S velocity reduction and height of the structure exist. In chapter 7, I discuss wave propagation of PKP and its precursors and constrain the detailed structures of the ultra low velocity zones near the core-mantle boundary from observed broadband PKP precursors. The observed long period precursors are explained by the existence of ultra low velocity zones with P velocity reduction of at least 7% and horizontal length scales of 100-300 km and height of about 60-80 km, whereas short period precursors suggest that the structures have smooth edges and structures with smaller scale are adjacent to these large Gaussian-shaped structures. These fine structures may be indicatives of vigorous small-scale convection or the instabilities of the bottom thermal boundary layer of the mantle.

Contents

List of Figures

List of Tables

Chapter 1 General introduction

Understanding the dynamics of Earth can be approached geodynamically and seismologically. Figure 1.1 summarizes the ideas in this thesis to approach the problem.

In the time scale of millions of years and length scale of thousands of kilometers, Earth can be treated as a viscous body (Figure 1.1a). Mantle convection causes lateral variations of chemistry and temperature in the mantle and those lateral variations produce density anomalies which eventually drive mantle convection and produce signatures observable at the surface of Earth, such as, geoid, topography, plate motions, intra-plate stresses, sea level change and true polar wander (Figure 1.1a). This thesis addresses some of those observables: geoid, topography and plate motions. Geoid at the surface of Earth is a combination of effects of density anomalies in the mantle and mass anomalies due to the deformations, the so-called "dynamic topography," at various chemical boundaries of Earth. So, geoid and topography place strong constraints on mantle rheology and convection, and they must be explained by a convection model before we claim that we have a self-consistent model. Plate motions not only place important constraints on the absolute value and lateral variation of mantle viscosity, but also bring out the question about the complexity of mantle convection system. Understanding those surface signatures is crucial to understanding mantle convection and those surface signatures must be used to test against predictions from convection models. Although modeling time-dependent mantle convection is our ultimate goal in geodynamics, it is important, in the first order, to understand the behaviors of the present-day Earth, not only because the present-day Earth is constrained by seismological and geodynamical observations but also because the present-day Earth holds the key to the past of Earth.

Those surface observables of the present-day Earth can be related to the interior density anomalies of the present-day Earth by instantaneous flow, simply because the time scale for the chemical boundaries to response the density anomalies is much

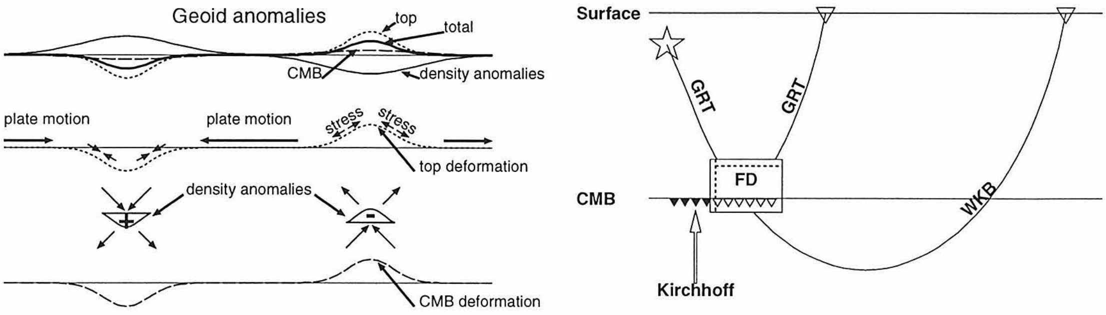

(a) Cartoon illustrating geodynamical approach. Density anomalies produce deformation, stress, plate motions and geoid, which are observable at the surface of Earth. Thus, these surface observables can be used to constrain the dynamics of Earth. The geoid anomalies are the summations of contribution from density anomalies themselves and that from mass anomalies due to the deformations of various chemical boundaries.

(b) The interfaces of hybrid method for calculating synthetic seismograms. Finite-difference (FD) is applied in the heterogeneous region (box). Generalized ray theory (GRT), WKB, and Kirchhoff theory are used outside. The source-side output in positions represented by filled triangles is calculated by GRT and that in positions represented by empty triangles is obtained from FD. This technique allows high resolution study of localized structures.

Figure 1.1: Illustration of geodynamical and seismological approaches.

smaller than that for the density anomalies to significantly change their locations. For example, for a viscous half space of viscosity η and density ρ and traction free surface at the top, the deformation at the surface (δz) caused by a density contrast $\sigma(k)cos(kx)$ at depth d is:

$$\delta z = -\frac{\sigma(k)cos(kx)}{\rho}(1+kd)exp(-kd)(1-e^{-t/\tau}) \tag{1.1}$$

τ is the relaxation time and

$$\tau = 2\eta k/\rho g \tag{1.2}$$

With $\eta = 10^{21}$ Pa s, $g = 10$ m/s^2, $\rho = 3.5$ Mg/m^3, $\tau \leq$ 11,000 yrs for small k (for example, $2\pi/1000$km) and the density anomalies will move less than 1.1 km in this time scale, assuming a flow velocity of 10 cm/yr.

The difficulty of modeling dynamic topography lies in the complexities of shallow mantle structure and the difficulty of modeling plate motions lies in the lack of knowledge about lateral variation of mantle viscosity and of techniques for modeling mantle flow with lateral variation of viscosity. All these issues will be addressed in this thesis.

On the other hand, in the time scale of seconds or years and length scale of seismic wave lengths, Earth can be treated as an elastic body. Complementary to the observables at the surface of Earth, the characteristics of the core-mantle boundary region bear very important information on geodynamics and mineralogy. Seismology is the only tool for revealing the structures in this particular region. Various observations of very small scale seismic structures in the core-mantle boundary region (scattering of PcP, ScS, precursors to PKP, complexity of SKS-SPdKS, *etc.*) and the accumulation of broadband data require new techniques for modeling seismic wave propagation through such fine structures. The length scale, magnitude and geometry of those fine seismic structures have important implications to mineralogy and geodynamics and the topographic reliefs of the core-mantle boundary place important constraints on mantle and core dynamics.

Both analytical and numerical methods have difficulties in handling the wave propagation through such fine structures (including topographic reliefs). Analytical methods have the advantages that they require little computer memory and computation time, but they are basically limited to applications to one-dimensional models. On the other hand, numerical methods can handle the wave propagation through heterogeneous regions, but they require massive computer memory and are limited to wave propagation of small distances and low frequency modelings. The calculations of seismic wave propagation through these fine structures can be implemented by combining the advantages of both analytical and numerical methods. Figure 1.1b shows the idea of hybrid method, where numerical finite-difference technique is applied in the heterogeneous regions only. How is the hybrid method developed? What strategies can we adpot to explore fine structures in the core-mantle boundary region? How does the existence of the ultra low velocity zones affect the wave propagations of SKS, SPdKS, SKPdS and PKP phases? How can we use the waveforms of those phases to constrain the scale, magnitude and geometry of fine structures near the core-mantle boundary? What are the geodynamical and mineralogical implications of those fine strucutres? All these issues will be addressed in this thesis.

Chapter 2 Slabs, hotspots, cratons and mantle convection revealed from residual seismic tomography in the upper mantle

2.1 Abstract

We calculate residual tomographic maps in the upper mantle by excluding from the tomography the first order effects of conductive cooling of oceanic plates, deep cratonic "roots," and cooling or partial melting associated with subducted lithosphere. No correlation is found between residual tomography in the upper mantle and the 30-130 Ma subduction. The good correlations between residual tomography in the transition zone (400-650 km) with 0-30 Ma subduction, at spherical harmonic degree l=2 can be explained either by slab accumulation in transition zone beneath some subduction zones, or by the poor lateral resolution of seismic tomography. Hotspots correlate with the residual tomography in the shallow (100-400 km) and the lowermost mantle at degree l=2. However, correlations of hotspots and seismic velocities in the middle mantle, and correlations between residual tomography at shallow depths and lowermost mantle tomography are poor. Therefore, the connection between residual tomography at shallow depths and seismic tomography in the lowermost mantle is not clear. There is an interesting correlation between craton distribution, distribution of hotspots and residual topography. This might indicate that cratonic "roots" affect the locations of upwellings and thus modulate upper mantle convection, or that cratons and other near-surface features control the platform of convection in the mantle.

2.2 Introduction

The relationship between subduction and seismic tomography has been studied extensively. *Richards and Engebretson* [1992] interpreted the good correlations between the large-scale seismic heterogeneity, averaged over the whole lower mantle, and subduction during the Cenozoic and Mesozoic as the result of the cooling effects of the subduction. *Scrivner and Anderson* [1992] correlated subduction positions since the breakup of Pangea, with seismic tomography depth by depth throughout the whole mantle. They found correlations in the transition zone region. *Ray and Anderson* [1994] found good correlations between integrated slab locations since the breakup of Pangea and fast velocities in the depth range 220-1022 km. *Wen and Anderson* [1995] quantified the slab flux by estimating the subducted volume in the hotspot reference frame and correlated it with seismic tomography throughout the mantle. They found significant correlations in the depth interval 800-1100 km and attributed these to the accumulation of subducted lithosphere in this region. Correlations were also found in the upper mantle and transition zone for recent subduction.

The relationship between hotspots and seismic tomography has also been investigated. Excellent correlations at degree $l=2$ were found in the lower mantle and, at degree $l=6$ in the upper mantle [*Richards et al.*, 1988; *Cazenave et al.*, 1989; *Kedar et al.*, 1993]. *Cazenave et al.* [1989] interpreted their results in terms of degree 2 convection in the lower mantle and degree 6 dominated convection in the upper mantle. *Richards et al.* [1988] hypothesized that hotspots originated in the deep lower mantle, based on the good correlations at degree 2, whereas *Montagner and Romanowicz* [1993] speculated that hotspots came from the transition zone, based on the dramatic decrease in the correlation below the transition zone, at degree 6.

One of the difficulties in relating tomography in the upper mantle with subduction and hotspots is the complexity and multiple causes of lateral velocity changes in this region. Large contributions from the cooling of the oceanic plates and cratonic "roots" make it difficult to get meaningful results from the hotspot and slab correlations with the seismic tomography. The role of deep cratonic "roots" in the upper mantle has been extensively discussed [*Lerner-Lam and Jordan*, 1987; *Hara and Geller*, 1994; *Polet and Anderson*, 1995]. The contribution from downgoing slabs, or possible stagnant slabs, may also prevent one from correctly relating seismic tomography to hotspots.

One can extract geodynamical information from seismological data in various ways. One method is to introduce an *a priori* regionalization of the upper mantle and use data to infer the parameters [e.g., *Toksoz and Anderson*, 1966; *Nataf et al.*, 1986; *Nataf and Ricard*, 1996]. Another way is to separate out the effects of near-surface features from the current generation of seismic tomographic models [e.g., *Forte et al.*, 1995]. *Forte et al.* [1995] decomposed seismic tomography into "correlated" and "uncorrelated" components with respect to the continent-ocean function, but other contributions may also be mapped into the "correlated" component if these contributions are not totally "uncorrelated" with the continent-ocean function. In this paper, recognizing problems of coverage, resolution and radial smearing, we test a current tomographic model for its geodynamic content. We construct residual tomographic maps for the upper mantle by excluding effects of conductive cooling of oceanic plates, cratonic "roots," and the cooling or partial melting associated with downgoing slabs. It is of interest to see if useful geodynamic information can be extracted from the current generation of seismic tomographic models. The residual tomography is compared with the pattern of subduction history in the past 130 Ma [*Wen and Anderson*, 1995] and with the distribution of hotspots. The procedures for excluding these effects are given in the first section. The correlation between residual tomography and past subduction is presented in the second section. The relationship between the distribution of hotspots and residual tomography and distribution of cratons is discussed in the third section.

2.3 Residual upper mantle tomographic models

The first order contributors to seismic tomography in the upper mantle are assumed to be oceanic plates, cratonic "roots," and on-going subduction. Other possible contributors, such as hotspots, stagnant slabs, and small scale mantle convection are assumed to be second order. If they are important, they may show up in the residual maps. The residual tomography is defined as the seismic tomography excluding the effects of the first order contributors. We use the seismic tomographic model SH12WM13 [*Su et al.*, 1994].

2.3.1 Oceanic plates

Our first job is to remove from the tomographic models the effects of the cooling of oceanic plates. Velocity heterogeneities can be related to temperature variation of the mantle by the temperature derivatives for the minerals in the mantle. The temperature distribution beneath oceans can be calculated from the age of oceanic lithosphere and thermal cooling models [*de Jonge et al.*, 1994; *Nataf and Ricard*, 1996]. We use the digital age map of *Müller et al.* [1993].

Figure 2.1 shows the velocity perturbation variation with the age of the oceanic lithosphere at depths from 100 to 650 km, based on the seismic tomographic model SH12WM13 [*Su et al.*, 1994] (circles). The velocity perturbations are calculated by averaging the velocity perturbations along the positions corresponding to each isochron on the surface of the Earth. The velocity perturbation vs. age curves at different depths have the same characteristics; they are flat over a certain period of age, then increase with age. The "turning points" of these curves are strongly dependent on the thermal diffusivity. However, with thermal diffusivity of κ=1.0 mm^{2}s^{-1}, conduction is primarily confined to about the top 150 km of the mantle. There are two possible explanations for the observed relation of average velocities and age of oceanic plates. 1) If the tomographic models are "exact" and do not suffer from any smearing, conductive cooling may extend deeper than general assumed. Diffusivity changes, for example, due to chemical changes with depth may be involved. 2) The current generation of seismic tomographic models have problems of resolution, coverage and crustal corrections. Details such as lithospheric thickening with age probably cannot be accurately recovered. The relation between velocity perturbations and age may be due to the smearing effects of the seismic inversion.

Our goal is to remove, empirically, the near-surface effects rather than interpreting them. We try two ways to remove the effects of the conductive cooling of oceanic plates. 1) A cooling model with one layer (0-210 km) with thermal diffusivity of $\kappa_1 = 1.65\ \mathrm{mm^2 s^{-1}}$ [*Kobayashi*, 1974] over a half space is used to explain the velocity-age curves at various depths. The effective diffusivity below 210 km is assumed to be $\kappa_2 = 3.3\ \mathrm{mm^2 s^{-1}}$. There is still one unknown, the conductivity ratio between that of the layer and that of the half space. The temperature derivatives which relate the temperature perturbation to velocity perturbation are uncertain [*Estey and Douglas*, 1986; *Karato*, 1993]. Effects of pressure and chemical differences would make these parameters even more uncertain. Since our purpose is to find the best fit model, and remove it, rather than to find the conductivity ratio or temperature derivatives, we make no attempt to guess these parameters, but fix the conductivity ratio and find the best temperature derivatives at various depths. The best fit velocity models, in the oceanic regions, are found by adjusting the temperature derivatives, at various depths, in order to minimize the difference between the thermal velocity model and SH12WM13 in the oceanic regions. The predicted velocity-age relations are indicated as light lines in Figure 2.1. 2) We assume that age correlated variations in the mantle below 200 km are the result of smearing by the inversion. The theoretical temperature models are calculated by a half space cooling model ($\kappa = 1.65\ \mathrm{mm^2 s^{-1}}$) above 200 km. The theoretical temperature distribution below 200 km is assumed to be the same as that at 200 km predicted by the half space cooling model (this can be thought of as equivalent to the "smearing" effects in tomography). The best fit velocity models are found by the same procedure in 1). The predicted velocity-age relations are indicated as dash lines in Figure 2.1. The resultant residual tomographic models from both procedures are the same above 200 km and only slightly different between 200 and 400 km depths. The follow-up analysis, using the residual tomographic models, gives the same results. The high velocity behavior under old lithosphere in the transition zone (400 - 670) could be due to the effect of stagnant slabs. For simplicity, we present the results by using the resultant residual tomographic models from procedure 1. The

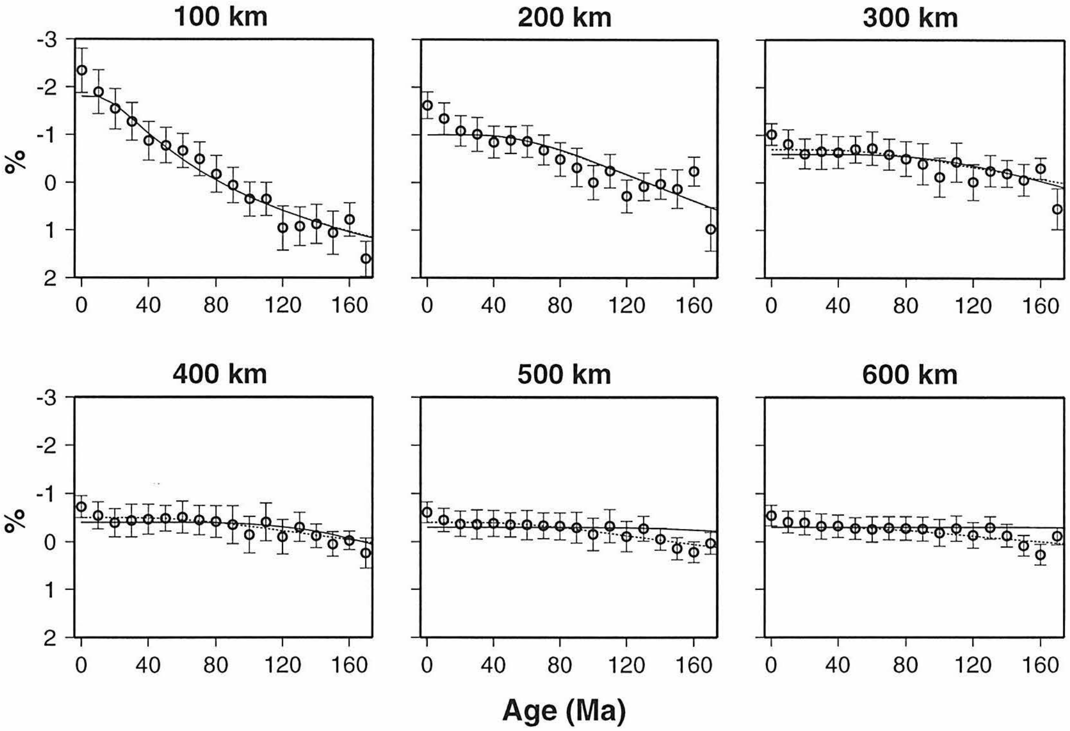

Figure 2.1: The velocity perturbation vs. age of oceanic plates at various depths, based on SH12WM13 [*Su et al.*, 1994] and digital age map [*Müller et al.*, 1993]. The velocity perturbations are averaged along each isochron. The RMS values, based on SH12WM13, with respect to the mean velocities are also plotted.

predicted models are expanded into spherical harmonics and are truncated at degree 12, in order to compare with SH12WM13. The first residual tomography (RES1) is obtained by excluding the oceanic plate component from the seismic tomography (SH12WM13).

2.3.2 Cratons

The contribution of cratonic "roots" to seismic velocity variation in spherical harmonic space is obtained by expanding the function, which, in cratonic regions, for each group of cratons, has the value of the average velocity perturbations from the residual tomography (RES1), and zero outside, into spherical harmonics. We classify the cratons according to their geographic locations and ages based on *Sclater et al.* [1981]. The cratons are divided into 13 groups; six for cratons between 800-1700 Ma

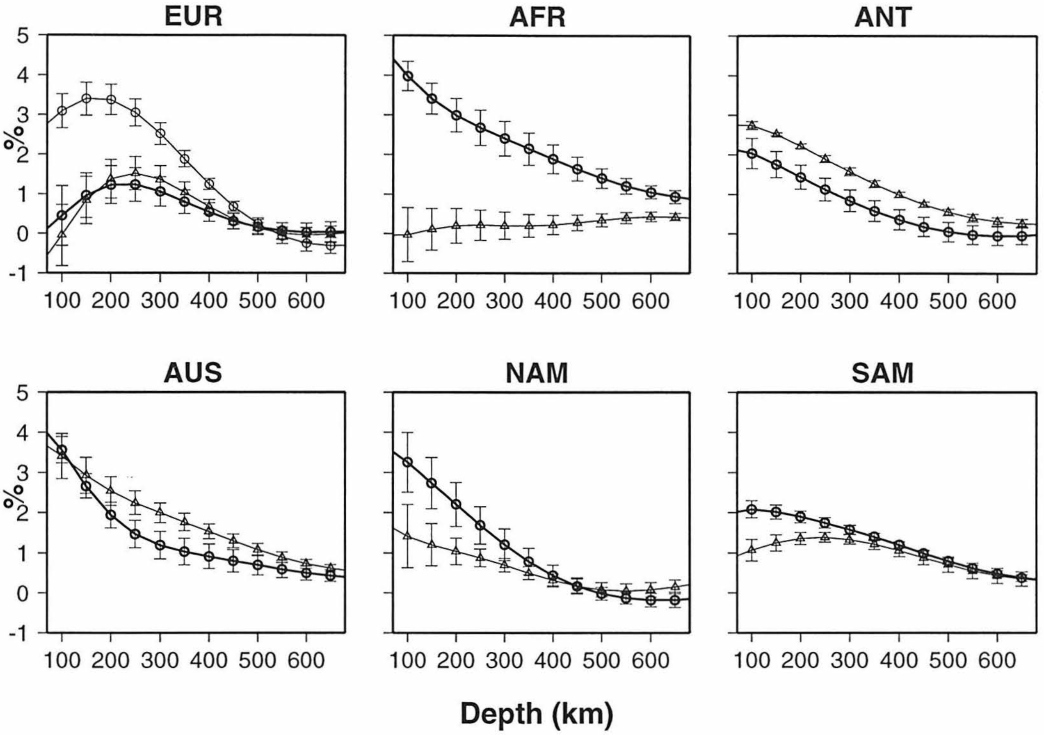

Figure 2.2: The average velocity perturbations beneath each group of cratons vs. depth. The RMS values, based on SH12WM13, with respect to the mean velocities are also plotted. Circles indicate those for cratons older than 1700 Ma and triangles indicate those for cratons younger than 1700 Ma.

(Middle Proterozoic), and seven for those older than 1700 Ma (Archean and Early Proterozoic). Each group is related to a major plate. For instance, cratons, between 800-1700 Ma, on the South American plate are placed in the same group. Cratons older than 1700 Ma in Eurasia fall into two groups. Figure 2.2 shows the velocity perturbations beneath each group of cratons vs. depth. The heavy lines and circles are the velocity perturbations for cratons older than 1700 Ma. The light lines and triangles are for cratons between 800-1700 Ma. This set of spherical harmonic coefficients can be multiplied by an arbitrary constant (C). This proportionality constant (C) is a parameter to be determined later. The goal is to remove the direct effect of the cratons from mantle tomography.

2.3.3 On-going subduction

We assume that the subducting plates sink vertically into the upper mantle at the velocity of the plate at the trench. The ages of the slabs are reconstructed at every depth. We assume that the seismic velocity perturbation within the slab is constant (δV_s) at a certain depth. The width of a particular slab segment is equal to its thickness. Thickness is calculated from the age of the oceanic lithosphere at the time of subduction [*Wen and Anderson*, 1995]. On-going subduction can cause low-velocities in the shallow mantle, because of volatile fluxed melting in the mantle wedge [*Anderson et al.*, 1992], and high-velocities at greater depth due to low-temperatures in the slab. We permit δV_s to take on negative or positive values (negative values probably imply partial melting).

2.3.4 Residual tomographic models

Synthetic models are obtained by linear superposition of the contributions from slabs, oceanic plates, and cratons at various depths. The two parameters (δV_s and C) at each depth are chosen by minimizing the quantity:

$$\sum \sqrt{V_{syn}^2 - V_{tomo}^2}$$

Where V_{syn} and V_{tomo} are the velocity perturbations of the synthetic model and SH12WM13, at a certain depth, respectively; the summation is over every 1° × 1° cell in a global grid. The residual models are obtained by subtracting synthetic tomography from SH12WM13. The residual models from 100-650 km depths are plotted in Figure 2.3. It should be noted that the possible effects of Gibbs oscillations due to the spherical harmonic truncations may influence our result to some extent, even though they are second order compared to the uncertainties in the subtraction of oceanic lithospheric cooling.

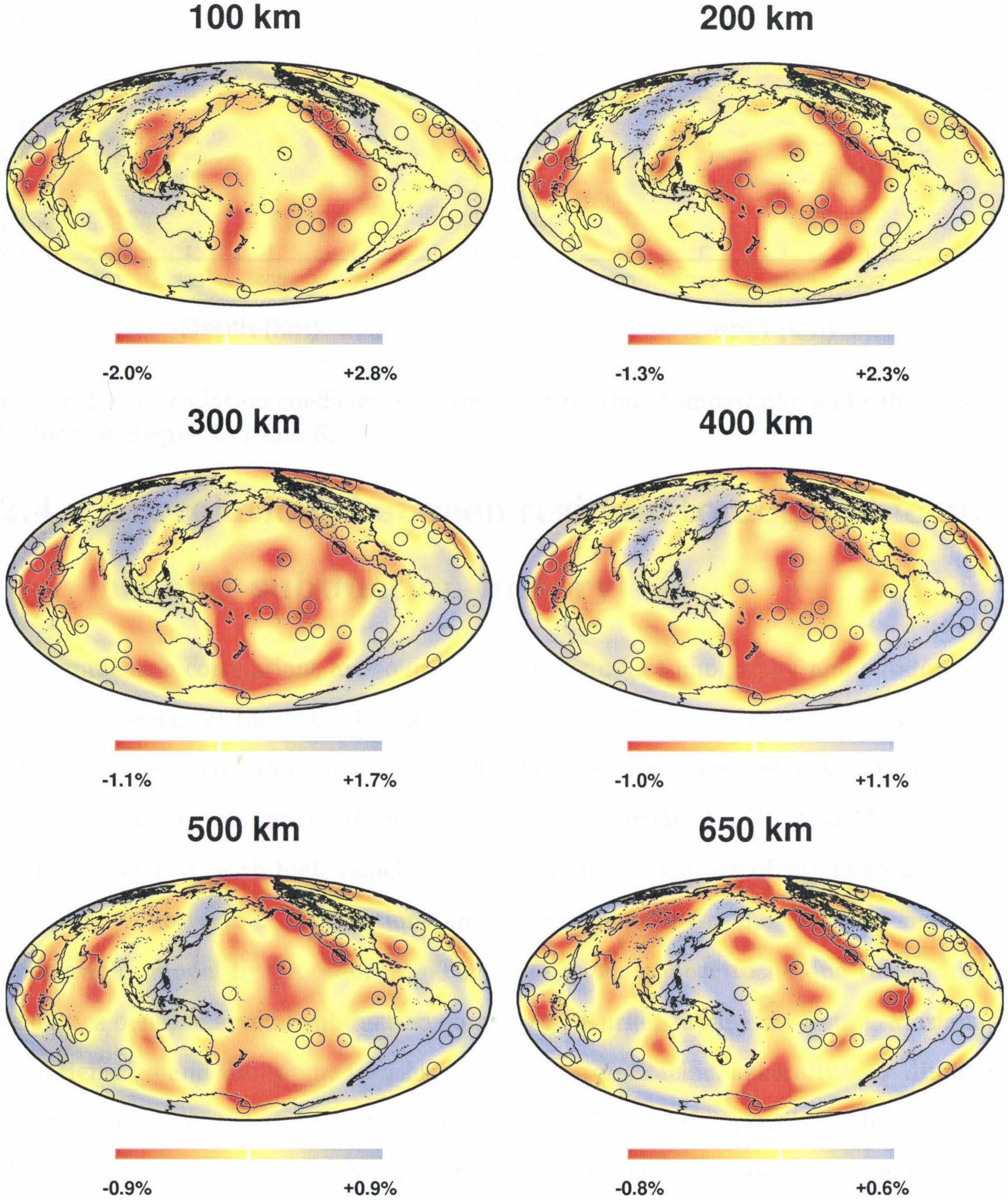

Figure 2.3: Residual tomographic models at various depths in the upper mantle. The positions of hotspots are indicated by circles.

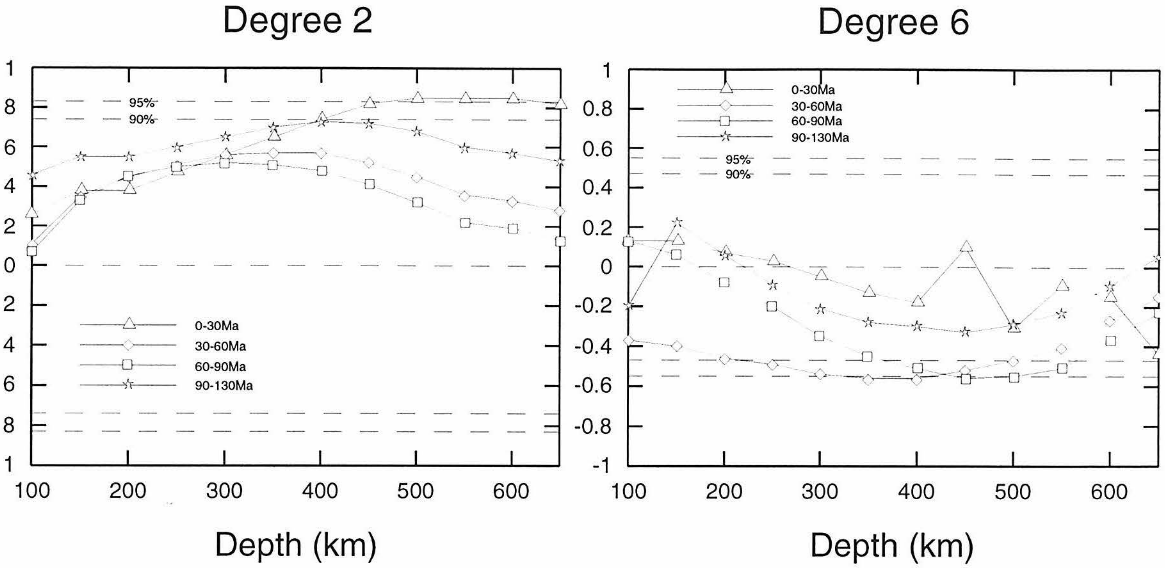

Figure 2.4: Correlation coefficients between the residual tomography and subduction history, at degree l=2 and 6.

2.4 Correlations between residual tomographic models and subduction history

No significance correlations are found between residual tomography and subduction history between 30-130 Ma [*Wen and Anderson*, 1995] (see Figure 2.4). There are some negative correlations between 30-90 Ma subduction and residual tomography in the 350-500 depth range. Residual tomography correlates with 0-30 Ma subduction, only at l=2, with high velocities corresponding to regions of subduction in the transition zone region. Correlations are less pronounced for the resultant residual tomography model by procedure 2. The correlations appear to be due to the high velocities beneath several subduction zones (e.g., Kurile, Japan, Izu-Bonin, Mariana, New Hebrides and Philippine trenchs, i.e., the western Pacific, generally west dipping slabs) rather than the global subduction pattern. We test this possibility by dividing the subduction in the past 30 Ma into two groups. Group 1 contains only the 0-30 Ma subduction in the Kurile, Japan, Izu-Bonin, Mariana, New Hebrides and Philippine trenches; group 2 includes subduction in the other convergence regions (e.g., Aleutian, Chile-Peru, Tonga-Fiji, Java trenches, etc). We found excellent correlations at degree

2 and 3 for group 1 subduction and no correlation for group 2 subduction (Table 2.1). Correlations which are significant at greater than 90% confidence level are underlined. The correlations have two possible explanations: 1). The resolution of the seismic model prevents us from excluding the on-going slabs efficiently by introducing the theoretical slab function. If slabs in the transition zone beneath the group 2 were not recovered in the seismic inversion, perhaps because of coverage problems, we cannot exclude efficiently the effects of on-going subduction from our procedures. We cannot discard this possibility for the present generation of tomographic models. 2) Some slabs beneath group 1 trenches accumulate in the transition zone region for a period of time. The behavior of the slab at the 670 km discontinuity is region-dependent, as suggested by seismology [e.g., *Jordan and Lynn*, 1974; *Zhou and Anderson*, 1989; *van der Hilst et al.*, 1991; *Fukao et al.*, 1992] and geodynamics [*Gurnis and Zhong*, 1995]. It may also be true that other effects, such as slab dip, direction of dip, trench migration or presence of back-arc basins are important and that the distinction between group 1 and group 2 slabs is geodynamically significant. The degree 2 heterogeneity is the most important component for many geophysical observables, such as seismic velocity [e.g., *Masters et al.*, 1982] and geoid [*Lerch et al.*, 1979]. However, the origin of this degree is still controversial. For the analysis of spectrum, we interpret the high velocities beneath group 1 trenches as stagnant slabs and subtract their effect from the residual tomography in the transition zone (450-650 km), assuming that stagnant slabs are only beneath group 1 trenches. Figure 2.5 shows the power spectra of the seismic tomography (SH12WM13), cratonic roots, on-going subduction and stagnant slabs, at degree l=2. In the shallow mantle (above 200 km), the oceanic lithosphere, cratons and subducting slabs contribute most of the power at degree 2. In the transition zone, stagnant slabs are also responsible for the degree 2 lateral variation.

Table 2.1: Correlations between 0-30 Ma subduction and residual tomography

	l=2		l=3	
Depth (km)	Group 1	Group 2	Group 1	Group 2
400	0.60	0.03	0.12	-0.70
450	0.74	-0.06	0.39	-0.80
500	0.83	-0.15	0.58	-0.83
550	0.88	-0.20	0.64	-0.84
600	0.91	-0.20	0.71	-0.80
650	0.91	-0.26	0.67	-0.81

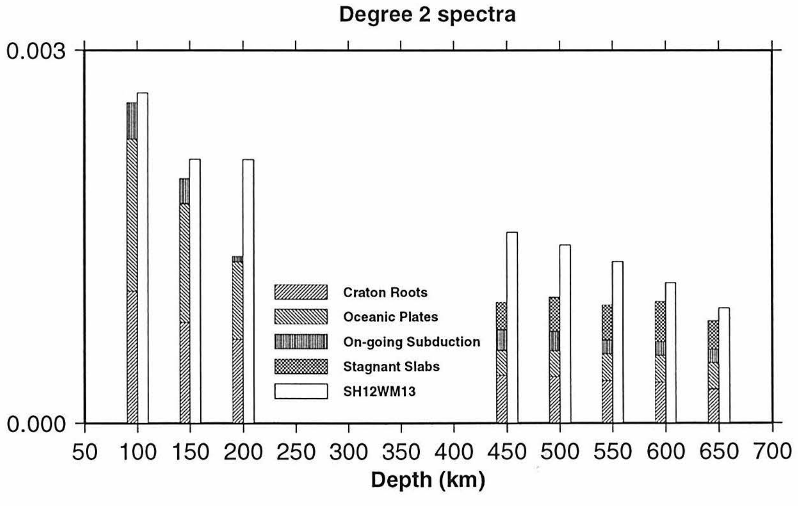

Figure 2.5: The degree 2 power spectra of SH12WM13, cratonic "roots," on-going subduction, oceanic plates, and stagnant slabs in the upper mantle.

2.5 Hotspots, cratons and mantle convection

Residual tomography, which excludes the near-surface features, may provide a constraint on convection in the mantle. Passive ridges are the first-order upwellings on the surface of the Earth. They possibly represent normal (uncooled) mantle. Hotspots are generally considered to be caused by deep, narrow, active upwellings. In this section, we use seismic tomography to attemp to constrain the characteristics of hotspots throughout the mantle. We use seismic tomography (SH12WM13) in the lower mantle and residual tomography in the upper mantle. The list of 47 hotspots, complied by *Morgan* [1981] and *Crough and Jurdy* [1980], is used.

The overall distribution of hotspots correlates very well with low seismic velocities in the deep lower mantle (1700 km-CMB) at degree l=2. There is some correlation with l=3 as well in the lower mantle. However, the degree 2 correlations are poor in the depth region 700-1700 km (except 900-1000 km). This is consistent with the results of previous authors [e.g., *Kedar et al.*, 1993]. Table 2.2 gives correlation coefficients between hotspot distribution and residual tomography in the upper mantle. Positive values mean that hotspot positions favor low velocity regions. Correlations which are significant at the greater than 90% confidence level are underlined. Hotspots correlate with slow seismic velocities at degree l=2 to 400 km depth and at degree l=4 to 150 km depth. The degree 2 correlations decrease very rapidly into the transition zone. Also, at l=4, hotspots correlate with fast velocities in part of the transition region (400-500 km) (Table 2.2). There is no significant correlation at degree l=6 between hotspot distribution and residual tomography in the upper mantle.

It is useful to discuss hotspots in the context of the three-dimensional residual velocity structure of the upper mantle. Most of the hotspots in the Pacific and circum-Pacific area are in long wavelength low-velocity regions of the upper mantle. Some hotspots are also in low-velocity regions in Africa, the Indian ocean and the North Atlantic. Most hotspots in the South Atlantic, around South America and near south Africa are in high-velocity regions. The high velocities under some hotspots in Africa could be because they are close to high-velocity cratonic "roots." This spatial

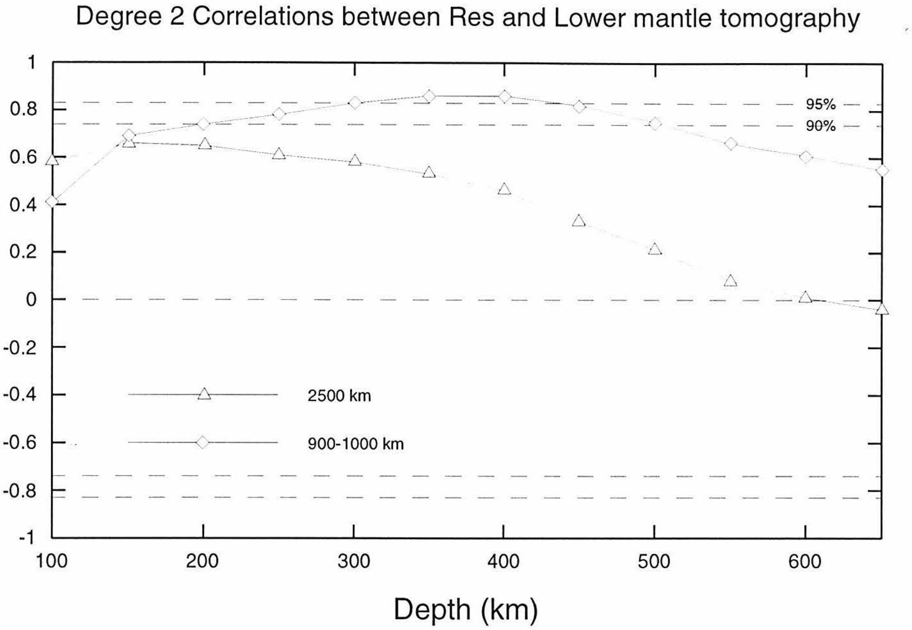

Figure 2.6: Correlations between the residual tomographic models with seismic tomographic model at 2500 km and 900-1000 km depths.

visual check and the good correlations at degree l=4 suggest that correlations between hotspot and residual seismic tomography in the upper 400 km, at long-wavelengths, are meaningful (Table 2.2).

Is there any connection between the correlations at shallow depths and lowermost mantle? No significant correlation is found between seismic tomography at 2500 km and residual tomographic models, at degree l=2 (Figure 2.6). The correlation is negative for residual tomography at 650 km. Tomographic models from 1700 km to CMB have similar correlations. However, residual tomographic models between 200-500 km depth correlate with the seismic tomography model in the 900-1000 km depth region. This is the only region in the lower mantle that correlates with residual tomography. Direct comparison among the degree 2 patterns of hotspots, residual tomography and lower mantle tomography is shown in Figure 2.7. They all have low values in the central Pacific and Africa; the residual tomography and hotspot highs (devoid of hotspots) extend to the south of South America and east of Asia. It is not clear how to relate the correlations at shallow depths with those in the deep mantle. However, it does appear that degree 2 is one of the fundamental modes in mantle convection. This is not predicted by convection models with uniform boundary conditions [e.g., *Tackley et al.*, 1993]. Hotspots do not appear to originate in mantle that has been cooled or blocked by slab. Previously normal mantle which has been cooled by subduction (fast seismic velocities) will, of course, correlate with subduction history. But tomography in this mantle will also correlate with hotspots, even if only "normal" mantle is present. Downwellings in the deep lower mantle, whether they are caused by slab accumulations, or are indirectly related to present or past subduction, will make the seismic patterns in this region correlate with hotspots. Do slabs cool the mantle or do plumes heat the mantle, or both? Is "normal" mantle uncooled or not heated? The cause and the effect must still be disentangled.

The degree l=6 correlation between upper mantle tomography and distribution of hotspots is actually a representation of correlation of distribution of cratons and distribution of hotspots at this degree. Figure 2.8 shows the degree 6 map of the craton function, which has unit value in cratonic regions and zero outside. The l=6 expansion has highs in most of the cratonic regions and lows in the North Atlantic, equatorial Atlantic, the Pacific superswell, south of New Zealand and the Afar. It looks very much like the l=6 hotspot [*Cazenave et al.*, 1989] and dynamic topographic maps [*Cazenave and Thoraval*, 1994].

This has several alternative explanations:

1. The pattern of convection in the upper mantle is modulated by cratons; hot upwellings occur in complementary locations. Cratons act as cold fingers and perturb the thermal and geometric properties of the boundary layer.

2. Hot upwelling mantle tends to drive cratons away and they settle in areas of colder mantle. Surface plates respond passively to mantle flow.

3. The degree l=6 pattern of surface dynamic topography could be the result of hot upwellings, if cratonic "roots" have normal densities, or the result of dense cratonic "roots" or both.

Hotspot Density: degree 2

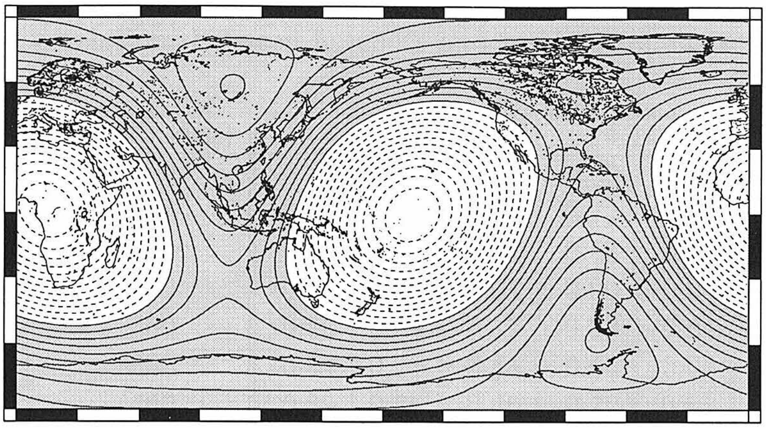

Residual Tomography (300 km): degree 2

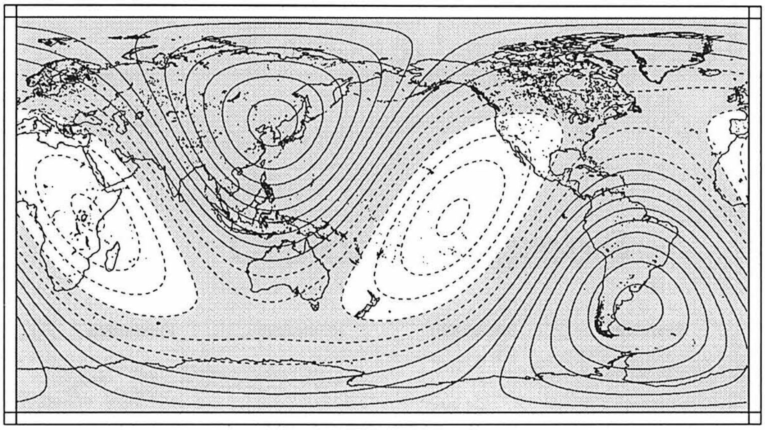

SH12WM13 (2500 km): degree 2

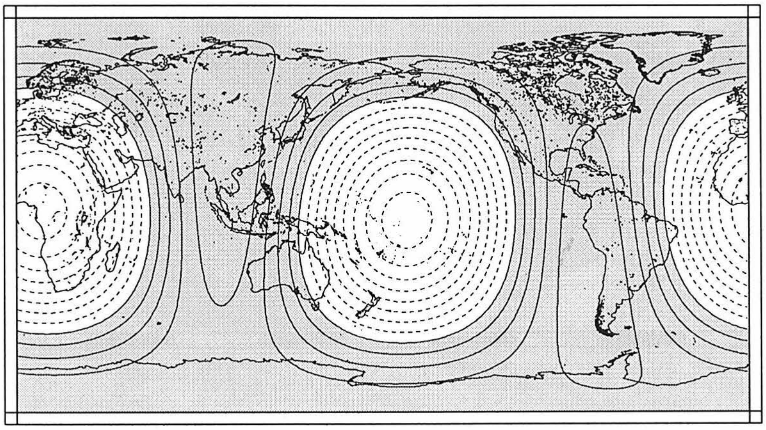

Figure 2.7: Degree 2 patterns for hotspot distribution, residual tomography at 300 km and seismic tomography at 2500 km. The dash contour area means the places with high number of hotspots or low seismic velocities.

Table 2.2: Correlations between hotspots and residual tomography at degree l=1 to l=6

Depth (km)	1	2	3	4	5	6
100	-0.42	0.47	0.17	0.90	-0.03	0.36
150	-0.47	0.79	0.19	0.72	-0.01	0.44
200	-0.62	0.86	0.11	0.43	-0.03	0.47
250	-0.70	0.85	0.04	0.09	-0.04	0.45
300	-0.80	0.83	-0.17	-0.23	-0.04	0.40
350	-0.84	0.77	-0.34	-0.54	-0.03	0.03
400	-0.89	0.76	-0.46	-0.72	-0.01	0.26
450	-0.82	0.53	-0.56	-0.87	-0.08	0.36
500	-0.75	0.39	-0.48	-0.80	0.13	0.40
550	-0.64	0.23	-0.43	-0.71	-0.15	0.43
600	-0.42	0.15	-0.33	-0.68	-0.16	0.46
650	-0.32	0.08	-0.27	-0.60	-0.05	0.44

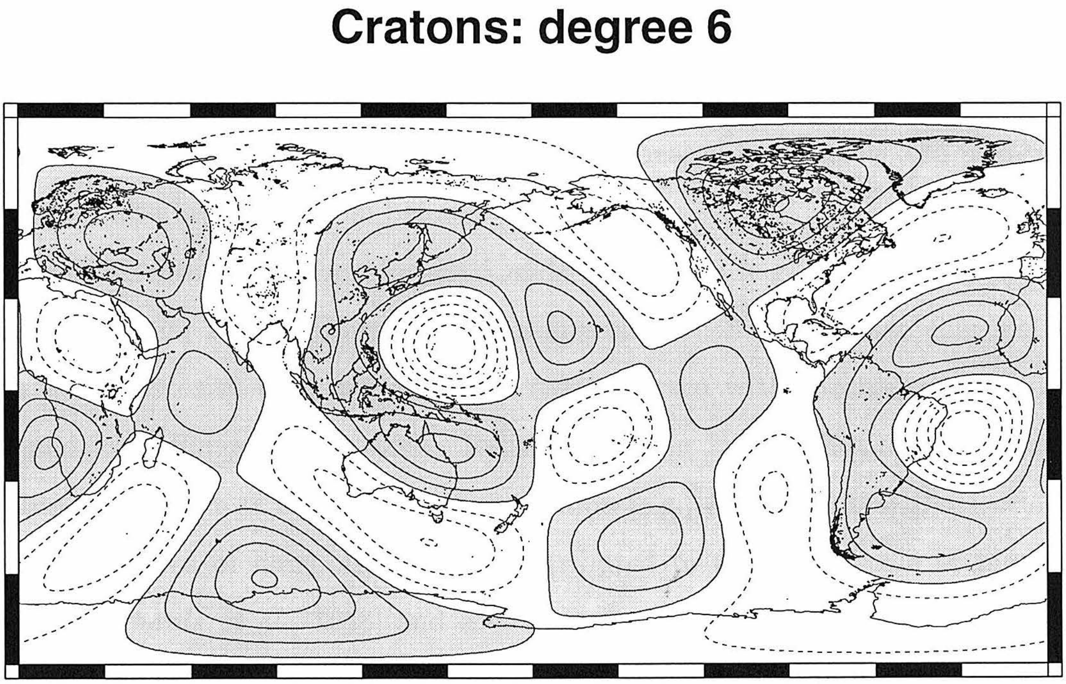

Figure 2.8: Degree 6 pattern of craton function, which has unit value in cratonic regions and zero outside. The dash contour area means the places with low numbers of cratons.

4. l=6 convection is intrinsic to the upper mantle [*Tackley et al.*, 1993]. Cratons in cold regions and upwellings in complementary regions establish the phase of the pattern.

Thermal instability of the lower thermal boundary layer is unlikely to be the main control on mantle convection. Cratons probably have long-lived "roots" extending to about 200 km and associated cold, high-velocity material may extend somewhat deeper. This is a large fraction of the depth of the upper mantle and the presence of thick cratons must influence mantle convection. In addition, a moving craton overrides cold oceanic lithosphere, placing a cold slab about 100 km thick under the craton. This cold dense downwelling also affects mantle convection, even after it settles "on the bottom." The upper mantle could be a system, cooled and dragged down at subduction zones and affected by lateral temperature gradients at the surface, with subcratonic isotherms at a deeper level than isotherms elsewhere, except in slabs. This general type of convection was treated by *Pekeris* [1935], *Allan et al.* [1967] and *King and Anderson* [1995]. It is quite distinct from the Rayleigh-Bénard convection in a fluid system heated from below which forms the basis for most discussions of mantle convection. The mantle could be heated from below and from within and could also be cooled from below.

Much attention has been focussed at l=2 and l=6 [e.g., *Richards et al.*, 1988; *Cazenave et al.*, 1989]. Convection in a spherical shell with phase changes or an increase of viscosity with depth gives a red spectrum with spectral peaks between l=2 and l=6 [*Bunge et al.*, 1996]. It has long been known that surface boundary conditions may act as a template for convection [e.g., *Pekeris*, 1935; *Elsasser*, 1969]. The l=6 pattern of hotspots has been attributed to a natural scale of plume formation [*Richards et al.*, 1988] and a characteristic of the lower thermal boundary. However, the strong l=6 convection could be intrinsic to the background flow, modulated by subduction history and surface boundary conditions.

2.6 Conclusion

Residual tomography is calculated from seismic tomography by excluding the effects of oceanic lithosphere cooling, cratonic "roots" and cooling or partial melting associated with subducted slabs in the upper mantle. There is no correlation between 30-130 Ma subduction and residual tomography in the upper mantle. Residual tomography in the transition zone correlates with 0-30 Ma subduction, especially the subduction in the Kurile, Japan, Izu-Bonin, Mariana New Hebrides and Philippine trenches. This can be explained either by stagnant slabs beneath those trenches, or by lack of lateral resolution of seismic tomography in other subduction regions. Most (slightly more than half) hotspots appear to be in slow regions of the upper mantle. The overall pattern of hotspots correlates with residual tomography in the top 400 km at degree $l=2$ and 4. Correlations decrease very rapidly in the transition zone region. About 25% of the hotspots occur in regions of the mantle which are slow down to 650 km depth. Hotspots also correlate with seismic tomography in the 900-1000 km region and the deep lower mantle at spherical harmonic degree $l=2$. However, the correlation between residual tomography in the upper mantle and seismic tomography in the deep lower mantle is poor. At spherical harmonic degree $l=6$, the distribution of hotspots correlates with the distribution of cratons and residual topography instead of residual tomography. Cratons may affect the locations of upwellings, thus modulating mantle convection, or the degree $l=6$ could be intrinsic with cratons and hotspots establishing the pattern. Mantle convection could be a system controlled by subduction and modulated by near surface conditions [*Elsasser*, 1969].

Chapter 3 Layered mantle convection: A model for geoid and topography

3.1 Abstract

The long-wavelength geoid and topography are dynamic effects of a convecting mantle. The long-wavelength geoid of the Earth is controlled by density variations in the mantle and has been explained by circulation models involving whole mantle flow. However, the relationship of long-wavelength topography to mantle circulation has been a puzzling problem in geodynamics. We show that the dynamic topography is mainly due to density variations in the upper mantle, even after the effects of lithospheric cooling and crustal thickness variation are taken into account. Layered mantle convection, with a shallow origin for surface dynamic topography, is consistent with the spectrum, small amplitude and pattern of the topography. Layered mantle convection, with a barrier about 250 km deeper than the 670 km phase boundary, provides a self-consistent geodynamic model for the amplitude and pattern of both the long-wavelength geoid and surface topography.

3.2 Introduction

Geoid and topography are connected dynamic effects of a convecting mantle. The dynamic topography, caused by deep mass anomalies, is quite different from the actual observed topography, which is dominated by variations in crustal thickness and thermal subsidence of oceanic plates. It is difficult to correct for these variations so it is uncertain exactly how much of the Earth's long-wavelength topography is actually due to the mass heterogeneities in the mantle. Several studies indicate that the smoothed topography in oceans deviates only slightly from thermal conduction

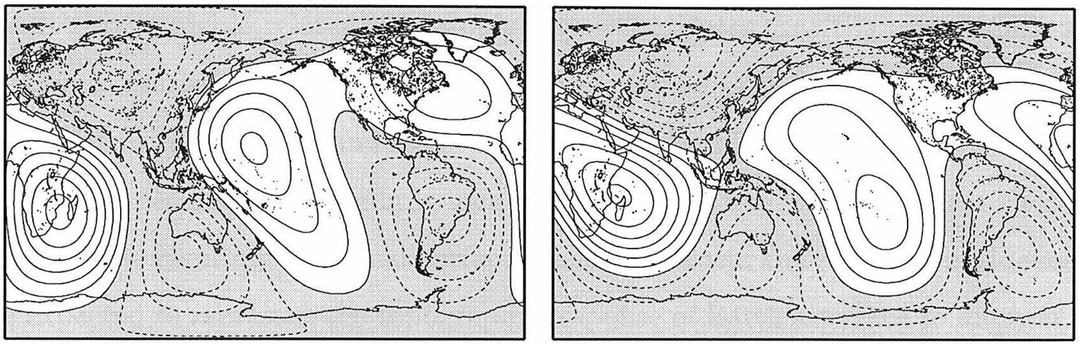

a: Residual Topography 1

b: Dynamic Topography 1

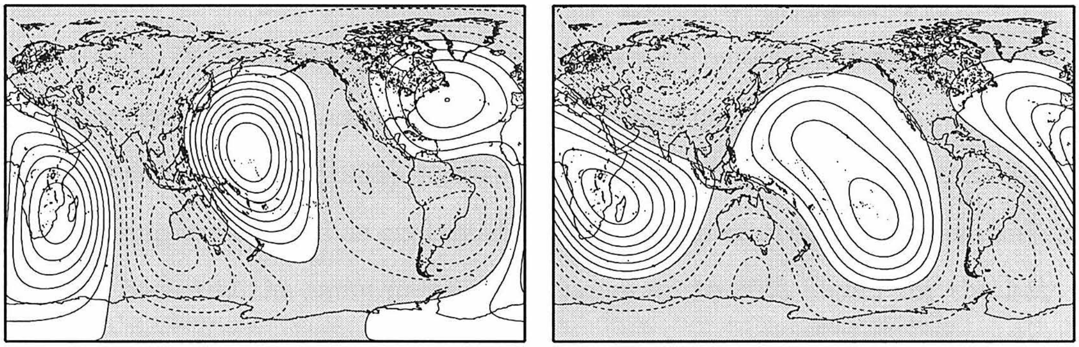

c: Residual Topography 2

d: Dynamic Topography 2

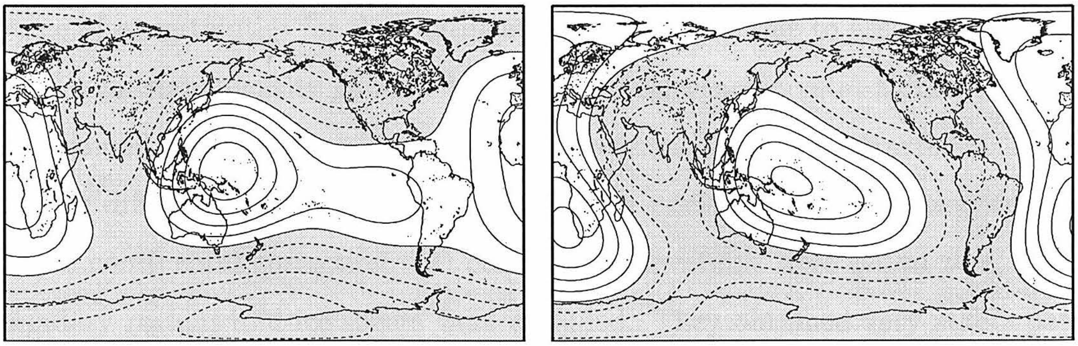

e: Observed Geoid

f: Predicted Geoid

Figure 3.1: The l=2-3 components of residual topography corrected for crustal thickness variation by assuming Airy compensation in continental regions and sediment loads and thermal subsidence based on: 1, plate model [*Stein and Stein*, 1992] (a) and 2, half space cooling model [*Marty and Cazenave*, 1989] (c) in oceans, dynamic topography predicted by 1, model WA1(b) and 2, model WA2(d), nonhydrostatic geoid (e) and geoid predicted by model WA1(f). Topography and geoid are predicted by assuming layered mantle flow stratified at 920 km. Topography and geoid lows are shaded. Contours: a,b,c,d: 100 m; e,f: 20 m.

models (about $\sim$ 500 m at spherical harmonic degree l=2) [*Cazenave et al.*, 1989; *Cazenave and Lago*, 1991; *Colin and Fleitout*, 1990; *Kido and Seno*, 1994]. The small gravity signal related to cratonic regions indicates that the topographic signal related to cratonic "roots" is also weak. The small amplitude of dynamic topography is consistent with the rise and fall of continents inferred from flooding records [*Gurnis*, 1990]. The residual topography, which is the residual after removal of the topographic components resulting from near surface density contrasts and seafloor subsidence, can be expected to represent the topographic response of Earth's surface to internal loads of the mantle. Figures 3.1a,c show degree l=2-3 components of residual topography and nonhydrostatic geoid [*Marsh et al.*, 1990]. The residual topography was provided by A. Cazenave. We use the residual topography corrected by the subsidence laws in oceanic regions: (1) by *Stein and Stein* [1992] (plate model), shown in Figure 3.1a; (2) by *Marty and Cazenave* [1989] (half-space cooling model), shown in Figure 3.1c. Sediment loading is corrected as explained in *Cazenave et al.* [1986]. Different subsidence laws give basically the same pattern and range up to 30% higher for the half-space cooling model. Over continental regions, topography is corrected for crustal thickness variation [*Cadek and Martinee*, 1991] assuming local Airy compensation. The largest source of uncertainties for the continental corrections is due to assumed crustal density. A constant density of 2800 kg/m^3 and a reference crustal thickness of 35 km are assumed. The mean residual elevation over continents is subtracted to avoid any baseline difference. *Cazenave et al.* [1989] have performed several other treatments for the continental correction: (1) continental elevations were set to zero; (2) plate boundary regions and ice sheets were excluded. They obtained very stable patterns at long wavelengths ($\geq$ 5000 km) and concluded that continental areas contribute negligibly to the very long wavelength residual topography.

The long-wavelength geoid can be explained by whole mantle flow models [*Hager et al.*, 1985; *Forte et al.*, 1993; *King and Masters*, 1992; *Ricard and Wuming*, 1991], although there are problems with the long-wavelength dynamic topography [*Hager and Clayton*, 1989; *Forte et al.*, 1993b; *Phipps-Morgan and Shearer*, 1994; *Thoraval et al.*, 1995]. It is worth noting that, in the traditional geodynamic modeling of the geoid, the predicted geoid anomalies are actually the summation of contribution of mass heterogeneities in the mantle and mass anomalies due to the dynamic topography caused by those mass heterogeneities in the mantle [*Hager*, 1984]. Both the geoid and topography must be explained by a mantle flow model before we can claim that we have a self-consistent model. Dynamic topography is difficult to model because the relations between seismic velocity variations and density variations are non-unique particularly in the upper mantle [*Forte et al.*, 1995] and are not entirely thermal in nature [*Jordan*, 1975; *Anderson and Bass*, 1984]. Cratonic roots have high seismic velocity, but do not necessarily have high density because they are chemically distinct from the surrounding mantle [*Jordan*, 1975; *Anderson and Bass*, 1984]. Most of previous modelings of topography either exclude the shallow structure of the mantle [*Phipps-Morgan and Shearer*, 1994; *Thoraval et al.*, 1995] which is an important contributor to the dynamic surface topography, or put a theoretical slab model into the upper mantle and ignore other density anomalies [*Hager and Clayton*, 1989; *Hager*, 1984; *Ricard et al.*, 1993]. Here we infer mantle density from seismic tomography [*Su et al.*, 1994] in the lower mantle and residual tomography [*Wen and Anderson*, 1997a] in the upper mantle. The residual tomography, the residual after removal of cratonic roots and the effects of conductive cooling of oceanic plates, is used since we want to isolate the dynamical response of the Earth's surface to internal loads. Detailed procedures are presented elsewhere [*Wen and Anderson*, 1997a]. With this approach, realistic subduction effects can also be included. We assume incompressible, self-gravitating Newtonian mantle flow [*Richards and Hager*, 1984]. The large scale structure (l=2-3) will be studied for two reasons: 1) most of the power of the geoid and topography is concentrated at l=2-3 and 2) mode coupling becomes important at shorter wavelengths due to lateral variation of viscosity [*Richards and Hager*, 1989; *Zhang and Christensen*, 1993]. We first reexamine whole mantle flow models and then propose a layered mantle flow model.

3.3 Whole mantle flow models

Three radial mantle viscosity structures and related velocity-density scalings, inferred from whole mantle flow models, by *Hager and Richards* [1989] (HR), *King and Masters* [1992] (KM) and *Forte et al.* [1993] (FPDW) are shown in Figures 3.2a-b. Those models are also used in the analysis of heat flow [*Phipps-Morgan and Shearer*, 1994]. These models have an increase in viscosity of about 10-30 times between the upper and lower mantle. The geoid kernels from these models are similar (Figure 3.2c). These show the effect on the geoid for a mass anomaly at a given depth. Geoid kernels of models KM and FPDW peak in the transition region, whereas model HR is more sensitive to the upper mantle. All geoid kernels are negative in the deep lower mantle. The geoid correlates with the seismic structure positively in the transition region and negatively in the deep lower mantle. The viscous flow model cannot be uniquely determined by geoid modeling. However, the characteristics of these geoid responses may be intrinsic. A successful model, whether it assumes whole mantle flow or layered mantle flow, should have a geoid response similar to those shown in order to fit the geoid. A layered mantle flow model, stratified near the 670 km discontinuity, would have geoid kernels insensitive to mass anomalies in the transition zone region. These three models predict the geoid well from mass anomalies derived from seismic tomography. However, the magnitudes of predicted topography are much larger than observed (about 2.5-3.5 km in peak-peak amplitude). There is some correlation at $l=2$ and no correlation at $l=3$ between observed and predicted topography for these whole mantle flow models. This is consistent with the results of other recent studies [*Phipps-Morgan and Shearer*, 1994; *Thoraval et al.*, 1995; *Stunff and Ricard*, 1995]. A large amplitude dynamic topography is also predicted for the density model inferred from past subduction [*Ricard et al.*, 1993].

It is obvious from effective topography kernels (Figure 3.2d) that current whole mantle convection models cannot predict both the geoid and residual topography simultaneously. The contribution from lower mantle heterogeneity by itself already exceeds the observed residual topography for these whole mantle convection models.

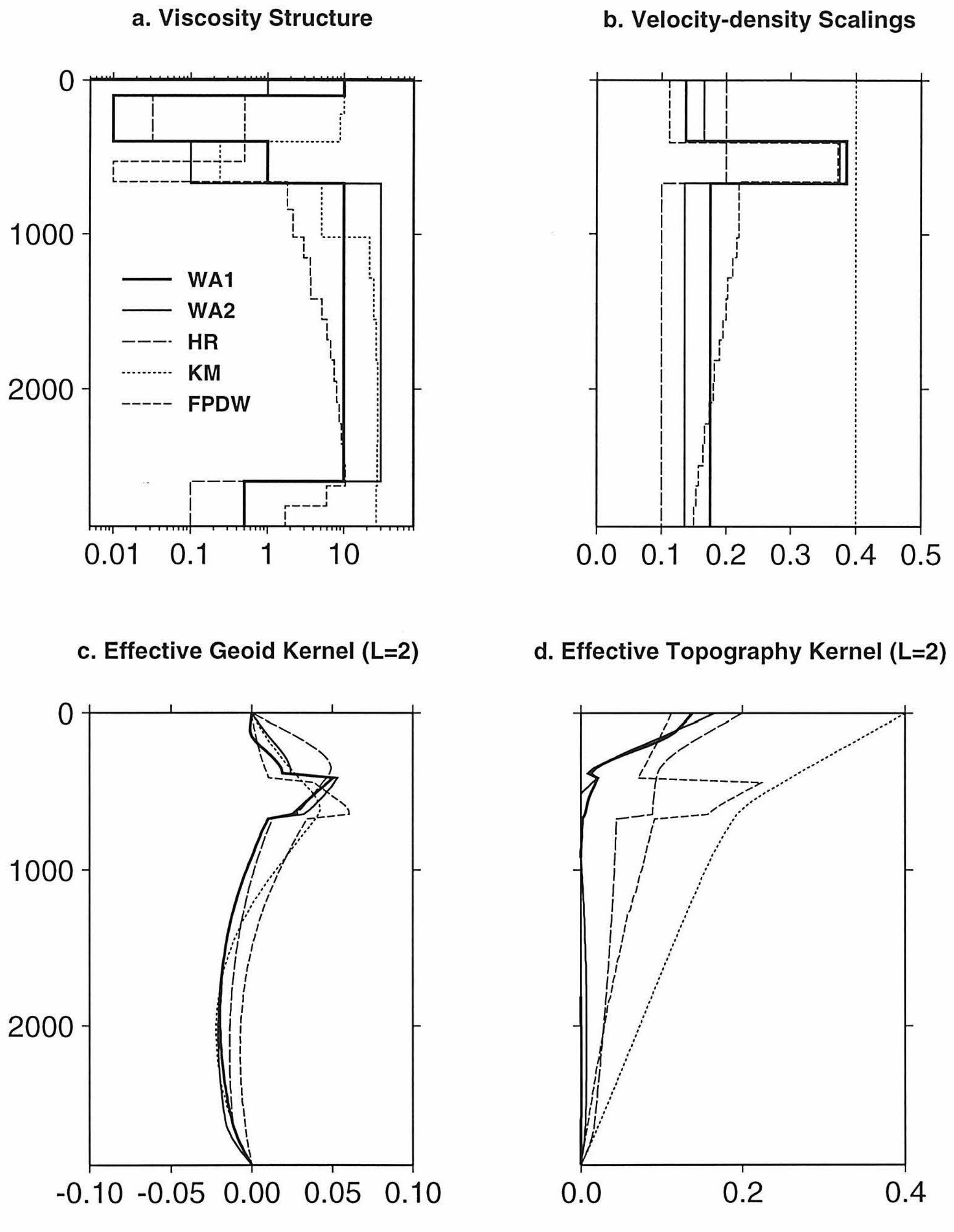

Figure 3.2: Radial viscosity structure (a) and corresponding velocity-density scaling ($\partial ln\rho$ / ∂lnV_s) (b) for three viscosity models, assuming whole mantle flow, HR [*Hager and Richards*, 1989], KM [*King and Masters*, 1992] and FPDW [*Forte et al.*, 1993] and the preferred viscosity models in this study (WA1 and WA2), which assume layered mantle flow stratified at 920 km. The effective degree 2 geoid (c) and dynamic topography kernels (d) for each model. These kernels are multiplied by the corresponding velocity-density scalings for that depth. Qualitatively, the area bounded by the effective topography kernel and vertical axis can be viewed as the amplitude of predicted dynamic topography. Note that the layered mantle flow model WA predicts much less dynamic topography than whole mantle flow models do.

This is evident also in previous work. We have attempted to find a whole mantle flow model that satisfies both the geoid and the dynamic topography. We use the above models for viscosity and assume that the velocity-density scalings are constants in the depth intervals 0-400 km, 400-670 km and 670 km-CMB. We attempted a least-squares fit to the geoid by searching over a range of velocity-density scaling constants. We were unable to reduce the amplitude of the predicted topography. We were unable to obtain a satisfactory fit to both the geoid and the topography at l=2,3 with whole mantle convection by performing a least-squares fit to both the geoid and topography. There is no correlation between residual topography and predicted dynamic topography at l=3 in any case.

3.4 The origin of dynamic topography

The spectra of residual topography and geoid are shown in Figure 3.3a. The amplitude of geoid decreases much faster toward short wavelengths than that of residual topography. The long-wavelength signal senses deeper than short-wavelengths. For potential fields, the faster the spectrum decreases with inverse wavelength, the deeper the origin of anomalies. For example, the magnetic field comes from the core and the spectrum decreases much faster than the geoid and topography spectra. The different behaviors of the spectra of geoid and residual topography imply that dynamic topography is controlled by density variations in the shallow mantle. *Thoraval et al.* [1995] recently proposed that the undulation of the 670 km discontinuity is responsible for the excessive topography at the surface produced by whole mantle flow models. Spectral analysis is useful in discussing this possibility since it depends only on the viscosity model. Let us assume that whole mantle flow models predict twice as much dynamic topography as observed. In this case, half confirms the observation and we will attribute the other half to the topographic effect of the 670 km discontinuity. In order to produce the excess topography that we have assumed, we can quantitatively calculate the spectral behavior of the undulation of the 670 km discontinuity for the various viscosity structure models. Figure 3.3b shows examples of the spectral behavior of the 670 km discontinuity for viscosity models of *Thoraval et al.* [1995] and *Hager and Richards* [1989]. This indicates that if the undulation of the 670 km discontinuity is responsible for the "excess topography" predicted by whole mantle flow models, then the signal increases at short wavelengths for the topography at 670 km. Geoid, topography, subduction history and seismic tomography show that large-scale features dominate mantle convection. It is hard to believe that small scale dominates for topography at the 670 km discontinuity. The spectrum of the seismologically inferred topography of the 670 km discontinuity [*Shearer and Masters*, 1992] is also shown for comparison. This quantitative analysis indicates that if a certain boundary is responsible for the "excess topography" at the surface produced by whole mantle flow models, this boundary cannot be as deep as 670 km. The incorporation of the topography of the 410 km and 670 km discontinuities into the geodynamical modeling also produces large amplitude surface dynamic topography [*Phipps-Morgan and Shearer*, 1994]. It is worth noting that heterogeneities in the upper 300 km were not included in those modelings [*Phipps-Morgan and Shearer*, 1994; *Thoraval et al.*, 1995]. These heterogeneities, however, have significant influence on dynamic topography.

It is also worth noting that explaining the pattern of the dynamic topography is as important as matching the amplitude of dynamic topography for a convection model. At l=2, the residual topography correlates with lower mantle seismic tomography [*Cazenave et al.*, 1989]. But the correlations are even better at shallow depths. No correlations are found in the transition zone region. The connection between deep mantle structure and shallow mantle structure at this degree (l=2) is unclear [*Wen and Anderson*, 1997a] and this confuses the situation. However, the pattern at l=2,3 allows us to discriminate between the various proposals for the origin of dynamic topography. Figure 3.4 shows the spherical harmonic degree l=3 component of the residual topography corrected by difference subsidence laws in the oceans, averaged residual seismic tomography in the top 400 km and transition zone region, and seismic tomography in the lower mantle. There are very good correlations between residual topography and shallow seismic residual tomography with topographic

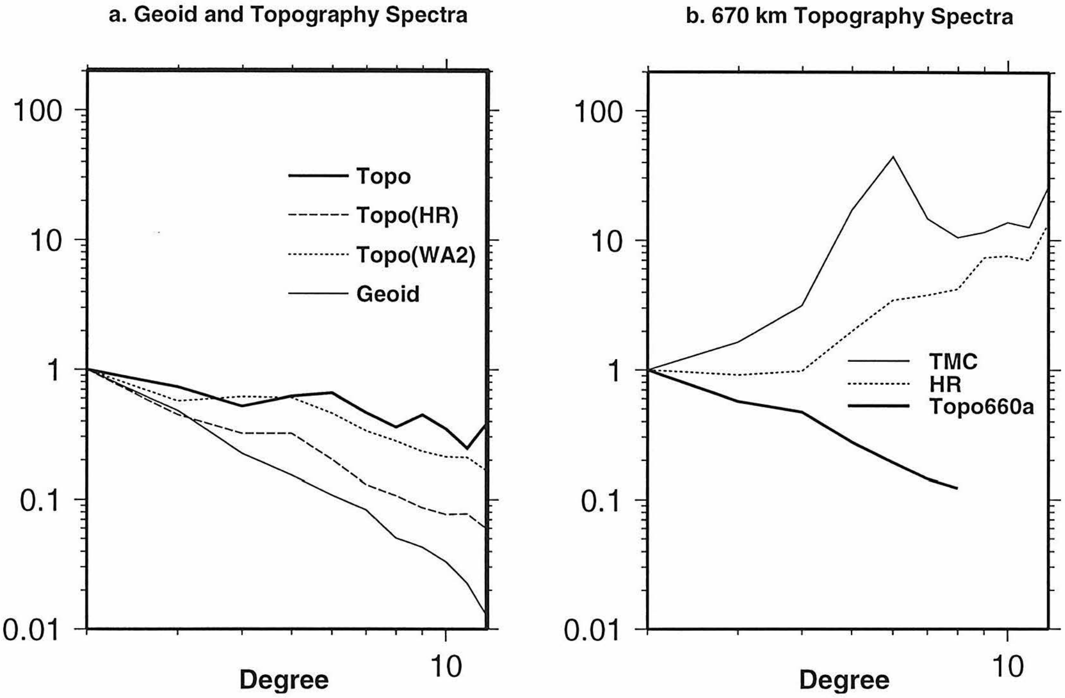

Figure 3.3: a. The spectra of nonhydrostatic geoid [*Marsh et al.*, 1990] and residual topography [*Cazenave et al.*, 1989] and predicted topography by layered mantle flow model WA2 and whole mantle flow model HR. b. The comparison of the spectrum of seismologically inferred topography (Topo660a) [*Shearer and Masters*, 1992] and spectra of the topography at 670 km calculated by using viscosity structure of TMC [*Thoraval et al.*, 1995] and HR [*Hager and Richards*, 1989], if the undulation of the 670 km seismic discontinuity is responsible for the excessive topography at the surface, produced by those models. We assume that the excessive topography is equal to the observed (i.e., whole mantle flow models produce twice as much dynamic topography as observed). Note the different behavior. This implies that "excess topography" at the surface, if there is any, cannot come from as deep as 670 km. For comparison, spectra are normalized to degree l=2. Note the logarithm scale.

lows corresponding with high velocities and topographic highs corresponding with low velocities. The shallow origin of residual topography can be seen clearly from the direct comparison of patterns of residual topography and seismic tomography. If one excludes the structure in the upper 300 km, it is hard to imagine that one can find a viscous flow model that predicts the correct pattern of dynamic topography from a density model inferred from seismic tomography for the rest of the mantle.

3.5 Layered mantle flow model

Shallow origin and small amplitude of dynamic topography have two possible explanations: 1) whole mantle flow with a very high viscosity lower mantle. Such a model would be rejected by the geoid. 2) layered mantle flow with the upper and lower part of the mantle mechanically decoupled. With a large viscosity jump from the upper to lower mantle, the Earth's surface does not respond to the mass heterogeneities in the lower mantle for layered mantle flow model. *Fleitout* [1991] pointed out that the magnitudes of observed surface topography and intra-plate stress is more compatible with a two-layer convective mantle with the lower mantle mechanically decoupled from the lithosphere and unable to induce tectonic stress.

Previous discussions about possible geodynamic barriers have focused on the 670 km discontinuity. Layered mantle convection models, stratified at 670 km, produce excessive topography at this boundary [*Hager and Richards*, 1989] or poor fits to the geoid [*Forte et al.*, 1993]. The incorporation of the seismologically inferred topography on the 670 km discontinuity [*Phipps-Morgan and Shearer*, 1993] seems to rule out this boundary as the dividing line between shallow and deep mantle convection. Many regional high resolution seismic tomography studies also reveal high velocity anomalies below this discontinuity beneath several subduction zones [*Jordan and Lynn*, 1974; *van der Hilst*, 1995]. The 670 km discontinuity is primarily due to an endothermic phase change between the spinel and post-spinel forms of olivine [*Anderson*, 1967]. There is no requirement that compositional difference must set in at this depth. For example, a chemical barrier may exist deeper and be unrelated to the present position

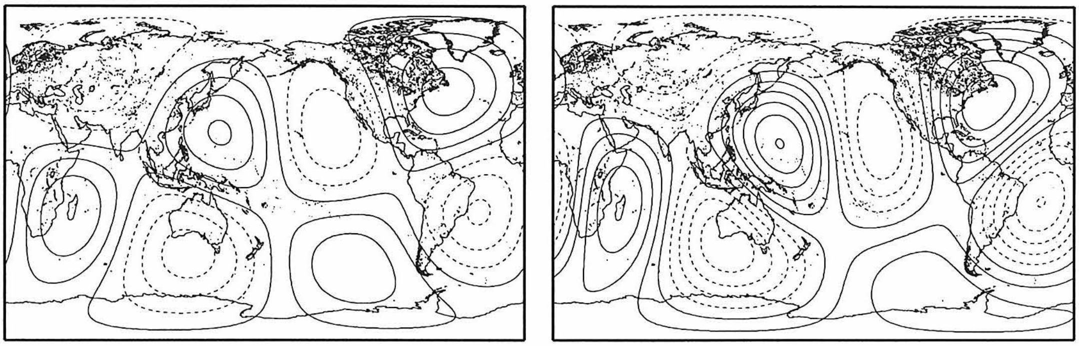

a1. Residual Topography 1

a2. Residual Topography 2

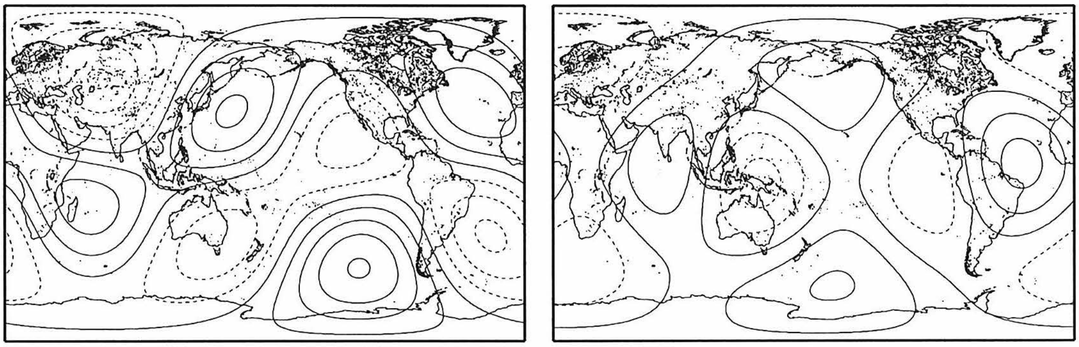

b. Residual Tomography (0-400 km)

c. Residual Tomography (400-670 km)

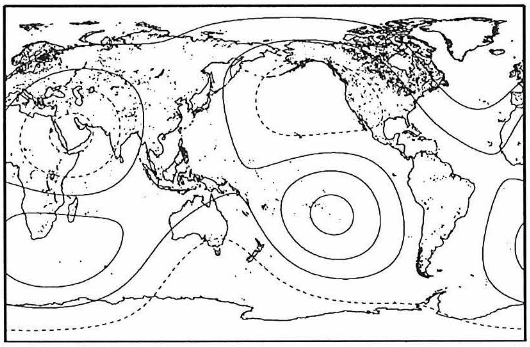

d. S_12WM13 (670 km-CMB)

Figure 3.4: The comparison of l=3 components among the residual topography models by plate model (a1) and half-space cooling model (a2), averaged residual tomography [*Wen and Anderson*, 1997a] in 0-400 km (b), 400-670 km regions (c) and averaged seismic tomography [*Su et al.*, 1994] (d) in the lower mantle. Note that, unlike l=2, strong correlations are only found between residual topography and shallow structure. This also confirms the shallow origin of residual topography. Contours: a: 100 m; b-d: 0.15%.

of the spinel-postspinel phase boundary.

There are now several independent lines of evidence for an important geodynamic boundary in the mid-mantle: seismic evidence for the presence and high relief of a 920 km discontinuity [*Kawakatsu and Niu*, 1994; *Niu and Kawakatsu*, 1997]; correlations between subduction history in the past 130 Ma and seismic tomography at about 800-1100 km depths in the mantle [*Wen and Anderson*, 1995]; decorrelation of seismic tomographic models at 900-1000 km depth [*Ritzwoller and Lavely*, 1995] and reversal of thermal fluctuations at a depth of about 850 km [*Balachandar*, 1995]. It is of interest to see if a barrier near these depths can satisfy the geoid and topographic data.

We apply rheological models, similar to that of *Hager and Richards* [1989] (WA1, WA2, Figure 3.2a). The velocity-density scaling factors ($\partial ln\rho\ /\partial lnV_s$) are assumed to be constants for the depth intervals, 0-400 km, 400-670 km and 670 km-CMB. These three constants are obtained by a least-squares fit to both the geoid and residual topography, assuming a layered mantle convection with a boundary at the 920 seismic discontinuity. WA1 and WA2 are applied for residual topography models corrected by plate model and half-space model separately.

Our best fit velocity-density scaling factors are similar to these for the whole mantle flow model of *Forte et al.* [1993] (Figure 3.2b). The effective geoid kernel is very similar to those of whole mantle convection models [*Forte et al.*, 1993; *King and Masters*, 1992; *Hager and Richards*, 1989] (Figure 3.2c). This indicates the lack of uniqueness of geoid modeling in discriminating between whole mantle and layered mantle flow. Remarkable differences between layered mantle and whole mantle flow models are evident in the topography kernels (Figure 3.2d). For the whole mantle convection models, the topography kernels are sensitive to the whole mantle. For layered mantle convection models, with a viscosity jump of about a factor of 10-30 in the lower mantle (WA1, WA2), and chemical stratification at 920 km, the topography kernel is only sensitive to the upper mantle, i.e., only density anomalies in the upper mantle contribute to most of the dynamic topography. The lower mantle contributes little to the surface dynamic topography for layered mantle flow model WA2. The predicted dynamic topography for layered mantle flow models, at l=2-3, are shown in Figures 3.1b,d. The predicted and observed dynamic topography have highs in the central Pacific and southeast Africa and large depressions in Eurasia, south Australia and South America. At l=2,3, the correlation coefficients between predicted and observed exceed the 95% confidence level for the topography corrected by the plate model, and exceed the 90% confidence level for topography corrected by the half-space cooling model. The predicted geoid is very similar for both models (WA1 and WA2). Therefore, only the prediction from model WA1 is presented in Figure 3.1f. The correlation coefficients between observed and predicted geoid exceed the 95% confidence level at l=3 and the 93% confidence level at l=2. The predictions of geoid and topography reproduce not only the patterns, but also the amplitudes as well. The spectrum of predicted dynamic topography for model WA2 is shown in Figure 3.3a. An example for spectral behavior of dynamic topography predicted by whole mantle flow model (HR) is also shown for comparison. The layered mantle convection flow model is more consistent with the spectral behavior of observed topography.

The topographic relief at the 670 km endothermic phase change is a second order effect in geoid and topography modeling. But it is important in predicting the dynamic topography at a deeper chemical discontinuity. We incorporate the topography at 670 km derived by *Shearer and Masters* [1992] into the calculation and assume a density jump of 9% [*Dziewonski and Anderson*, 1981]. The predicted geoid changes by less than 10% in amplitude, and the correlations persist. There is almost no change in the computed topography. The predicted dynamic topography at 920 km has about 110 km of peak-peak variation of depth, assuming a density change of 0.2 g/cm^3.

Similar to the prediction of surface topography, layered mantle flow models also predict much less amplitude of dynamic topography at the CMB than whole mantle flow models do. Figure 3.5 shows predicted CMB dynamic topography for layered mantle flow model WA2. Model WA1 predicts very similar pattern of the CMB topography with slightly different amplitude. Little topography is related to circum-Pacific regions. Most topography is related to upwelling regions. The peak-peak variation of predicted CMB topography is about 2 km. Whole mantle flow models

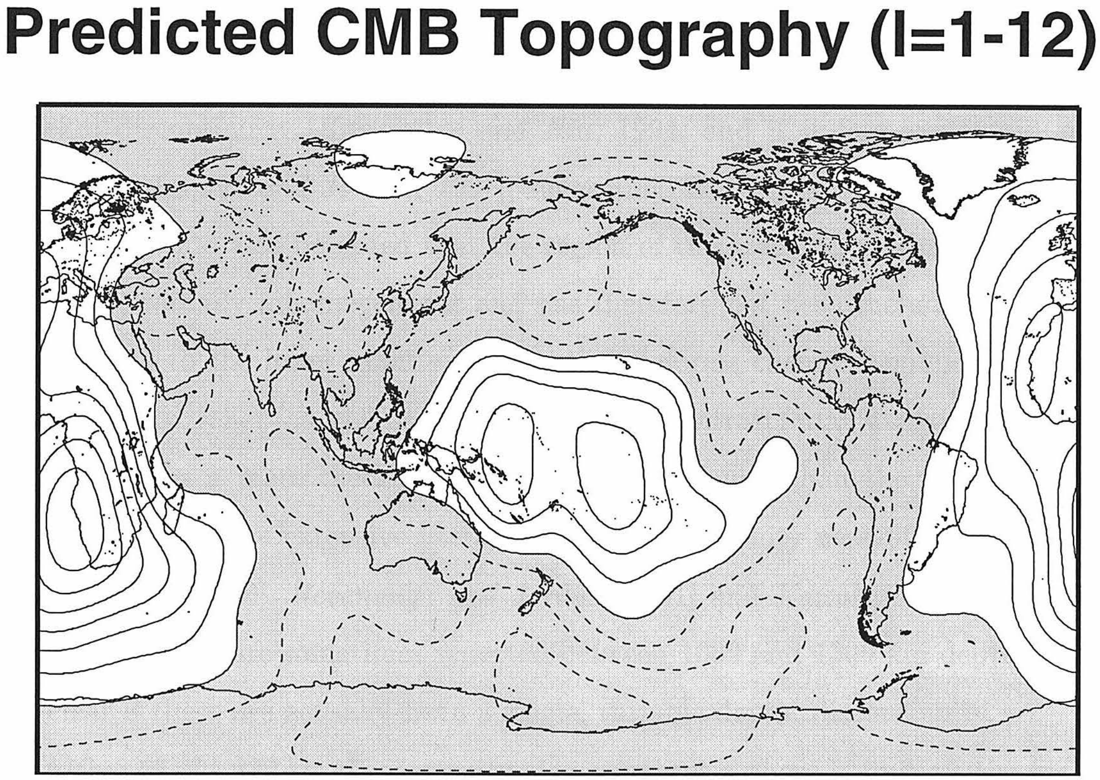

Figure 3.5: Dynamic topography at the CMB predicted by layered mantle flow model WA2. A density contrast of 4.5 g/cm^3 across the CMB is assumed. Topography lows are shaded. Contours: 200 m.

predict at least twice as much [*Forte et al.*, 1993; *Ricard and Wuming*, 1991; *Hager and Clayton*, 1989]. We obtain a second zonal harmonic deviation from the hydrostatic equilibrium figure, with the peak-to-valley deviation being about 550 m, in excellent agreement with the analysis of nutation data [*Gwinn et al.*, 1986]. *Hager and Clayton* [1989] predicted 2 km of excess ellipticity of the CMB. However, our results are inconsistent with some seismological studies [*Morelli and Dziewonski*, 1987; *Doornbos and Hilton*, 1989] but different studies give conflicting results [*Vidale and Benz*, 1992]. It is also unclear how to relate dynamic topography to the actual topography at the CMB.

3.6 Discussion

The seismic discontinuity near 920 km has about one-half the velocity jump as the 670 km discontinuity [*Kawakatsu and Niu*, 1994] and it is less evident in seismic stacks [*Revenaugh and Jordan*, 1991], suggesting that it may exhibit greater topography. It should also be noted that the region of the mantle between 670 and about 900 km is radially inhomogeneous and has therefore not been included in equations of state fits to the lower mantle. Convection deforms chemical boundaries and the high expected relief (as well as its small velocity contrast) may explain why this discontinuity has a more checkered history of being found than the 400 and 670 km discontinuities. The extensive literature on a discontinuity near 900 km is reviewed by *Anderson* [1966], *Revenaugh and Jordan* [1991] and *Kawakatsu and Niu* [1994]. Weak reflections are sometimes reported between 1000 and 1300 km depth. It is not yet clear if these are actually from a single, variable depth, discontinuity.

Although the 920 km discontinuity may represent a phase boundary, the garnet to perovskite transition being the most obvious candidate [*Kesson et al.*, 1994], it may also represent a chemical boundary. Chemical variations between the mesosphere and the lower mantle below about 920 km most plausibly involve variations in MgO, FeO, SiO_2, Al_2O_3 and CaO contents. These are the major controls on density and seismic velocity. Assuming that these oxides are distributed between perovskites and magnesiowüstite, a reasonable intrinsic density difference may be of the order of 0.1 g/cm^3. For example, a chondritic mantle, depleted of Al_2O_3, MgO and CaO to form the crust and a fertile upper mantle will have Mg/Si about 1 (perovskite) and low Ca and Al in the residue. The radioactive elements will also be depleted in the residual lower mantle. Long wavelength lateral temperature contrasts of about 200 K would yield 0.2% density variations, if the thermal expansivity at lower mantle conditions is 10^{-5} K^{-1}. This thermal density contrast is less than the intrinsic chemical contrast, at lower mantle pressures, inferred for upper mantle vs. plausible deep mantle compositions [*Jeanloz*, 1991]. The density difference at lower mantle pressures, between various plausible chemical models of the upper and lower mantle ranges from 2.6 to

5% [*Jeanloz*, 1991]. This is enough to stratify mantle flow.

An increase in SiO_2 or a decrease in MgO content will tend to raise seismic velocities. The effect of FeO depends on its spin state and metallic nature. Assuming that Al_2O_3 stablizes the garnet structure to about 1000 km depth [*Kesson et al.*, 1994; *Jeanloz*, 1991], and assuming further that magma extraction has depleted the lower mantle (presumably during accretional melting) in Al_2O_3 and CaO and that the original mantle was more chondritic than the current upper mantle, then a SiO_2-rich and CaO, Al_2O_3-poor, and U, Th, K-poor, lower mantle is expected. The FeO-budget of the lower mantle depends not only on its melt extraction history but its subsequent interaction with the core and core forming material in its early history. It is, in fact, difficult to imagine how a homogeneous mantle may have formed, particularly considering the efficient extraction of the crust-forming elements upwards and the core-forming elements downwards. Thermal expansion is high at upper mantle pressures; this plus the effects of partial melting means that compositional layers can be breached and potentially mixed with surrounding mantle. Pressure suppresses thermal expansivity and chemical discontinuities can be expected to be more permanent in the deep mantle.

There are various arguments for and against stratified mantle convection. Small intrinsic density contrasts between layers can easily be overcome at lower pressures. The effect of pressure on thermal expansivity makes this more difficult at high pressures. Many of the arguments against stratified convection are actually arguments against the 670 km level being the boundary. These arguments do not apply if the convection interface occurs nearer to 920 km. The possibility of an important geodynamic boundary several hundred kilometers deeper than the major seismic discontinuity at 670 km is consistent with electrical conductivity and viscosity data, as well as with 1D and 3D seismic modeling. For example, the viscosity may rise rapidly below 800-900 km [*Ivins et al.*, 1993]. Layered mantle convection serves to insulate the lower mantle and is less efficient at heat removal than whole mantle convection [*Spohn and Schubert*, 1982]. Consequently, two-layer convection implies a lower mantle depleted of radioactive heat sources [*Spohn and Schubert*, 1982], consistent with the differentiation during accretion model [*Anderson*, 1989].

3.7 Conclusion

The amplitude of dynamic topography predicted by previous viscosity models involving whole mantle flow is much larger than observed. We are unable to find reasonable velocity-density scalings to fit the geoid and residual topography for whole mantle flow models. This is consistent with recent studies on topography [*Phipps-Morgan and Shearer*, 1994; *Thoraval et al.*, 1995; *Stunff and Ricard*, 1995]. We show that the seismic tomography at shallow depths, once corrected for the chemical effects of cratonic roots and thermal cooling of oceanic lithosphere, exhibit slow velocities that are well correlated with uplifted regions at long-wavelengths (l=2,3). The spectrum of residual topography also reveals the shallow origin of dynamic topography. The long-wavelength dynamic topography is controlled by density variations in the upper mantle, whereas, the long-wavelength geoid is controlled by density throughout the mantle. Layered mantle convection stratified at about 920 km provides a self-consistent geodynamic model in explaining the long-wavelength geoid and topography.

Chapter 4 Present-day plate motion constraint on mantle rheology and convection

4.1 Abstract

Large-scale mantle convection, to first order, is a system driven by interior density anomalies, modulated by variable plate thickness and extreme rheology variations at the top of the mantle. The rheological difference between oceanic and continental regions significantly influences the surface velocity. We apply a three-dimensional Newtonian viscous flow model to explain the large-scale present-day plate motions. The density anomalies are derived from seismic tomography and a slab model. With a viscosity difference of a factor of 30-60 between continents and oceans in the upper 90 km of the Earth, we are able to explain both the observed large-scale poloidal and toroidal plate motions. The viscosity difference between continental and oceanic regions has major control on both the poloidal-toroidal kinematic energy partitioning and the pattern of toroidal motion. Nonlinear rheology can help establish toroidal motion. Plate motions can be explained by assuming either layered or whole mantle flow. In order to match the amplitude of observed plate motions, the value of the reference viscosity (corresponding to that of between 400 to 670 km depth) is 1.6×10^{21} Pa s for layered mantle flow and 3.2×10^{21} Pa s for whole mantle flow. However, the predicted net rotation of the lithosphere, from both layered and whole mantle flow models, is very small and cannot account for the amplitude of the net rotation obtained from the plate tectonic models assuming a fixed hotspot reference frame.

4.2 Introduction

Plate tectonics is generally believed to be the result of mantle convection. While several large-scale geophysical observables, such as geoid and topography, can be explained in the context of mantle convection [*Hager*, 1984; *Ricard et al.*, 1984; *Hager et al.*, 1985; *Forte et al.*, 1993; *Wen and Anderson*, 1997b], plate motions remain a puzzle for mantle convection. Plate motions are important in many contexts of mantle dynamics:

1. They are the direct evidence of plate tectonics; only after we have established the relationship between observed plate-like motions and mantle convection models can we understand plate tectonics in the context of mantle convection, and vice versa. Figure 4.1a shows present-day plate motions in the hotspot reference frame from a plate tectonic model [*Gordon and Jurdy*, 1986]. One can decompose these plate motions into poloidal and toroidal motions [*Hager and O'Connell*, 1979], or equivalently, divergence and vorticity [*Forte and Peltier*, 1987]. Figure 4.1b shows the spherical harmonic $l = 1-5$ components of divergence and vorticity obtained from the plate motions shown in Figure 4.1a. Divergence is defined as $\nabla_H \cdot U$ (U is the surface velocity) and represents convergent (negative) or divergent (positive) motions, and vorticity $(\nabla \times U)\cdot\, \hat{\mathrm{r}}$ ($\hat{\mathrm{r}}$ is the radial unit vector) represents the shear motions between plates (negative corresponding to clockwise rotation). Models with radial symmetric viscosity structure predict poloidal motions only [*Hager and O'Connell*, 1981]. Models with temperature and stress-dependent viscosity predict a small component of toroidal motion [*Christensen and Harder*, 1991; *Tackley*, 1993; *Cadek et al.*, 1993; *Zhang and Christensen*, 1993]. The observed toroidal/poloidal ratio is close to unity [*O'Connell et al.*, 1991]. Effects on the lateral variation of viscosity in the lithosphere have also been studied by several authors, with approximate methods [e.g., *Ricard et al.*, 1988; *Stewart*, 1992; *Ribe*, 1992]. However, the origin of toroidal plate motion remains unknown.

2. Plate motions are directly related to the question of the complexity of mantle convection. Are plate-like motions controlled by some "magic" behavior of the

a) Present-day Plate Velocity

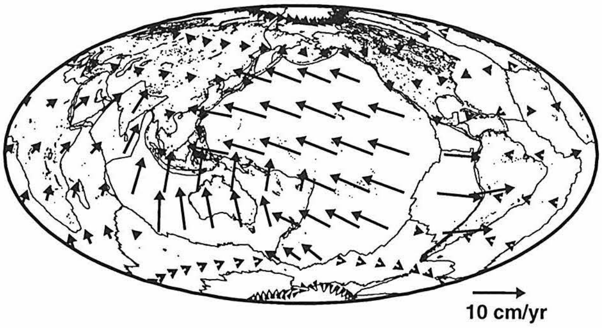

b) Observed Divergence (L=1-5)

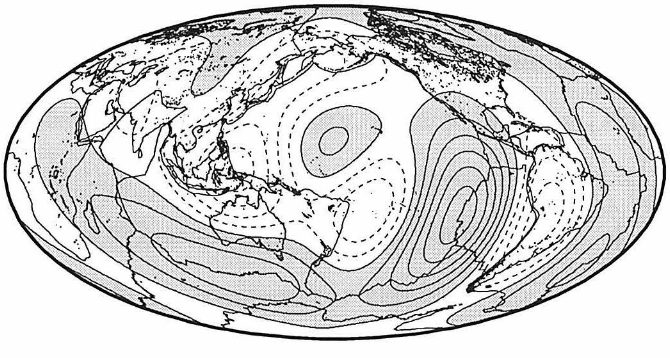

c) Observed Vorticity (L=2-5)

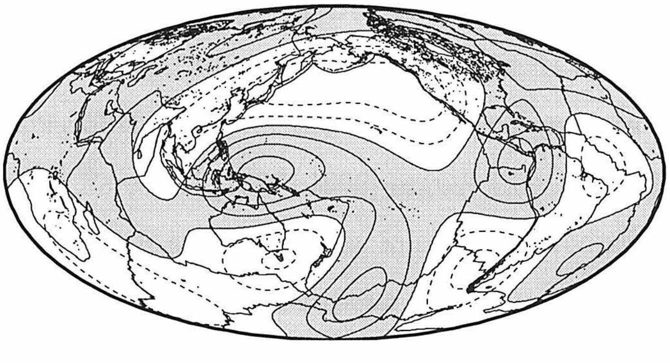

Figure 4.1: a) Surface plate velocity, b) divergence ($l = 1 - 5$), and c) vorticity ($l = 2 - 5$) of surface velocity constructed from the finite rotation poles and angular velocities of *Gordon and Jurdy* [1986] in the hotspot reference frame. See text for the definitions of divergence and vorticity. Positive values of divergence correspond to divergent motion and negative values correspond to convergent motion. Negative values of vorticity correspond to clockwise rotation and positive values correspond to counter-clockwise rotation. Regions with positive values are shaded. Contour interval is 1×10^{-8} rad/yr.

so-called "plates" which is beyond our modeling ability? Or, are plate-like motions controlled by mantle convection modulated by surface boundary conditions? Are the plates controlled by very special rheology, or is simple rheology sufficient to explain large-scale plate behavior? One approach is to define plate geometries a priori and assume plate-like (either observed or to-be-determined) velocity as a boundary condition, regardless of the origin of these plate velocities [*Hager and O'Connell*, 1981; *Ricard and Vigny*, 1989; *Gable et al.*, 1991; *Lithgow-Bertelloni and Richards*, 1995]. The constraint is that the forces or torques induced by the interior density anomalies and those caused by the imposed surface velocity are balanced at the surface of the Earth or at a certain depth in the mantle. Lateral variation of viscosity is usually ignored. One problem with this approach is that the total stress acting on the plate, due to the imposed plate-like velocity, goes to infinity [*Hager and O'Connell*, 1981]. One way around this dilemma is to balance the torques at a certain depth in the mantle [*Hager and O'Connell*, 1981; *Gable et al.*, 1991]. However, the normal forces between plates and the average shear stress at the surface still go to infinity. Another way to deal with this problem is to apply a failure criterion for the lithosphere and mathematically truncate the stress contribution at a certain harmonic degree [*Ricard and Vigny*, 1989; *Lithgow-Bertelloni and Richards*, 1995]. Plates are essentially partly moved with "the finger of God" in this approach. Another approach is to invoke special rheology for the lithosphere to explain the observed plate motions. For example, *Bercovici* [1993, 1996] argues that lithosphere might have a special rheology with dynamic self-lubrication in order to produce plate-like motions. *O'Connell et al.* [1991] and *Olsen and Bercovici* [1991] attribute the kinematic partition of toroidal and poloidal motions to the geometrical effects of the existing plates. On other hand, *Zhong and Gurnis* [1995, 1996] suppose that preexisting faulted plate margins hold the key to the present-day plate motions.

3. Plate motions provide important constraints on surface rheology. Unlike geoid and topography, which place strong constraints on the radial viscosity structure, plate motions place constraints more strongly on the lateral variation of viscosity. For example, weak plate margins [*Lachenbruch and Sass*, 1988] may have a large influence

on plate motions, based on two-dimensional flow models [*Gurnis*, 1989]. *Ribe* [1992] predicts a substantial toroidal component of surface motions by considering a model in which the lithosphere is represented as a thin shell with laterally variable thickness, overlaying a radially symmetric mantle. *O'Connell et al.* [1991] and *Ricard et al.* [1991] claim that at least 1 order magnitude of difference of viscosity between continental and oceanic mantle is required to explain the observed net rotation ($l = 1$ toroidal motion) of the lithosphere in a fixed hotspot reference frame. Plate motions can also place constraints on the absolute value of viscosity in the mantle, whereas geoid and topography can only constrain the relative values of viscosity.

It is also worth mentioning that toroidal surface motion is essentially a three-dimensional problem. Any two-dimensional investigations of lateral variation of viscosity [e.g., *Richards and Hager*, 1989] would have limited application in modeling the toroidal motions in three dimensions. Three-dimensional models can also be constrained by geoid and topography. In this paper we present a new method to calculate three-dimensional Newtonian flow with lateral variable viscosity and test several rheological models for their capability of generating toroidal motions. In the first section we discuss briefly the new method and present several rheological models for a simple slab density model. We will focus on rheological models with large-scale variations, that is, rheological differences between continental and oceanic regions. In the second section we refine the density model to match geoid and surface residual topography [*Cazenave et al.*, 1989]. The density anomalies are derived from residual tomography [*Wen and Anderson*, 1997a] and the presence of slabs in the upper mantle and seismic tomography [*Su et al.*, 1994] in the lower mantle. The predicted plate velocities are presented. We also discuss the net rotation of the lithosphere.

4.3 Three-dimensional Newtonian flow and model experiments

4.3.1 Method

Earth's mantle is assumed to behave as an incompressible Newtonian viscous fluid with negligible Reynolds number. Three sets of equations govern the mantle flow:
Equation of continuity

$$\nabla \cdot U = 0, \tag{4.1}$$

where U is the velocity.
Equations of motion at zero Reynolds number

$$\nabla \cdot \tau + \delta \rho g = 0, \tag{4.2}$$

where τ is the stress tensor, $\delta\rho$, the density anomaly and g, the gravitational acceleration.
Constitutive equation for Newtonian flow

$$\tau = -p + 2\eta\varepsilon, \tag{4.3}$$

where p is the pressure, η, the viscosity and ε, the strain rate tensor.

The appendix gives procedures for solving these equations in spherical coordinates. The horizontal variations of variables are expressed in terms of spherical harmonics. For a radially symmetric viscosity structure, toroidal-poloidal, poloidal-poloidal and toroidal-toroidal equations are decoupled at every spherical harmonic degree and order [*Kaula*, 1975; *Hager and O'Connell*, 1981]. For a structure with lateral viscosity contrast, toroidal and poloidal equations are coupled and equations at every degree or order of the spherical harmonics are also coupled with each other. The coupling coefficients are presented in the appendix. If we truncate the contribution at a certain spherical harmonic degree ($l_{\max}$) and consider the coupling effects for those spherical harmonic degrees ($l \leq l_{\max}$), we can reduce the above three set of equations to a set of linear equations. These linear equations have constant coefficients for a shell with the same form of lateral variation of viscosity and can be solved by standard propagator matrices [*Gantmacher*, 1960] (see appendix for details). The geoid and dynamic topography at various boundaries in the mantle can be easily obtained from Z_3^{lm} terms in the appendix. The procedures of obtaining geoid and topography are presented elsewhere.

The method has been checked by the following procedures:

1. For radially symmetric viscosity, the solutions are in exact agreement with those obtained by traditional propagator matrix method [e.g., *Hager and O'Connell*, 1981].

2. We compare our results with those obtained by the method of *Zhang and Christensen* [1993] for the density perturbation $\delta\rho = \sin \pi z * Y_{11} + Y_{20}$ and viscosity structure $\eta = \eta_0 \ \exp \ (C * \delta\rho)$, where $C = 0.2$, $z = (r - r_i)/(r_0 - r_i)$, r_0 and r_i are the radii of the Earth's surface and the core-mantle boundary, and η_0 is the reference viscosity, and $Y_{11}, Y_{2,0}$ are the normalized spherical harmonics. The correlation coefficients between predicted divergence and vorticity by the two methods are shown in Figure 4.2a and the normalized spectra of predicted divergence and vorticity are shown in Figure 4.2b. The results obtained by the two methods are in excellent agreement.

3. We compare our large-scale predictions of divergence and vorticity with those obtained by *Ribe* [1992] for a three plate model with lateral variation of viscosity in a shell. For comparison, we assume that the lateral variation of viscosity is confined in a thin shell with a thickness of 10 km and the rest of the mantle has uniform viscosity 1. Figure 4.3a shows the lateral variation of viscosity in the thin shell or the "stiffness" $f = (h/a)(\eta(\theta, \phi)/\eta(a) - 1)$, as defined by *Ribe* [1992], as a function of colatitude. The "stiffness" is scaled from the lateral variation of viscosity, and $\eta(\theta, \phi)$ is the viscosity in the shell, $\eta(a)$ is the reference viscosity, h is the thickness of the shell and a is the radius of the Earth. The variation of this "stiffness" is very similar to that used by *Ribe* [1992]. Mantle flow is driven by a surface density contrast of degree and order $(l, m) = (2, \pm 1)$ in the middle mantle ($r = 0.773a$). The predicted divergence

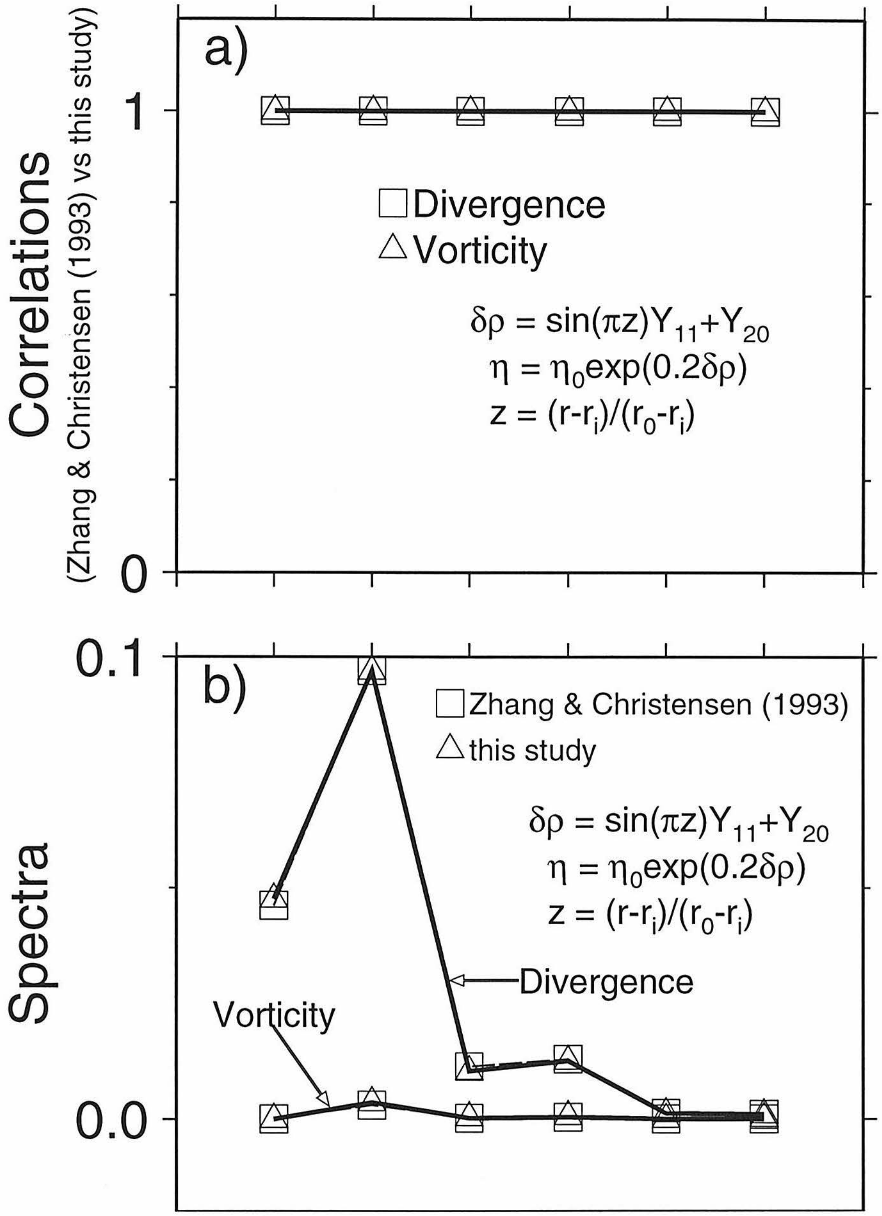

Figure 4.2: Comparisons between the results produced by the method of *Zhang and Christensen* [1993] and those obtained by this study. The distributions of density anomalies and viscosity are shown in the figures. a) correlation coefficients between the predictions by two methods, and, b) comparison of spectra obtained by two methods.

along the meridian $\phi = 0$ and vorticity along the meridian $\phi = 90^0$ are shown in Figures 4.3b and 4.3c. A truncation degree of $l_{\max}= 12$ is used in our calculation and a truncation degree of $l_{\max}= 128$ is used by *Ribe* [1992]. Thus small-scale features are missing in our results. Note, however, that at long wavelengths, we obtain very good agreement between the two methods (see Figure 8 of *Ribe* [1992]).

4.3.2 Thermal models

Oceanic lithosphere.

Several models have been proposed to explain the heat flow and bathymetry data in the oceanic regions. The increase in ocean depth away from spreading centers varies linearly, on average, with the square root of age of the oceanic plates up to 70-80 m.y. [*Parsons and Sclater*, 1977], as predicted by both the half-space cooling model [*Turcotte and Oxburgh*, 1967] and the plate model [*Parsons and Sclater*, 1977; *Stein and Stein*, 1992]. The plate model can fit the average ocean data beyond 70-80 m.y. Many mechanisms have been proposed to explain the departure of the observed ocean depth from the trend predicted by the half-space cooling model. For example, small-scale convection [*Richter*, 1973], hotspots [*Heestand and Crough*, 1981], viscous heating [*Schubert et al.*, 1976], etc. For the purpose of our study the differences between these models are rather small. The forces generated by the cooling of oceanic lithosphere are small compared to those resulting from density variations in the mantle. The plate model of *Stein and Stein* [1992] is used in the oceanic regions. The temperature $T(x,z)$ as a function of distance x from the ridge and depth z below the seafloor is given by

$$T(x,z) = T_m[z/a + \sum_{n=1}^{\infty} c_n \exp(-\beta_n x/a) \sin(n\pi z/a)],$$

where a is plate thickness (95 km), T_m is basal temperature (1450^o C) and

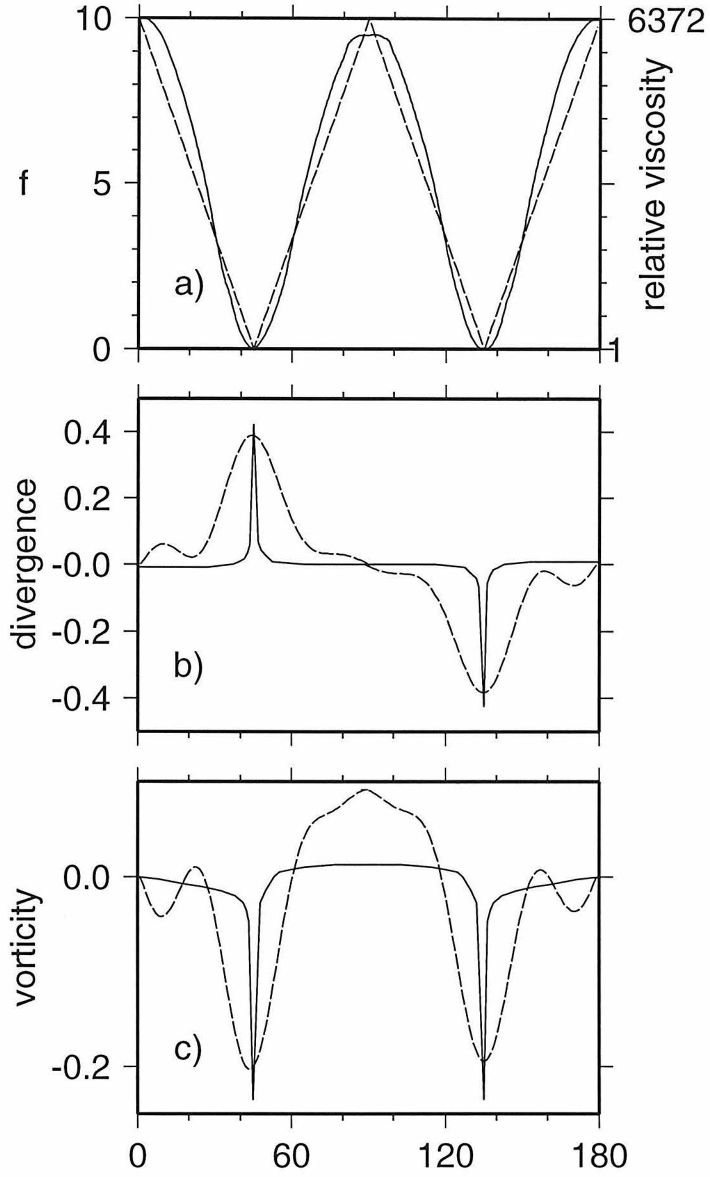

Figure 4.3: Effects of large lateral variations on the surface velocity field, for a three-plate model, as defined in *Ribe* [1992]. a) "stiffness" $f(\theta)$ or relative viscosity in a thin shell of thickness of 10 km; b) profile of surface divergence along the meridian $\phi = 0$; and c) profile of radial vorticity along the meridian $\phi = 90^0$. Surface divergence and radial vorticity are shown in units of $g\sigma/\eta_0$. The flow is driven by a surface density contrast of degree and order $(2, \pm 1)$ in the middle mantle. Results of *Ribe* [1992] are indicated by heavy lines.

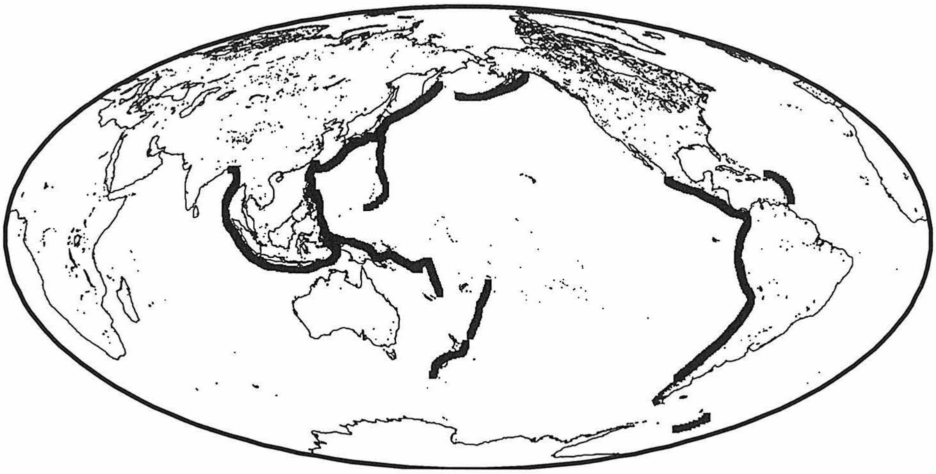

Figure 4.4: Locations of present-day subduction zones.

$$c_n = 2/(n\pi),\ \beta_n = (R^2 + n^2\pi^2)^{1/2} - R,\ R = va/(2\kappa),$$

where thermal diffusivity $\kappa = k/(\rho_m C_p)$, k is thermal conductivity (7.5×10^{-3} cal K^{-1} cm^{-1} s^{-1}), ρ_m is mantle density (3330 kg m^{-3}) and C_p is specific heat (0.28 cal g^{-1} K^{-1}). The thermal expansion coefficient $\alpha = 3.28 \times 10^{-5}$ K^{-1} and the digital ocean age map by *Müller et al.* [1993] are used. Continents are assumed to be equivalent to ridges in terms of density in the upper 90 km. The upper 90 km is divided into nine layers each with thickness of 10 km.

Density anomalies in the mantle.

The density anomalies in the mantle are assumed to be only those related to subducting slabs. The locations of slabs are shown in Figure 4.4. Slabs are assigned a thickness of 128 km and density contrast of 0.067 g/cm^3, regardless of age. They are assumed to sink vertically into the mantle and to be confined to the upper mantle. This slab model is expanded into spherical harmonic degrees. The upper mantle is divided into 11 layers of thickness 50 km. This density model in no way represents all the thermal anomalies in the real Earth. However, it can be used to test the viscosity structure of the mantle at high spherical harmonics.

4.3.3 Viscosity structure of the Earth

Several mechanisms may cause lateral variations in viscosity: (1) temperature dependence, (2) stress dependence, and (3) chemical differences. Models of mantle flow with temperature-dependent viscosity in a three-dimensional Cartesian geometry [*Christensen and Harder*, 1991; *Tackley*, 1993] and spherical geometry [*Zhang and Christensen*, 1993] and with stress-dependent viscosity [*Cadek et al.*, 1993; *Zhang and Christensen*, 1993] are unable to generate sufficient toroidal energy to be compatible with the observations. In this study we consider temperature- and stress-dependent viscosity to be second-order effects in generating toroidal plate motions at the surface. The extreme lateral variations in viscosity probably occur at shallow depths, where the rheological difference of continental and oceanic regions is obvious. Figure 4.5 shows the regionalization of continents, oceans and plate margins in the present-day configuration. We assume viscosity variation exists only in the upper 90 km; the rest of the mantle has radially symmetric viscosity structure. To resolve weak plate margins might require a very high truncation degree in spherical harmonic domain, which is very difficult for our technique to handle. Note that the number of linear equations grows as $l_{\max}^2$ and the calculation grows as $l_{\max}^6$. Thus we will focus on testing rheological models with long-wavelength variations in viscosity. One obvious candidate is the rheological difference between oceanic and continental regions, as is obvious from seismic images [e.g., *Zhang and Tanimoto*, 1993; *Grand*, 1994; *Polet and Anderson*, 1995]. All the calculations will be done with truncation degree $l_{\max}= 12$, and we will only consider the components of degrees ($l \leq 5$), since they are affected very little by neglecting the coupling effects of small-scale structures, as we will show later.

We start from a very simple model with stiff "continents" overlaying a uniform mantle. "Continents" include thick cold cratons as well as noncratonic areas. They also include crust and upper mantle. "Continents," however, are assumed to have

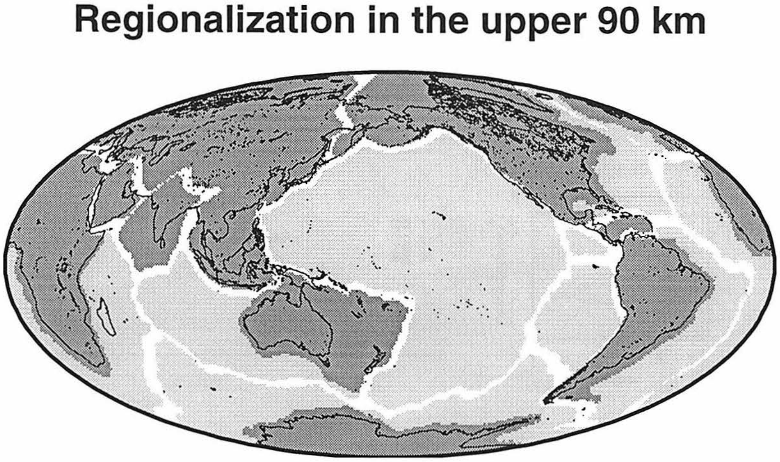

Figure 4.5: Regionalization of tectonic regions. The upper 90 km is divided into three regions: oceans (light gray), plate margins (white), and continents (dark gray).

uniform viscosity and uniform thickness (90 km). Thus lateral variations in viscosity exist only in the upper 90 km of the mantle. The schematic representation of the viscosity structure is shown in Figure 4.6a. The predicted toroidal/poloidal spectrum ratios for this model reach about 40%. However, no significant correlations between predicted and observed vorticity are found (Figure 4.6a). Figure 4.6b shows results for a model similar to model a but with a stiff lower mantle (model b). Model b predicts less toroidal motion, but the correlation becomes better at degree $l = 6$. Overall, a high-viscosity lower mantle has little effect on the prediction of plate motions. The toroidal energy predicted by models a and b cannot account for the observations.

Significant changes appear for the model (model c) with a weak asthenosphere (Figure 4.6c), which is simulated as a channel with low viscosity. Plates are decoupled efficiently from the rest of the mantle through this weak asthenosphere. Significant toroidal plate motions are predicted. As shown in Figure 4.6c, the toroidal/poloidal spectrum ratios are around 0.8-1.2, very close to observations. The predicted and observed vorticity patterns correlate well at degrees $l = 2 - 6$. The above model experiments indicate that plates with a viscosity difference between continental and oceanic regions can be driven by the cooling of the oceanic plates and subducting slabs and can move in the right direction, if they are efficiently decoupled from the rest of the mantle. Both the viscosity difference of the continental and oceanic regions

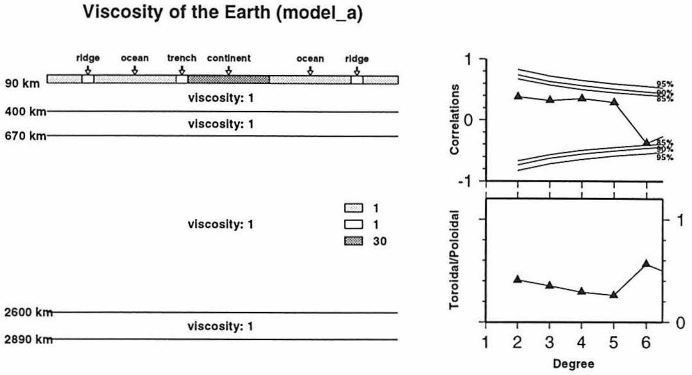

(a) Viscosity model for model a, where uniform viscosity mantle is overlain by stiff continents; right bottom figure shows the ratio of predicted spectra of surface toroidal to poloidal motions; right top figure shows the correlation coefficients of predicted and observed vorticity. The buoyancy forces are assumed to be slabs only.

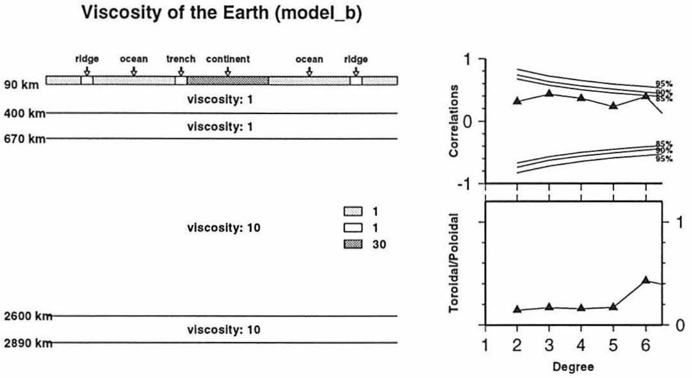

(b) Same as Figure 4.6a, except for model b, which has a high viscosity lower mantle.

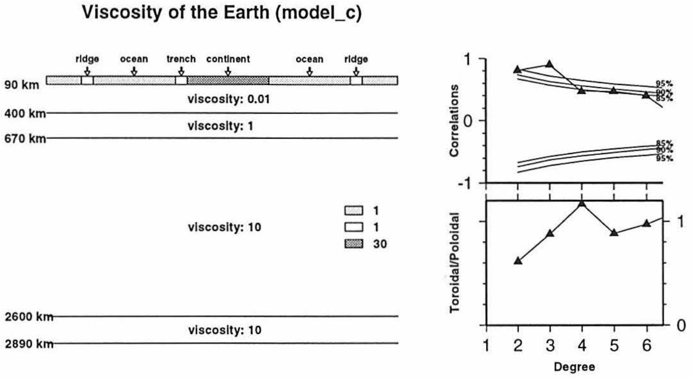

(c) Same as Figure 4.6a, except for model c, which has a high viscosity lower mantle and a weak asthenosphere below the lithosphere. Note the ratio of predicted spectra of toroidal/poloidal velocities and the good correlations between predicted and observed vorticity.

Figure 4.6: Various viscosity models for the Earth.

and a low-viscosity asthenosphere are important in generating plate motions at the Earth's surface.

4.3.4 Truncation effects

The coupling effects among spherical harmonic degrees $l < l_{\max}$ are exactly predicted by our method, but the effects of small-scale structures on the large-scale predictions are still unknown. It is worthwhile investigating the effects of using different truncation degrees ($l_{\max}$). Very little change in the prediction of models a-c is observed. Figure 4.7 shows the correlation coefficients and percentage change of spectrum between the predicted divergence and vorticity with truncation degree $l_{\max}= 12$ for model c and those with different truncation degrees. The predictions at two extreme degrees ($l = 1, 5$) are shown. The correlation coefficients are between 0.99 and 1 for both divergence and vorticity, and the spectra have about a maximum of 4% variations. This experiment indicates that, for the viscosity structure we consider, the density anomalies at $12 < l_{\max} \leq 24$ contribute very little to the large-scale divergence and vorticity. It is not surprising that the couplings between small-scale density anomalies and small-scale viscosity variation to the large-scale surface velocity are rather small because the power of both density anomalies and lateral variation of viscosity decrease rapidly with spherical harmonic degree l. It should be mentioned that the slab model has smaller scale structures than the tomographic models. The truncation effects are expected to be smaller for the real Earth. Considering the uncertainties of the density model, we believe that the prediction with truncation degree $l_{\max}= 12$, the highest degree of our density (tomographic) model, is good enough and will be robust for predicting the plate velocities at degrees $l = 1 - 5$. For the purpose of mimicking the large-scale effects of stress-dependent viscosity, we will include "weak zones" in the plate margins in the following calculations. It should be mentioned that truncation effects are larger for purely "weak zones" models than for "ocean/continent" models. The purpose here is purely for mimicking the stress-dependent viscosity, since stresses are likely to be large at plate margins and will decrease the effective

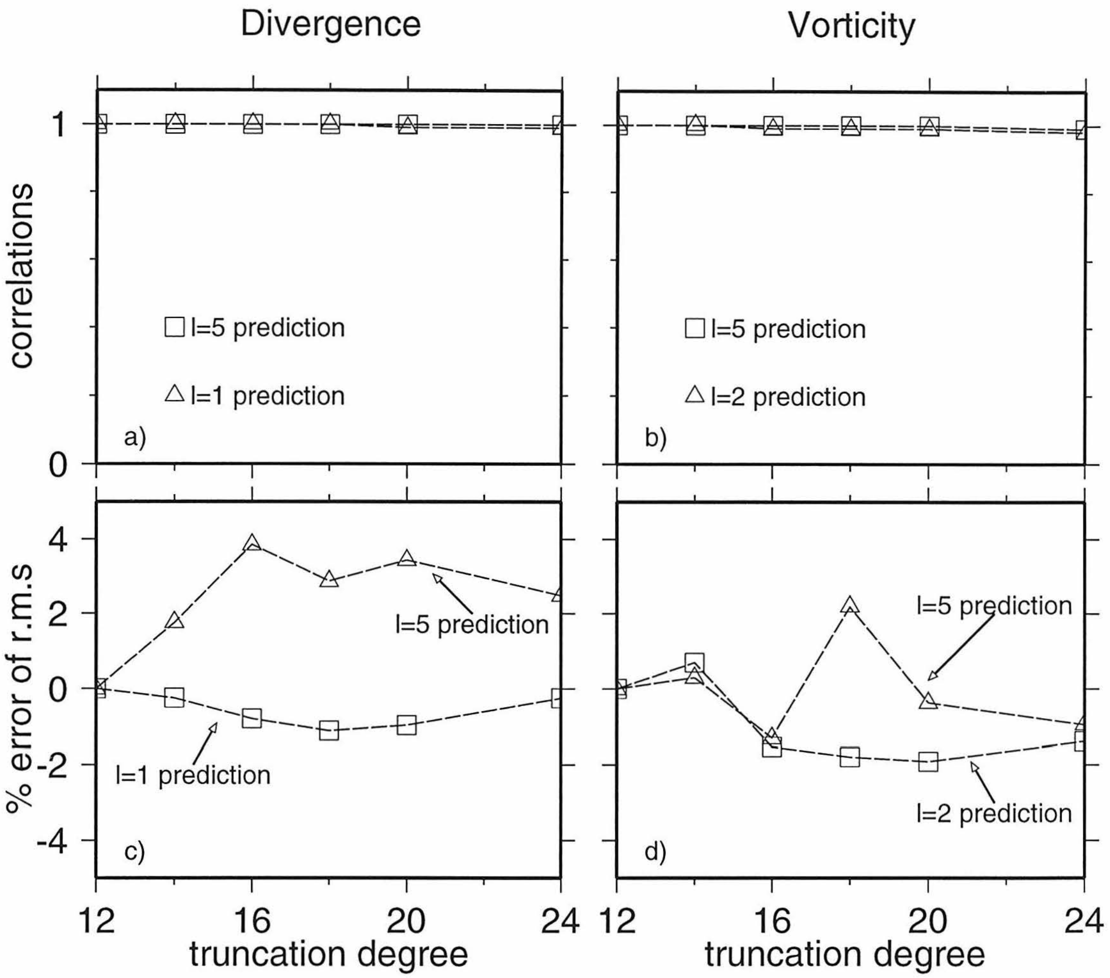

Figure 4.7: Correlations and error of r.m.s with respect to predicted divergence and vorticity using truncation degree ($l_{max} = 12$) for those with different truncation degrees.

viscosities. Equivalently, we impose a gradient of stress-dependent viscosity variation by truncating "weak zones" at low degree.

4.4 Geoid, topography, and plate motion constrained mantle convection

In this section we refine our density model to fit the geoid and residual topography.

4.4.1 Refined density anomalies in the mantle

The long-wavelength ($l = 2-3$) geoid and residual topography [*Cazenave et al.*, 1989] are explained successfully by a density model derived from residual tomography [*Wen and Anderson*, 1997a] in the upper mantle and seismic tomography in the lower mantle for layered mantle flow [*Wen and Anderson*, 1997b]. The amplitude of residual topography places strong constraints on the velocity-density scaling in the shallow mantle. We apply the same velocity-density scalings shown in our previous model at $l = 2 - 3$. At degrees $l = 4 - 9$, geoid and velocity divergence correlate strongly with subducting slabs [*Hager*, 1984; *Forte and Peltier*, 1991]. These slab signals in the upper mantle are missing in the current generation of seismic tomography [*Forte and Peltier*, 1991]. The predictions of geoid and surface velocity divergence based on seismic tomography are generally not good at those degrees. The density anomalies in subducting slabs are somewhat uncertain. We derive a hybrid density model in the upper mantle by adjusting the relative weights of density anomalies of subducting slabs and residual seismic tomography. This is similar to the approach of *Forte and Peltier* [1991], except that the residual tomography is used in the upper mantle in our approach. Our criterion for choice of parameters for the density models is to match the geoid, residual topography and surface velocity divergence with the observations. We need to test whether we can match the surface vorticity for a given viscosity structure, in terms of magnitude and pattern.

The velocity-density scalings for degrees $l = 4 - 12$ are shown in Figure 4.8. The subducting slabs are assumed to sink vertically into the upper mantle and to be confined in the upper mantle (the dip angle of subducting slab is of little consequence at large scale; however, it does modify the inferred thickness of the slab, which, equivalently, is considered by changing the density contrast of the slab). The thickness of subducting slabs is assumed to be 128 km, corresponding to the thickness of a vertically sinking mature slab. The density contrasts in different subduction zones are listed in Table 4.1. The degree $l = 4-12$ components of this slab model are used.

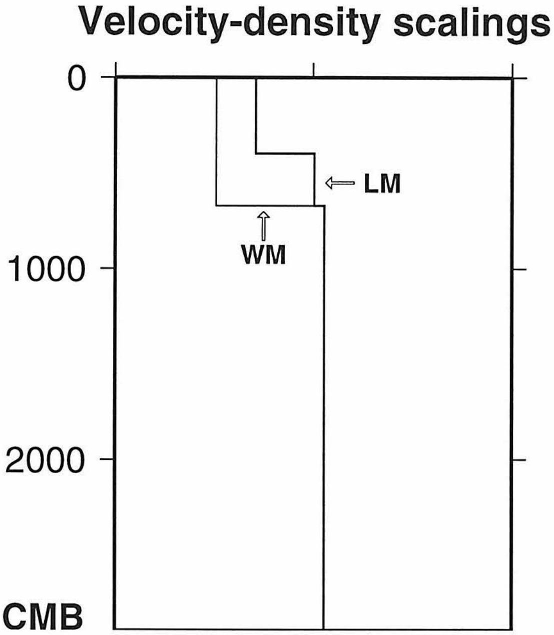

Figure 4.8: Velocity-density scalings at $l = 4 - 12$ for models assuming layered mantle flow (LM) and whole mantle flow (WM). These scalings for model (LM) are obtained by matching the amplitude of observed geoid and residual topography; and those for model (WM) are obtained by matching the amplitude of geoid only.

Table 4.1: Density contrast of slabs (10^{-3} g/cm^3)

Subduction Zone	LM	WM
Java	32	18
New Herbrides	118	80
Tonga	16	64
Mariana	32	18
Ryukyu	45	18
Kurile	45	18
Aleutian	45	45
Middle America	32	64
Caribbean	32	64
Peru-Chile	110	96

The Earth is divided into 43 layers: 9 layers in the upper 90 km with thickness of 10 km, 12 layers in the rest of the upper mantle, and 22 layers in the lower mantle. We test two models for mantle convection: layered mantle and whole mantle flow. Again, all the calculations are done with truncation degree $l_{\text{max}}= 12$ and only prediction at degrees $l = 1 - 5$ will be discussed.

4.4.2 Buoyancy driven plate motions

The layered mantle convection model used here is the same as we used in explaining the long-wavelength geoid and residual surface topography [*Wen and Anderson*, 1997b], except that now there is strong lateral variation of viscosity in the upper 90 km of the mantle. The schematic representation of viscosity structure is shown in Figure 4.9, where both the viscosity contrast between continental and oceanic regions and "weak zones" are considered. The magnitude of the viscosity contrast between continental and oceanic regions is chosen by matching the ratio of the predicted vorticity and divergence to those observed. Mantle flow is assumed stratified at 920 km, rather than at 670 km. There is little difference in this case, however, for the present purposes.

The predicted divergence and vorticity of surface velocity (Figures 4.10a-4.10c) agree well with the observations. The divergent motions at ridges and convergent motions at subduction zones and the magnitudes of those rates are well predicted (see Figure 4.1b). The clockwise rotation along the San Andreas fault, Aleutian trench, Ryukyu-Kurile trench, south of south America and South Africa and counter-clockwise rotation in north Australia, boundary between North America and Cocos plates and circum-Pacific regions and the magnitude of those rotations are also well predicted by our model. The correlation coefficients between predicted surface divergence and vorticity with those observed are shown in Figure 4.11. There are good correlations up to $l = 10$ for surface divergence, up to $l = 6$ for surface vorticity. The breakdown at degree $l = 6$ could be due to the neglect of density anomalies at degrees $l > 12$. Since vorticity results from coupling of modes and divergence is mostly caused

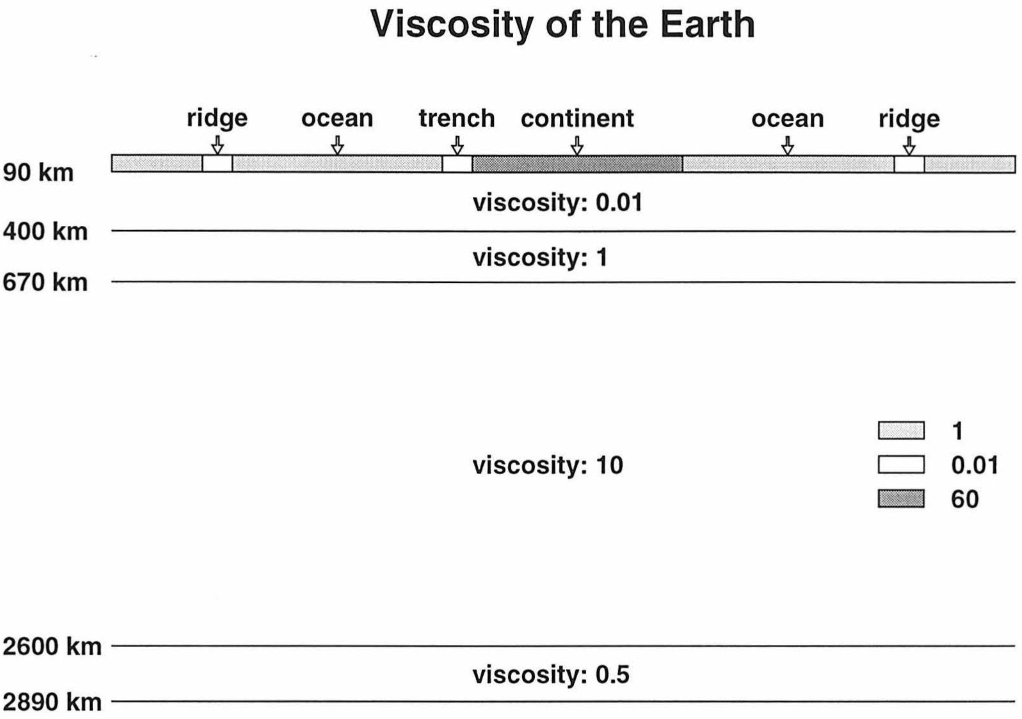

Figure 4.9: Viscosity model used to predict surface velocity field, assuming layered mantle flow, stratified at 920 km. For the model assuming whole mantle flow, the relative effective viscosity of "continents" is 30.

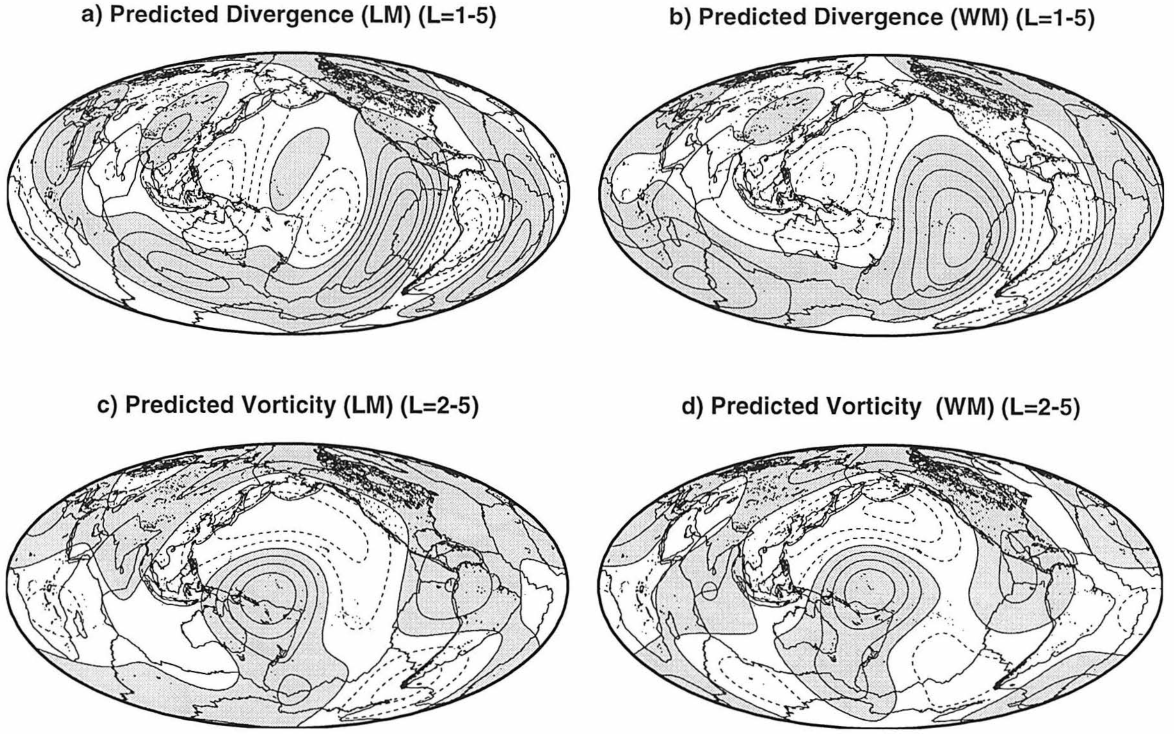
a) Predicted Divergence (LM) (L=1-5)

b) Predicted Divergence (WM) (L=1-5)

c) Predicted Vorticity (LM) (L=2-5)

d) Predicted Vorticity (WM) (L=2-5)

Figure 4.10: Predicted divergence ($l = 1-5$) and vorticity ($l = 2-5$) for surface velocity field for models assuming layered (LM) and whole (WM) mantle flow. Regions with positive values are shaded. Contour interval is 1 $\times 10^{-8}$ rad/yr.

by the density at the same mode, truncation affects the prediction of vorticity more than that of divergence. The reference viscosity (corresponding to the viscosity in 400 - 670 km depth interval) is 1.6 $\times 10^{21}$ Pa s for the layered mantle flow model.

The predicted divergence and vorticity assuming whole mantle flow are also shown in Figures 4.10b and 4.10d. The density contrasts in different subduction zones are listed in Table 4.1 and the velocity-density scalings are shown in Figure 4.8. This density model is only constrained by geoid data. The predictions do not match the observations as well as those assuming layered mantle flow. This is because significant contribution comes from density anomalies in the lower mantle, which have less correlation with the surface divergence. Of course, one can argue that seismic tomography in the lower mantle suffers the same problem as those we claim in the upper mantle, and one can apply the same corrections as we do in the upper mantle. One can probably find a different viscosity structure to make the surface velocity more sensitive to the upper mantle anomalies. The fitting of divergence and

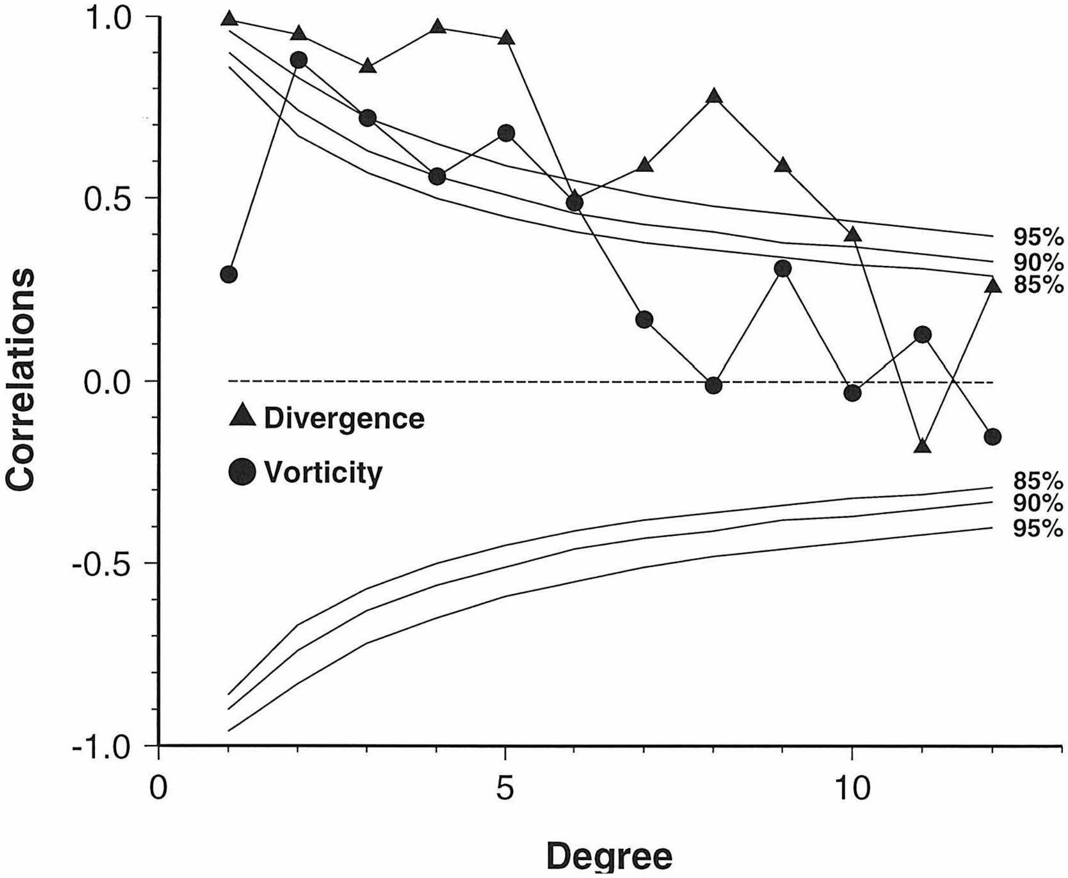

Figure 4.11: Correlation coefficients between observed divergence and vorticity and those predicted for model LM, assuming layered mantle flow.

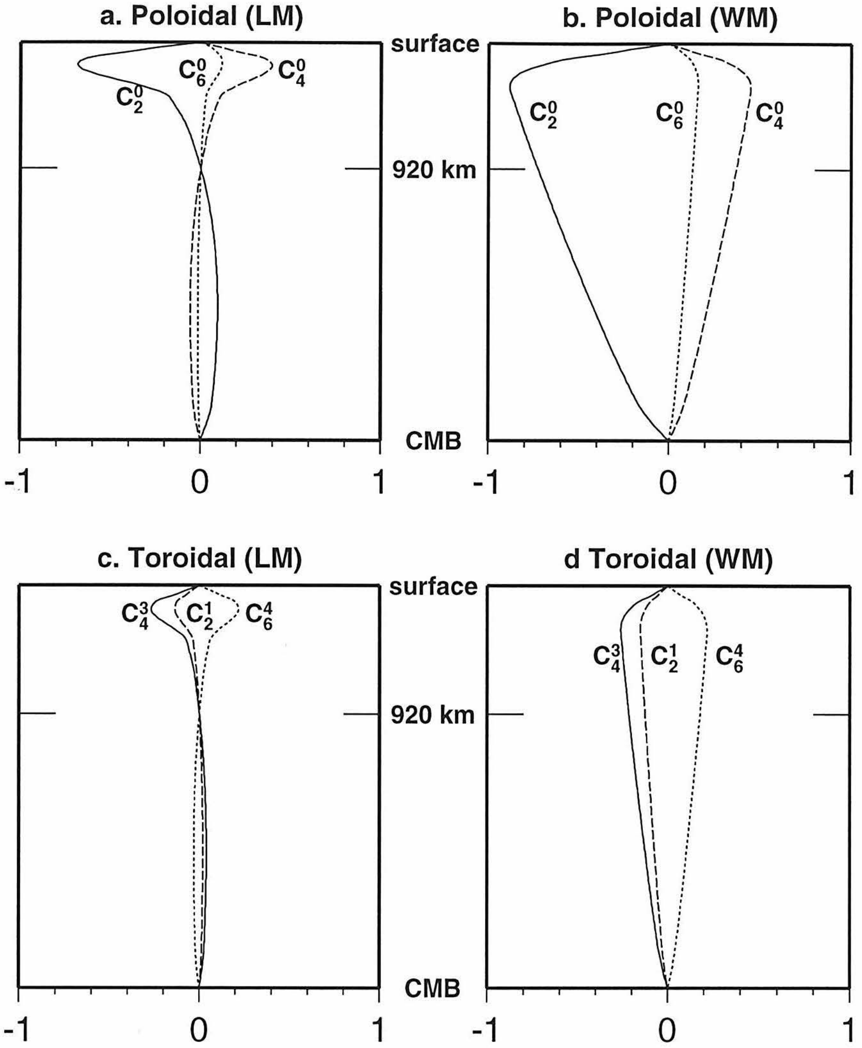

Figure 4.12: Kernels for surface poloidal and toroidal motions for a density load Y_2^0 in the mantle. The viscosity models are the same as those used in Figure 4.10.

vorticity can then be improved significantly. The magnitude of the predicted surface velocity does not constrain the style of mantle convection since it is scaled by the reference viscosity, which is not known exactly. The relative viscosity of "continents" (top of the upper mantle) with respect to that of "oceans" is chosen to be 30 in order to match the power of toroidal and poloidal motions. The reference viscosity is now 3.2×10^{21} Pa s, twice that which was used for layered mantle flow model.

The poloidal and toroidal velocity kernels are shown in Figure 4.12 for the viscosity structures used to predict the divergence and vorticity in Figure 4.10. Those kernels represent the responses of surface poloidal and toroidal motions at certain spherical harmonic degrees and orders for a $Y_{2,0}$ load at a certain depth. Only responses at some modes are shown in the figure as an illustration. Besides a pronounced contribution to $Y_{2,0}$ divergence, significant contributions can also be found at other modes. On the other hand, little contribution is found at degree $l = 2$ for vorticity. Significant contributions come from the density anomalies in the upper mantle region for both layered mantle and whole mantle flow models.

It should be clarified that, in the above models, it is the viscosity difference between continental and oceanic regions, not the "weak zones," that controls the main feature of the predictions. Figure 4.13 shows the predicted surface divergence and vorticity for the density and viscosity models, used in Figures 4.10a and 4.10c, except that no "weak zones" are included. The main features of observed vorticity are well predicted, although the correlations between observations and predictions are slightly lower than those from models with weak plate margins. Models with "weak zones," with this truncation degree $l_{\max}= 12$, only predict a small portion of the observed vorticity.

4.4.3 Net rotation of the lithosphere?

The plate reconstruction models by *Gordon and Jurdy* [1986] and model AM1-2 by *Minster and Jordan* [1978] are based on the assumption that hotspots are fixed and they use the hotspot reference frame. There are significant net rotation motions of lithosphere with respect to hotspots for both models. The net rotation reaches 0.11 degree/m.y. around a pole situated at 37^0E and 40^0S for the model by *Gordon and Jurdy* [1986] and 0.26 degree/m.y. around 68^0E and 53^0S for the model AM1-2 [*Minster and Jordan*, 1978]. This differential net rotation is sometimes interpreted as the net rotation of the lithosphere with respect to the lower mantle.

The rigid body rotation of the Earth is unconstrained by viscous flow. However, the differential net rotation of Earth's surface with respect to other parts of the mantle is constrained. The predicted net rotation (degree $l = 1$ component of toroidal motion) of the lithosphere with respect to the core-mantle boundary for each model

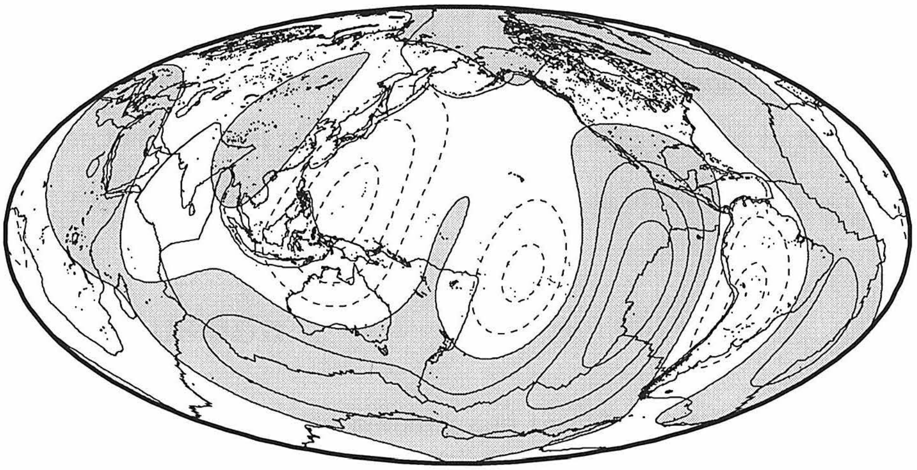
a) Predicted Divergence (LM) (L=1-5)

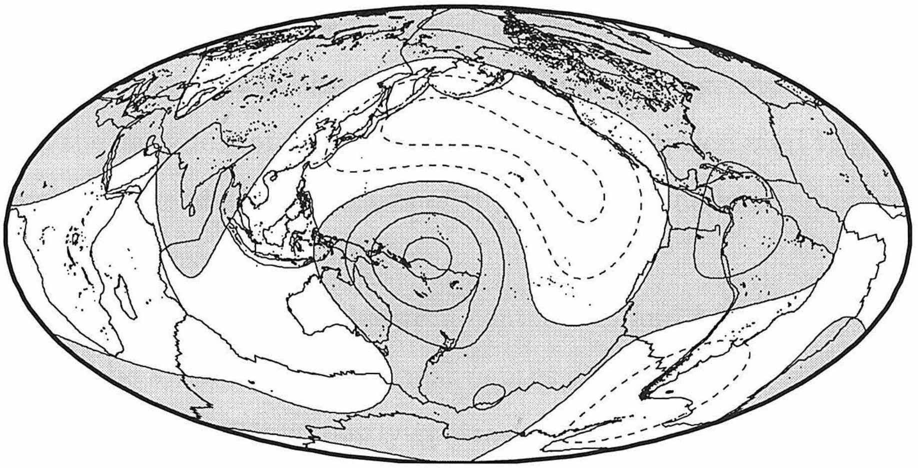
b) Predicted Vorticity (LM) (L=2-5)

Figure 4.13: Same as those in Figures 4.10a,c for model LM, except that plate margins have same viscosity as oceans, i.e., only the viscosity contrast between "continents" and "oceans" is present in the upper 90 km.

used in Figure 4.10 is very small (about 1% of observed net rotation with respect to hotspots). This is also true for the net rotation of the lithosphere with respect to other internal boundaries in the mantle and for the convection models assuming layered mantle or whole mantle flow. The predicted net rotation certainly depends on the viscosity models. The lateral variation of viscosity in the deep mantle will have significant effects on the net rotation of the Earth's outer shell. It is unclear, at this stage, whether temperature- and stress-dependent rheology in the deep mantle can produce the net rotation of the Earth's surface, as observed in the hotspot reference frame, or whether the concept of fixed hotspots is in error.

4.5 Discussion

Although large-scale observed poloidal and toroidal plate motions are well predicted by our model, we have ignored such effects as temperature-dependent viscosity, nonlinear rheology and compressibility in the deep mantle. The lateral variations of viscosity in the deep mantle will certainly affect the prediction, although they are unlikely to be very important in predicting surface plate motions [*Zhang and Christensen*, 1993]. It should also be kept in mind that our model is simplified. For example, the thickness of the plate is purely an assumption, and there are many possible explanations about the causes of the rheological difference between continental and oceanic regions:

1. The viscosity difference between continental and oceanic regions shown in our model could be a reflection of different depths of the lithosphere beneath continental and oceanic regions. The viscosity contrast between continental and oceanic regions is the integrated effect of crust and top of the upper mantle.

2. The viscosity difference between continental and oceanic regions could be the effects of presence of cratons in the continental regions (integrated effects of cratons and younger areas). Cratons appear cold and extend deep in the mantle [*Polet and Anderson*, 1995]. They also affect temperatures and convection in the underlying mantle. Future study on short-wavelength plate motions might help distinguish this

possibility.

3. The viscosity beneath continental regions is large compared with that beneath oceanic regions. Viscosity is controlled by composition, temperature, volatile content, and extent of partial melting. It is unclear, at this stage, how those factors affect viscosity.

Although the interpretation of our results has ambiguities, the viscosity contrast between continental and oceanic regions is necessary to produce the correct pattern of toroidal plate motions. We tested rheological model with oceans having 60 times higher viscosity than continents. Not only are no correlations found between predicted and observed vorticity, but correlations between predicted and observed divergence are degraded significantly.

It is important, for the study of mantle convection, to take into account a realistic distribution of surface geology and density anomalies. Despite the simplicity of our model, it can provide considerable insight into some important aspects of the study of the mantle convection:

1. The shallow mantle seems to be very important in controlling mantle dynamics. Density anomalies at shallow depths contribute significantly both to plate velocity (Figure 4.12) and dynamic surface topography [*Wen and Anderson*, 1997b]. The lateral variations of viscosity at shallow depths appear to be important in controlling the plate velocity at the surface of Earth. The complexity of the shallow mantle still needs to be sorted out.

2. Large-scale plate motions can be explained in terms of mantle convection with simple rheologies. The observed plate motions are controlled by mantle rheology and should not be treated as boundary conditions in modeling of mantle convection. With improving knowledge and confidence about the interior structure of the Earth and with more computational power, it should be possible to predict small-scale plate motions.

3. Since the model presented here is dynamically self-consistent and can account for the normal forces across the plate boundaries, it will be useful for detailed study of intraplate stresses and mantle driving forces. The observation of intraplate deviatoric

stress will place strong constraints on the dynamics of the mantle.

4. It is possible, by applying the model presented here, to realistically simulate self-consistent, time-dependent mantle convection and compare with geophysical and geological observations such as past plate reconstructions, sea level change, etc.

4.6 Concluding remarks

1. We have provided a convective explanation for the present-day plate kinematic observations as well as for the toroidal/poloidal ratio. Large-scale plate motion is the result of mantle convection driven by internal density anomalies and modulated by extreme lateral variation of viscosity near the surface. Continental area, the distribution of "continents," and the length and distribution of subduction zones appear to be important in controlling the directions and magnitudes of the surface plate velocities. Convection can drive the plates at the right magnitudes and directions suggested by plate tectonic models.

2. The viscosity contrast between continental and oceanic regions, broadly defined, is the major control on the surface velocity field. Both layered mantle and whole mantle convection models, with continental regions having an effective integrated viscosity about 30-60 times larger than oceanic regions (assuming 90 km thick plates), are able to predict the correct patterns of surface poloidal and toroidal velocities and can account for the observed ratio of poloidal-toroidal motion. Weak asthenosphere tends to decouple the plates from the rest of the mantle and reinforces the generation of surface toroidal motion. To first order, large-scale mantle convection may be a very simple system governed by Newtonian or stress-dependent viscosity flow with radial and lateral variations of viscosity due to chemical or rheological differences.

3. The reference viscosity (corresponding to that of the 400 - 670 km depth interval) is 1.6×10^{21} Pa s assuming layered mantle flow and 3.2×10^{21} Pa s for whole mantle flow.

4. Mantle convection models, with lateral viscosity contrasts between continental and oceanic regions, predict very little net rotation of the lithosphere with respect to

the rest of the mantle, which is not consistent with plate tectonic models using the hotspot reference frame.

Chapter 5 A two-dimensional P-SV hybrid method

5.1 Abstract

A P-SV hybrid method is developed for calculating synthetic seismograms involving two-dimensional localized heterogeneous structures. The finite-difference technique is applied in the heterogeneous region and generalized ray theory solutions from a seismic source are used in the finite-difference initiation process. The seismic motions, after interacting with the heterogeneous structures, are propagated back to the Earth's surface analytically with the aid of the Kirchhoff method.

5.2 Introduction

The core-mantle boundary (CMB) and adjacent regions play a fundamental role in the mantle and core dynamics and resolving the lateral variations of seismic structure in this region is crucial to understanding the region's thermal, chemical and dynamical behavior. Many seismological observations have suggested the existence of small scale heterogeneities in the lowermost mantle. For example, the decay rate of the diffracted P waves [*Alexander and Phinney*, 1966] and the precursors to PKP [*Cleary and Haddon*, 1972; *Cormier*, 1995] have been interpreted as results of scattering by seismic heterogeneities in the lowermost mantle, although the precise nature of those scatterers has not been known. *Doornbos* [1976, 1978, 1988] show that the topographic relief of the core-mantle boundary with scale lengths of about 10-20 km and an amplitude of several hundred meters offers an equally feasible explanation for the observed precursors to PKP phase. The complexities of SKS and SPdKS phases sampling non-circum-Pacific regions in the core-mantle boundary region have been interpreted in term of the presence of ultra low velocity layers just above the core-mantle boundary, with a thickness of tens of kilometers [*Garnero et al.*, 1993; *Garnero and Helmberger*, 1995, 1996; *Helmberger et al.*, 1996]. The presence of a low seismic velocity layer is also invoked to explain the precursor to the PcP phase recorded in California from events in Fiji [*Mori and Helmberger*, 1995]. Rapid variation of waveforms of those phases from event to event strongly suggests that these structures rapidly vary with length scales which are very small compared to the length of the ray path.

Both numerical and analytical methods have difficulties in handling this type of wave propagation. Numerical methods (e.g., finite-difference [*Alterman and Karal*, 1968; *Boore*, 1972; *Virieux*, 1984] and finite element [*Lysmer and Drake*, 1972]) require massive computer memory and have been limited to wave propagation at small distances and to low frequency modeling [e.g., *Igel and Weber*, 1996], even though they can handle wave propagation in heterogeneous media. Analytic methods (e.g., the generalized ray theory [*Helmberger*, 1968], the WKB method [*Chapman*, 1976] and the reflectivity method [*Müller*, 1985]), on the other hand, can only deal with one-dimensional models. Even though some modifications of these methods enable them to deal with wave propagation in dipping layered structures [*Hong and Helmberger*, 1978] or smooth boundary structures [*Helmberger et al.*, 1996; *Liu and Tromp*, 1996], these methods cannot be applied to wave propagation in heterogeneous media.

In this chapter, we combine advantages of both numerical and analytical methods and develop a hybrid method by applying a finite-difference technique in heterogeneous regions and analytical methods outside. The generalized ray theory solutions are interfaced with the finite-difference calculation and synthetic seismograms at the Earth's surface are obtained from interfacing the output of the finite-difference calculation with WKB Green's functions using Kirchhoff theory. The staggered grid finite-difference scheme [*Virieux*, 1986] is used to handle the fluid-solid interface.

5.3 A two-dimensional P-SV hybrid method combining generalized ray theory, finite-difference technique, WKB and Kirchhoff theory

The P-SV wave propagation problem is illustrated in Figure 5.1a, where we assume the Earth flattening approximation. The heterogeneous region is bounded by a box, where a finite-difference technique is applied. The generalized ray theory (GRT) solutions are interfaced with the finite-difference (FD) calculation in the shaded regions in Figure 5.1b. The wavefields are output from the finite difference calculation just below the core-mantle boundary, which are indicated by empty triangles. The solutions in solid triangles are calculated directly by the generalized ray theory, since those regions are affected very little by the presence of heterogeneities. The synthetics at the surface of the Earth are obtained by applying the Kirchhoff method to interface the output of receivers (triangles in Figure 5.1a) with WKB Green's functions. Interfacings of these motions are discussed in the next two subsections.

5.3.1 GRT-FD interfacing

Shtivelman [1985] and *Emmerich* [1989] present one way to handle the interfacing between the finite-difference technique and the analytical method by dividing the finite difference region into two regions. The situation is slightly different here. The left boundary requires special treatment as well.

The staggered-grid scheme is used for finite-differencing the P-SV wave equations [*Virieux*, 1986; *Levander*, 1988]. Finite-difference grids are illustrated in Figure 5.1b, where vertical and horizontal velocities are indicated by triangles and circles, and normal and shear stresses are represented by diamonds and squares. The finite difference grids are divided into three regions, separated by the dashed lines in Figure 5.1b:

1. Total: where the whole wavefields are calculated. The heterogeneity is only present in this region.

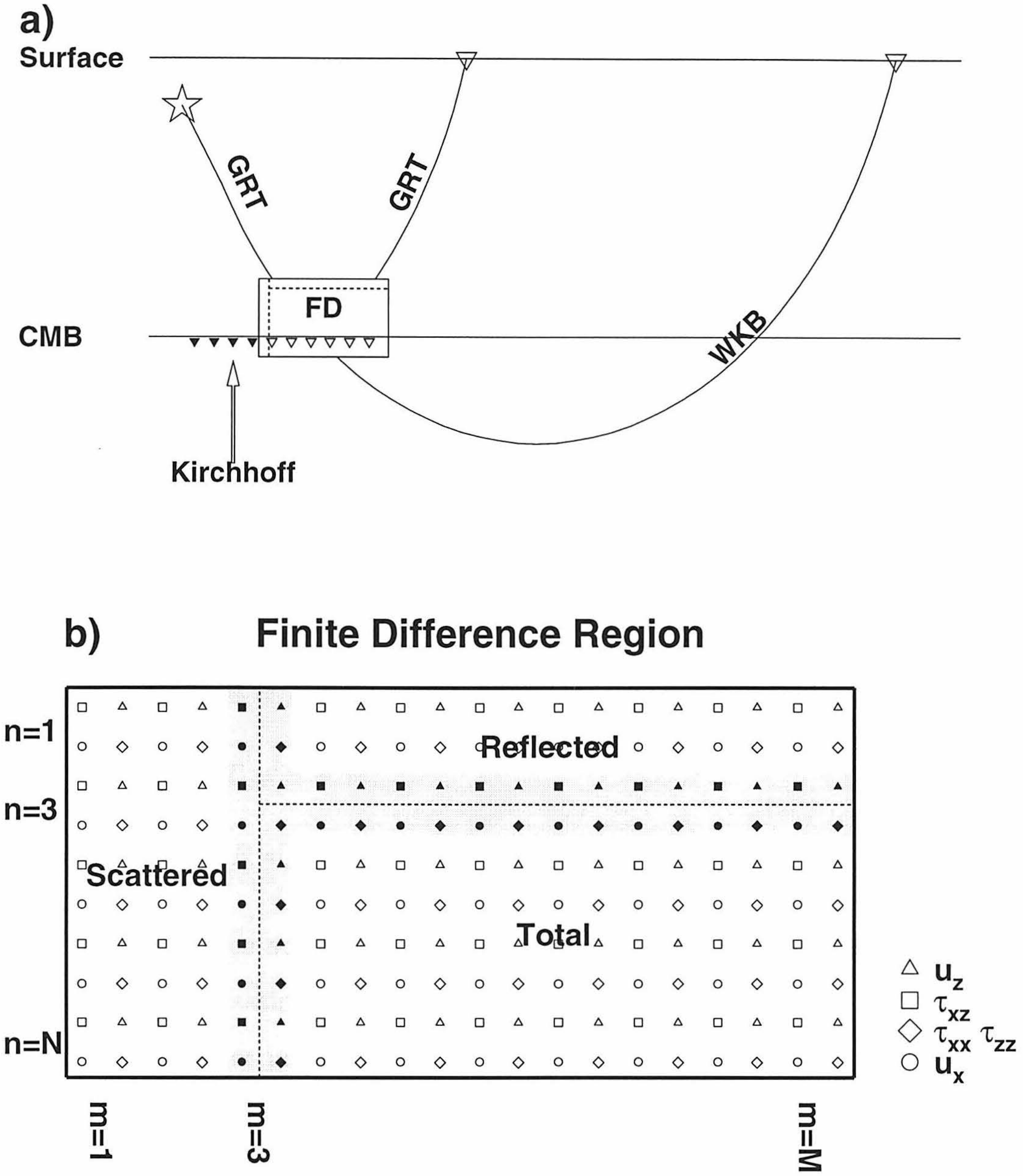

Figure 5.1: a) Schematic illustration of interfacings of the hybrid method. The heterogeneous regions are assumed to be confined inside the small box, where the finite-difference technique is applied. Generalized ray theory is used to calculate wave propagation from the source to the finite-difference region and synthetic seismograms at the Earth's surface is obtained by integrating convolutions of the output from the source-side along the line represented by triangles and the Green's function from the receiver-side at the same positions. The source-side output in positions represented by filled triangles is calculated by the generalized ray theory; that in positions represented by empty triangles is obtained from the finite-difference calculation. b). The division of the finite-difference region. The finite-difference region is divided into three parts, where different wave fields are calculated (see text for detailed explanations).

2. Reflected: where reflected wavefields are calculated. The reflected waves are defined as the reflections from the heterogeneous region (i.e., energy propagating upward), due to the incident wave.

3. Scattered: where scattered wavefields are calculated. Scattered wavefields are defined as the scattering due to the presence of the heterogeneities (i.e., energy propagating leftward). For an one-dimensional model, these wavefields are zero.

Let the incident wavefield be I_0, the one-dimensional solution of the wavefield be T_0, the reflected wavefield due to the one-dimensional model be R_0, the whole wavefield be T, the reflected wavefield be R and the scattered wavefield be S. I, T, R and S are either velocities (u_x, u_z) or stresses (τ_{xx}, τ_{zz}, τ_{xz}). There are general relationships among S, I, T and R, namely

1. $T = I_0 + R$; or $R = T - I_0$;

2. $S = T - T_0$; or $T = S + T_0$;

3. $S = R - R_0$; or $R = S + R_0$.

The finite-difference schemes are applied directly in those regions, since wavefields in those regions satisfy the wave equations individually. The explicit numerical schemes of fourth order in space and second order in time [*Levander*, 1988] are applied in the interior of those regions, whereas those of second order in space and time [*Virieux*, 1986] are used for the grid points indicated by filled symbols in Figure 5.1b, where special treatments are required. For example, in order to calculate the reflected shear stresses (τ_{xz}) at n = 3 (filled squares), the reflected horizontal velocities (u_x) at n=3 (filled circles) are required. The horizontal velocities (u_x) in those positions, however, are the whole wavefields as defined above. On the other hand, in order to calculate the whole horizontal velocities (u_x) at n=3 (filled circles), the whole shear stresses (τ_{xz}) at n=3 (filled squares) are required. The shear stresses τ_{xz} at those positions, however, are the reflected wavefields as defined above. The whole shear stress (τ_{xz}) and reflected horizontal velocities (u_x) can be obtained by using the above three relationships among I, R, S and T. The explicit finite difference formulations at those special regions are presented in the appendix.

5.3.2 Generalized ray theory

I_0, R_0 and T_0 can be calculated by the generalized ray theory [*Helmberger*, 1983]. With small modifications for a line source, the potentials for a receiver in a medium with a stratified velocity structure are:

P-waves:

$$\varphi = \frac{M_0}{4\pi\rho}[\dot{D}(t) * \sum_{j=1}^{3} A_j C_j V_\alpha(t)] \tag{5.1}$$

SV-waves:

$$\Omega = \frac{M_0}{4\pi\rho}[\dot{D}(t) * \sum_{j=1}^{3} A_j SV_j V_\beta(t)] \tag{5.2}$$

where

$$V_\alpha(t) = \frac{1}{\pi}[\sum_{i=1}^{n} Im(\frac{1}{\eta_\alpha} \prod(p) \frac{dp}{dt})_i],$$

$$V_\beta(t) = \frac{1}{\pi}[\sum_{i=1}^{n} Im(\frac{1}{\eta_\beta} \prod(p) \frac{dp}{dt})_i],$$

p = ray parameter,

$\dot{D}(t)$ = far-field time function,

$\prod(p)$ = product of the transmission and reflection coefficients,

$\sum$ = summation over contributing rays,

$\eta_\beta = (\beta^{-2} - p^2)^{\frac{1}{2}}$, $\eta_\alpha = (\alpha^{-2} - p^2)^{\frac{1}{2}}$.

The orientation constants A_j and source radiation patterns C_j, SV_j, are defined in *Helmberger* [1983]. From the relationships between stresses and displacements:

$$\begin{aligned}
\tau_{xx} &= (\lambda+2\mu)\frac{\partial u}{\partial x} + \lambda(\frac{\partial w}{\partial z}), \\
\tau_{zz} &= \lambda\frac{\partial u}{\partial x} + (\lambda+2\mu)(\frac{\partial w}{\partial z}), \\
\tau_{xz} &= \mu(\frac{\partial u}{\partial x} + \frac{\partial w}{\partial z}).
\end{aligned}$$

where u and w are the x- and z- components of displacement, receiver functions for converting potentials to velocities and stresses are:

for velocities:

$$\left\{\begin{aligned}
R_{pz} &= s^2\varepsilon\eta_\alpha \\
R_{px} &= s^2 p
\end{aligned}\right.$$

$$\left\{\begin{aligned}
R_{sz} &= s^2 p \\
R_{sx} &= s^2\varepsilon\eta_\beta
\end{aligned}\right.$$

for stresses:

$$\left\{\begin{aligned}
R_{p\tau_{xx}} &= s^2((\lambda+2\mu)p^2 + \lambda\eta_\alpha^2) \\
R_{p\tau_{zz}} &= s^2(\lambda p^2 + (\lambda+2\mu)\eta_\alpha^2) \\
R_{p\tau_{xz}} &= s^2(-2\varepsilon\mu p\eta_\alpha)
\end{aligned}\right.$$

$$\left\{\begin{aligned}
R_{s\tau_{xx}} &= s^2(-2\varepsilon\mu p\eta_\beta) \\
R_{s\tau_{zz}} &= s^2(2\varepsilon\mu p\eta_\beta) \\
R_{s\tau_{xz}} &= s^2\mu(\eta_\beta^2 - p^2)
\end{aligned}\right.$$

$$\varepsilon = \begin{cases} 1 & \text{upgoing ray} \\ -1 & \text{downgoing ray} \end{cases}$$

Horizontal velocities calculated by the GRT-FD interfacing and those from GRT for an incident SV wave on the one-dimensional PREM reference model [*Dziewonski and Anderson*, 1981] show an excellent agreement in terms of both waveshape and absolute amplitude (Figure 5.2). The left panel shows a comparison of synthetics for receivers indicated by squares and the right panel for receivers indicated by triangles. All traces are plotted to the same scale. Two primary phases are produced by the interaction of the incident SV wave with the core-mantle boundary, namely an S to P reflection and an S to S reflection. The P-wave from the former reflection becomes a head-wave and diffracts into the core. Note that the diffracted P phase is small for PREM.

5.3.3 Kirchhoff interfacing

For any two functions: u and w, there exists a relationship:

$$\int_{\Gamma}(u\frac{\partial w}{\partial n} - w\frac{\partial u}{\partial n})dl = \int\int_{D}(u \bigtriangledown^2 w - w \bigtriangledown^2 u)dA \tag{5.3}$$

D is enclosed by Γ, n is outward directed normal to Γ, dl is the line integral along Γ and dA is the areal integral in D.

The wavefield potential (Q), for a seismic wave propagating in a two-dimensional whole space, satisfies the following equation:

$$\bigtriangledown^2 Q = \frac{1}{v^2}\frac{\partial^2 Q}{\partial t^2}$$

where v is either P or SV wave propagational velocity. The Laplace transform of the above equation over time yields:

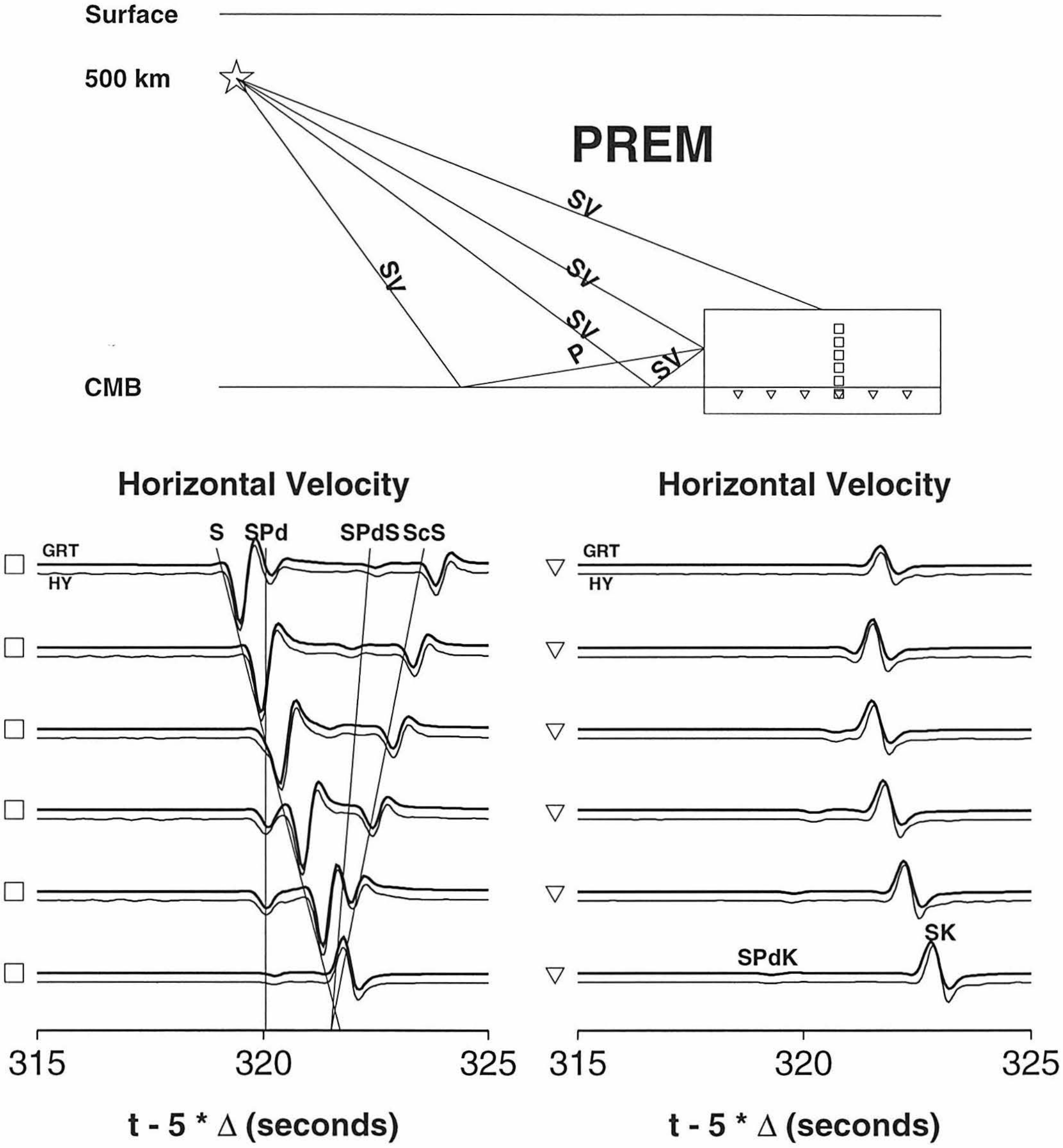

Figure 5.2: Comparison of horizontal velocities obtained by the generalized ray theory (heavy lines) and the hybrid method (light lines) with a source depth of 500 km. The epicentral distance of the vertical cross section is 1000 km and the separation of vertical receivers is 8 km. The separation of horizontal receivers is 55 km. PREM is used for the calculation and the Earth flattening approximation is applied. All seismograms are plotted to the same scale.

$$(\nabla^2 - \frac{s^2}{v^2})\bar{Q} = 0$$

The Green's function ($\bar{G}$) for a line source, by definition, satisfies:

$$(\nabla^2 - \frac{s^2}{v^2})\bar{G} = \delta(x - x')\delta(z - z') \tag{5.4}$$

Inserting $\bar{G}$ and $\bar{Q}$ into equation 5.3, we have

$$\begin{aligned}\int_\Gamma (\bar{Q}\frac{\partial \bar{G}}{\partial n} - \bar{G}\frac{\partial \bar{Q}}{\partial n})dl &= \int\int_D (\bar{Q} \nabla^2 \bar{G} - \bar{G} \nabla^2 \bar{Q})dA \\ &= \int\int_D \bar{Q}\delta(x - x')\delta(z - z')dA\end{aligned}$$

that is,

$$\bar{Q}(x, z) = \int_\Gamma (\bar{Q}\frac{\partial \bar{G}}{\partial n} - \bar{G}\frac{\partial \bar{Q}}{\partial n})dl \tag{5.5}$$

In this study, the integration is along a straight line just below the core-mantle boundary, G is calculated by WKB technique [*Chapman*, 1976] and Q is output from the GRT-FD interfacing for regions indicated by solid triangles and directly from the generalized ray theory, for regions indicated by empty triangles in Figure 5.1.

Since Q only applies to a P or an SV wave, it is necessary to separate the responses of P and SV waves from the output of the finite-difference calculation. P and SV responses can be separated based on displacements and stresses output from the finite-difference calculation:

$$\vec{u} = \nabla\phi + \nabla \times \psi\vec{e}_z = \vec{u}_p + \vec{u}_s$$

where $\vec{u}$ is displacement and ϕ and ψ are the potentials for P and SV waves respectively. Note that

$$\begin{aligned}
\bigtriangledown(\bigtriangledown \cdot \vec{u}) &= \bigtriangledown(\bigtriangledown^2 \phi) \\
&= \frac{1}{\alpha^2}\frac{\partial^2 \bigtriangledown \phi}{\partial t^2} \\
&= \frac{1}{\alpha^2}\frac{\partial^2 \vec{u}_p}{\partial t^2} && (5.6) \\
\bigtriangledown \times (\bigtriangledown \times \vec{u}) &= \bigtriangledown \times (\bigtriangledown \times \bigtriangledown \times \psi \vec{e}_z) \\
&= \bigtriangledown \times (\bigtriangledown(\bigtriangledown \cdot \psi \vec{e}_z) - \bigtriangledown^2 \psi \vec{e}_z) \\
&= -\bigtriangledown \times (\frac{1}{\beta^2}\frac{\partial^2 \psi}{\partial t^2}\vec{e}_z) \\
&= -\frac{1}{\beta^2}\frac{\partial^2(\bigtriangledown \times \psi \vec{e}_z)}{\partial t^2} \\
&= -\frac{1}{\beta^2}\frac{\partial^2 \vec{u}_s}{\partial t^2} && (5.7)
\end{aligned}$$

Thus, Q in equation (5.5) can take the forms of $\bigtriangledown(\bigtriangledown \cdot \vec{u})$ and $\bigtriangledown \times (\bigtriangledown \times \vec{u})$, which are equivalent to accelerations caused by P and SV waves respectively. $\bigtriangledown(\bigtriangledown \cdot \vec{u})$ and $\bigtriangledown \times (\bigtriangledown \times \vec{u})$ can be obtained from the displacements and stresses output from the finite-difference calculation.

$$\begin{aligned}
\bigtriangledown(\bigtriangledown \cdot \vec{u}) &= \bigtriangledown(\tfrac{\partial u_x}{\partial x} + \tfrac{\partial u_z}{\partial z}) \\
&= \bigtriangledown(\tfrac{\tau_{xx}+\tau_{zz}}{2(\lambda+\mu)}) \\
&= \tfrac{\partial}{\partial x}(\tfrac{\tau_{xx}+\tau_{zz}}{2(\lambda+\mu)})\vec{e}_x + \tfrac{\partial}{\partial z}(\tfrac{\tau_{xx}+\tau_{zz}}{2(\lambda+\mu)})\vec{e}_z \\
\bigtriangledown \times (\bigtriangledown \times \vec{u}) &= \tfrac{\partial}{\partial z}(\tfrac{\partial u_z}{\partial x} - \tfrac{\partial u_x}{\partial z})\vec{e}_x + \tfrac{\partial}{\partial x}(\tfrac{\partial u_x}{\partial z} - \tfrac{\partial u_z}{\partial x})\vec{e}_z
\end{aligned}$$

$\bigtriangledown(\bigtriangledown \cdot \vec{u})$ and its $z-$ derivative calculated by GRT and those obtained by the FD-GRT interfacing show an excellent agreement (Figure 5.3). Again, all traces are plotted to the same scale and PREM is assumed.

The point source solution can be obtained by correcting the line source response [e.g., *Stead and Helmberger*, 1988]:

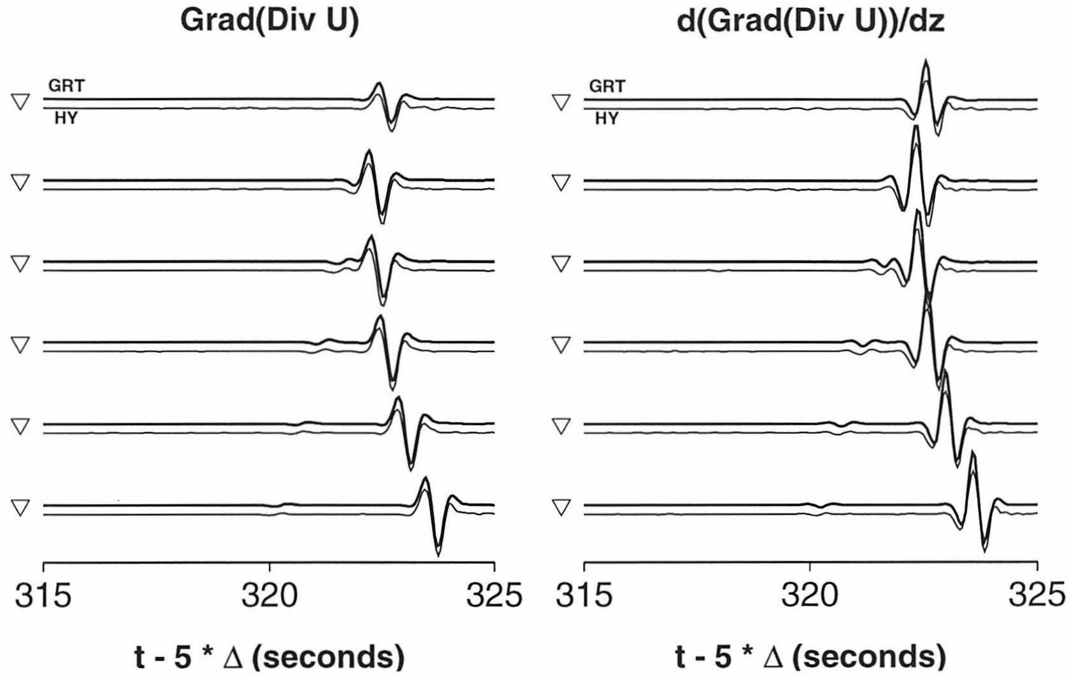

Figure 5.3: Comparison of quantities $\nabla(\nabla \cdot U)_x$ and $\frac{d}{dz}(\nabla(\nabla \cdot U)_x)$ obtained by the generalized ray theory (light traces) and the hybrid method (heavy traces). All synthetics are plotted to the same scale. The receivers are indicated in Figure 5.2.

$$U_{point} = \frac{2}{\sqrt{R} + \sqrt{x}} \frac{1}{\sqrt{t}} * \frac{d}{dt} U_{line} \tag{5.8}$$

where R and x are the total and horizontal distances respectively.

For Earth models similar to PREM, SV wave reaches a critical angle at the core-mantle boundary and bifurcates into an SKS and a diffracted P (SPdKS) propagating along the boundary at a distance of about 106^0 [*Choy*, 1977](Figure 5.4). Synthetics waveforms obtained from the GRT-FD-Kirchhoff interfacing and those by the generalized ray theory show reasonable agreement except the difference in the frequency content of the SPdKS phase at large distances (Figure 5.4). The discrepancy is caused by the lack of long period diffracted energy obtained from the WKB synthetics [*Chapman and Orcutt*, 1985; *Helmberger et al.*, 1996]. The difference becomes less noticeable when SPdKS contributions dominate the synthetics for models with ultra low velocity zones (ULVZ).

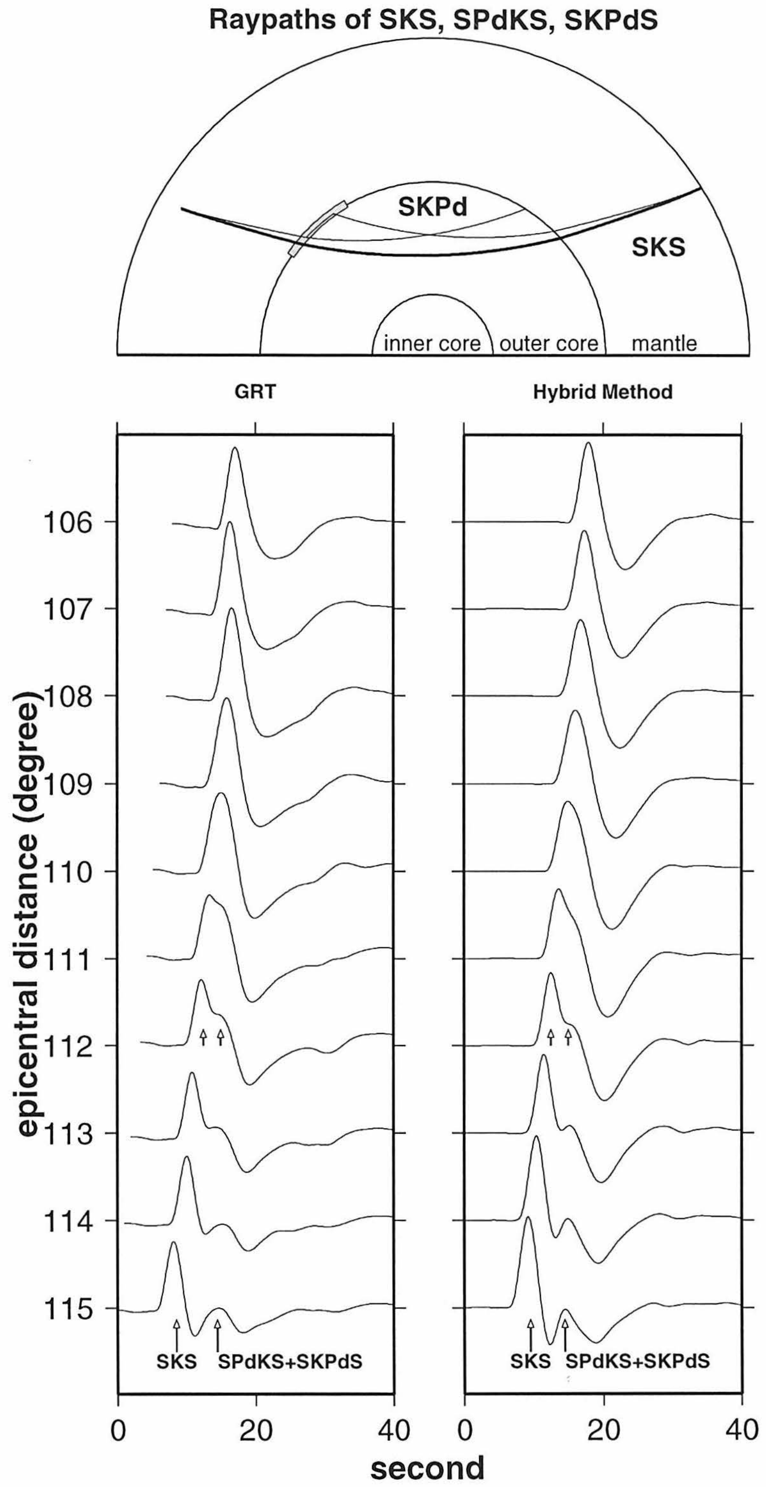

Figure 5.4: Ray paths of SKS-SPdKS phases and comparison of SKS-SPdKS synthetics obtained by the generalized ray theory and the hybrid method. Synthetics have been convolved with the long period instrument response of the world-wide standard seismic network (WWSSN) with $t^* = 1$ and a trapezoidal source time function (1,1,1). All traces are self normalized. PREM and a source depth of 500 km are used for the calculation. The shaded area is the finite difference region.

5.4 Conclusion

A two-dimensional P-SV hybrid method is developed, which combines generalized ray theory, finite-difference, WKB and the Kirchhoff theory. The generalized ray theory solutions are interfaced with the finite-difference calculation and synthetics at the surface of the Earth are obtained by integrating convolutions of the output from a finite-difference technique with WKB Green's functions by applying the Kirchhoff theory. Since the finite-difference technique is applied in the heterogeneous region only, the hybrid method takes much less computer memory and has wide applications for high-resolution studies of localized structures. The comparisons of the hybrid method seismograms with the generalized ray theory seismograms yield good agreement.

Chapter 6 Ultra-low velocity zones from SKS and SPdKS/SPKdS phases

6.1 Abstract

Anomalous long-period SKS-SPdKS observations, sampling a region near the core-mantle boundary beneath the south-west Pacific and Iceland, are modeled with the hybrid method. Localized structures just above the core-mantle boundary, with lateral dimensions of 250 to 400 km, can explain even the most anomalous data observed to date if S-velocity drops up to 30% are allowed for a P-velocity drop of 10%. Structural shapes and seismic properties of those anomalies are constrained from the data since synthetic waveforms are sensitive to the location and lateral dimension of seismic anomalies near the core-mantle boundary. Some important issues, such as the density change and roughness of the structures and the sharpness of the transition from the structures to the surrounding mantle, however, remain unresolved due to the nature of the data.

6.2 Introduction

SKS-SPdKS waveforms are very sensitive to the localized structures near the core-mantle boundary and provide ideal localized samplings of these structures. In the meantime, the almost identical ray paths of SKS and SPdKS in the mantle (Figure 5.4) and the nearly homogeneous outer core structure minimize the uncertainties of waveform modeling due to crust and mantle heterogeneities and seismic source radiation pattern.

Figure 6.1 displays a sample of anomalous SKS-SPdKS waveforms, recorded at long period WWSSN stations in North America, for two Fiji and one Kermadec events. The large relative time lags of SPdKS phases with respect to SKS and the small critical distance for SKS are obvious in the data, as opposed to the predictions (dashed lines) from PREM (Figure 6.1). The arrival times in the average data can be fit by a model with a 10% drop of P-velocity at the mantle's base (dotted line) [*Garnero and Helmberger*, 1996]. Contrary to those predicted by PREM, the diffracted SPdKS phases at some distances (e.g., 110^0) become strong geometrical arrivals if a low velocity layer is present just above the core-mantle boundary [*Helmberger et al.*, 1996]. The considerable variation of observed waveforms has been modeled in terms of ultra low velocity layers at the bottom of mantle with variable layer thicknesses ranging from 5 to 40 km, drops in P and S velocities of 10%, and the density of PREM [*Garnero and Helmberger*, 1996]. If the low velocity layer, however, is caused by partial melting, an S velocity drop of about 30% will be expected for a P velocity drop of 10% [*Williams and Garnero*, 1996]. In that case, the converted S to P phase at the upper boundary of ultra low velocity layers becomes discernible in synthetics, unlike the data. Unless the thickness of the layer is less than about 10 km, the separation in timing between the SKS and the converted phases is small and not observable at long-period waveforms [*Garnero and Helmberger*, 1997]. Models with flat layers encounter a further conceptual problem when the waveform variation continues down to small scales, as documented by *Garnero and Helmberger* [1997]. Essentially, to match the waveforms requires that the variation in layer thickness approaches the lateral sampling separation, in violation of Huygen's principle. Moreover, some very anomalous records, such as those labeled by the dots in Figure 6.1, remain unexplained with current modeling techniques. Given these modeling difficulties and large velocity variations, it appears particularly important and necessary to investigate the effects of non-planar structures by numerical methods, as strongly suggested by the rapid variations of the observed waveforms. In this chapter, we perform SKS-SPdKS waveform sensitivity studies for various two-dimensional structures in the first part and model the Fiji and Iceland data in the second part.

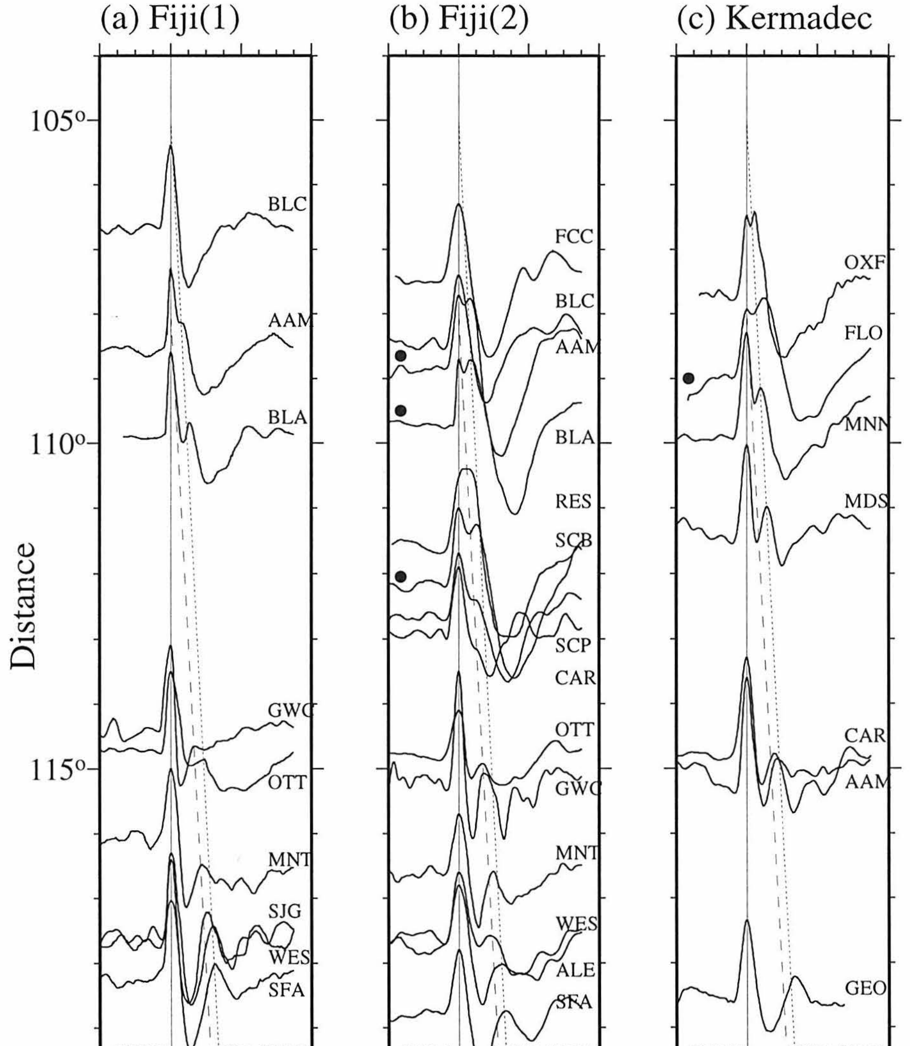

Figure 6.1: Observed SKS-SPdKS seismograms for 2 Fiji and 1 Kermadec events and predicted arrivals of SKS and SPdKS phases for PREM (dashed lines) and a model with a P velocity drop of 10% at the mantle's base (solid lines).

6.3 Sensitivity studies

In this section, we explore the waveform complexity produced by various two-dimensional structures. To reduce the parameter space, we consider mostly simple dome-shaped structures just above the core-mantle boundary. These structures produce waveforms best fit to the data. In most cases, we adopt an 1 to 3 ratio of P and S velocity drops of the seismic anomalies, which is favored on the physical ground of partial melt [*Williams and Garnero*, 1996], although other values of this ratio are also considered. We examine effects of various dimensions (in height and width), seismic parameters and position.

We begin by exploring effects of dome curvature for an impinging SV wave. The dome is assumed to have a P-velocity reduction of 10%, an S-velocity reduction of 30% and a density increase of 20%, with respect to PREM. These parameters are obtained by assuming a partial melting origin [*Williams and Garnero*, 1996]. PREM is used elsewhere. The dome starts just before the SV wave reaches the critical angle at about 770 km and ends at 1043 km (Figure 6.2a). Figure 6.2b shows the important phases for generating the SPdKS-SKPdS phase at the surface of the Earth. SKPdS is formed as an SSK wave on the source side and a KPdS wave on the receiver side of the mantle and SPdKS is formed as an SPdK and an SPK on the source side and a KS on the receiver side of the mantle. Snapshots of wave propagation are shown in Figures 6.2c-f. At t = 384.25 *sec*, only the incident SV wave is present (Figure 6.2c). The converted and reflected phases due to the dome structure at later times are labeled in the figure (Figures 6.2d-f). SPdK is relatively small because it is a diffracted arrival while the SPK phase is strong because it is locally a geometrical arrival (e.g., Figure 6.2e).

The propagational effects of ultra low velocity zones are demonstrated by the SKS-SPdKS total waveforms and contributions from different segments of the core-mantle boundary, separated by the Kirchhoff integral on the source side (Figure 6.3). The division of segments is shown in the top panel. The PREM synthetics are also shown in dashed lines for comparison. Contributions from the segment 1 are exactly

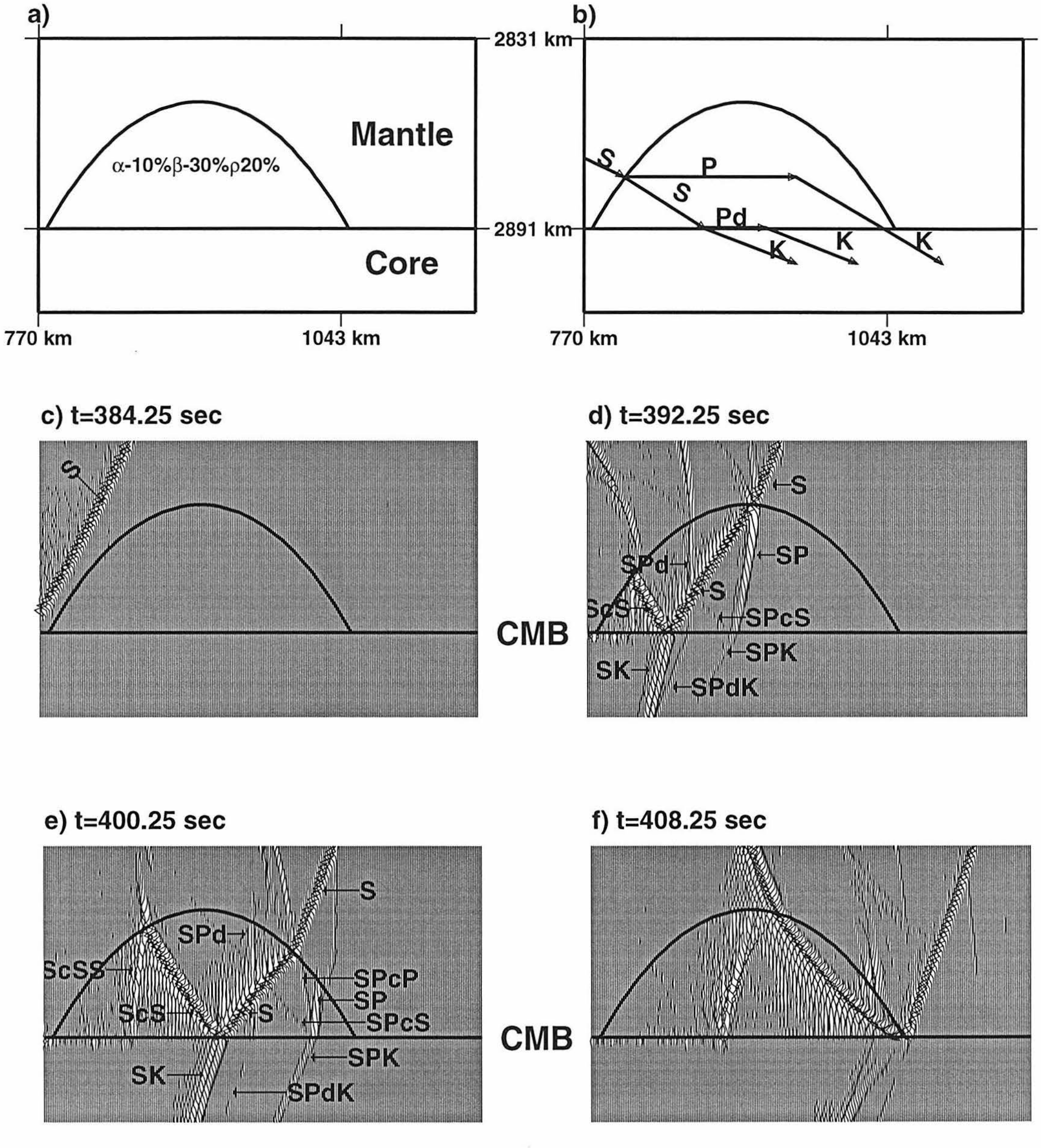

c) t=384.25 sec

d) t=392.25 sec

e) t=400.25 sec

f) t=408.25 sec

Figure 6.2: Wave propagation for a model with a dome-like structure just above the core-mantle boundary. PREM is used and the dome has a P velocity reduction of 10%, an S velocity reduction of 30% and a density increase of 20% with respect to PREM. These parameters are obtained by assuming partial melt with a P velocity drop of 10%. a) model setup; b) important phases for generating SKS-SPdKS waves at the surface of the Earth; c-f), snapshots of the wavefields.

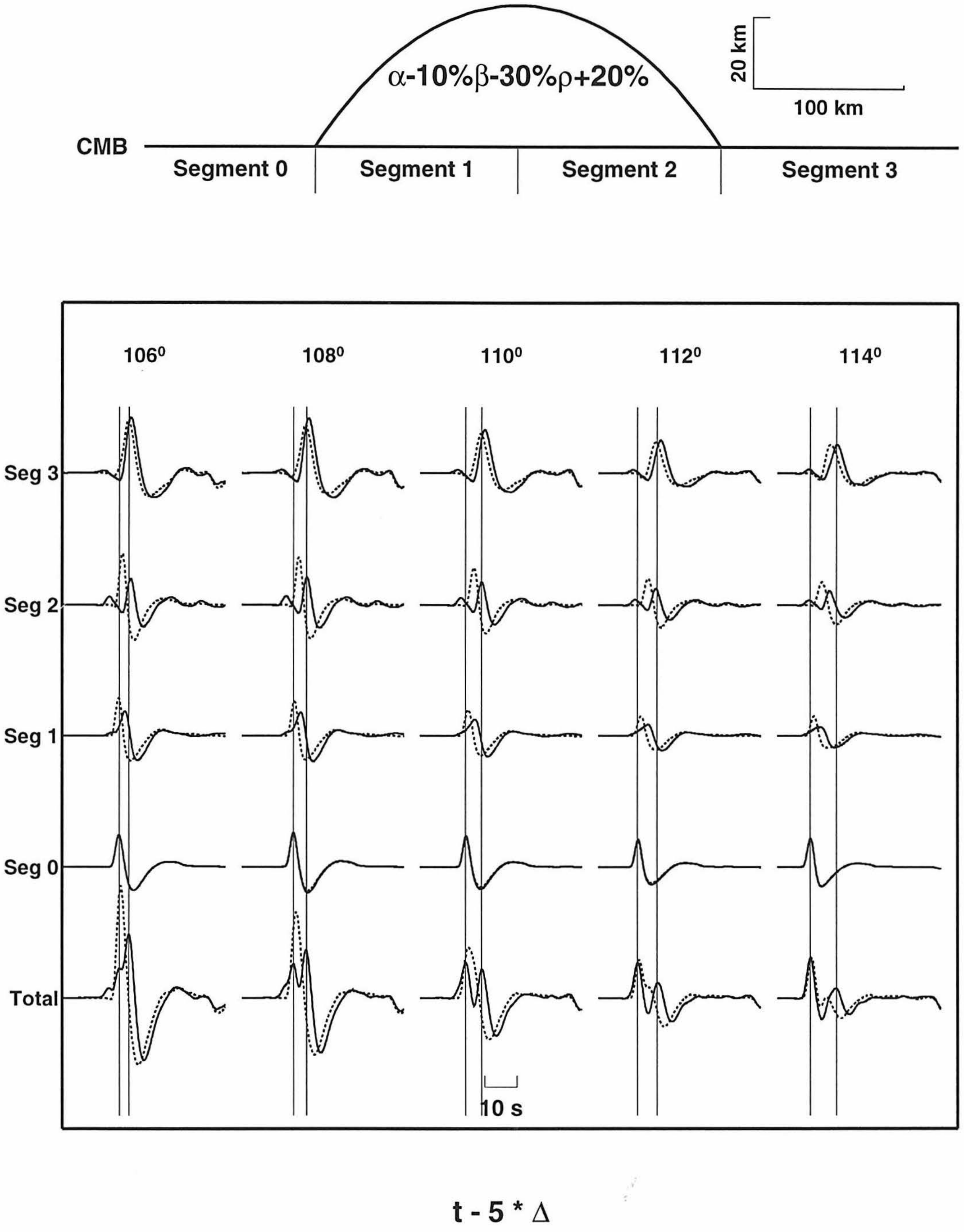

Figure 6.3: The total SKS-SPdKS waveform synthetics along with contributions to SKS-SPdKS synthetics from different segments of the core-mantle boundary on the source side. The dashed traces are those for PREM and heavy traces are calculated with the dome structure shown in Figure 6.2. The source depth is 500 km.

matched for both models, since the wave propagation is not affected by the presence of the ultra low velocity zone. For the contributions from the segment 3, waveforms predicted by the dome structure are in good agreement with those of PREM, except that they are delayed by the ultra low velocity zone. For the SKS-SPdKS wave groups contributed by the segments 2 and 1, in addition to the delays of waveforms caused by the ultra low velocity zone, the reduced amplitudes of these SKS-SPdKS phases produced by the model with the ultra low velocity zone are also obvious. The delays break down the coherence of SKS at small distances (106^0-110^0) and partition the SKS energy into two phases. Note that the maximal amplitudes of synthetics predicted by the dome structure are smaller than those of PREM at these distances, because some energy of the incident SV wave is reflected back into the mantle due to the curved structure and some SKS energy is partitioned into SPdKS and SPKS phases. The latter phase has a path similar to SKS except that it propagates as a converted P wave in the ultra low velocity zone. SPKS appears as a precursor in the contributions from the segment 2. Those precursors will become more obvious if the dome-structure is under the entry point of SKS phase. At larger distances, the dome structure affects mostly the SPdKS phases, since the dome structure is far away from the entry point of SKS at these distances. It is also obvious from snapshots that the dome structure will produce strong precursors to ScP and ScS.

Figure 6.4 shows snapshots of wave propagation for a boxcar structure for the same model setup in Figure 6.2. Although broadband SKS-SPdKS synthetics for the model with a dome-shaped structure and that with a boxcar structure are distinguishable, the long period WWSSN synthetics, however, are very similar for these two structures with these dimensions (Figure 6.5). For the boxcar structure, precursors to SKS are stronger because of a stronger S to P conversion from the mantle to the structure, compared to the case of the dome-like structure (Figure 6.2). If the boxcar structure extends to larger distances, synthetics will become even more complex, with many converted phases even for long period synthetics, similar to the predictions from one-dimensional models with ultra low velocity layers.

Since the multiples are strongly influenced by the geometrical location of the S to P

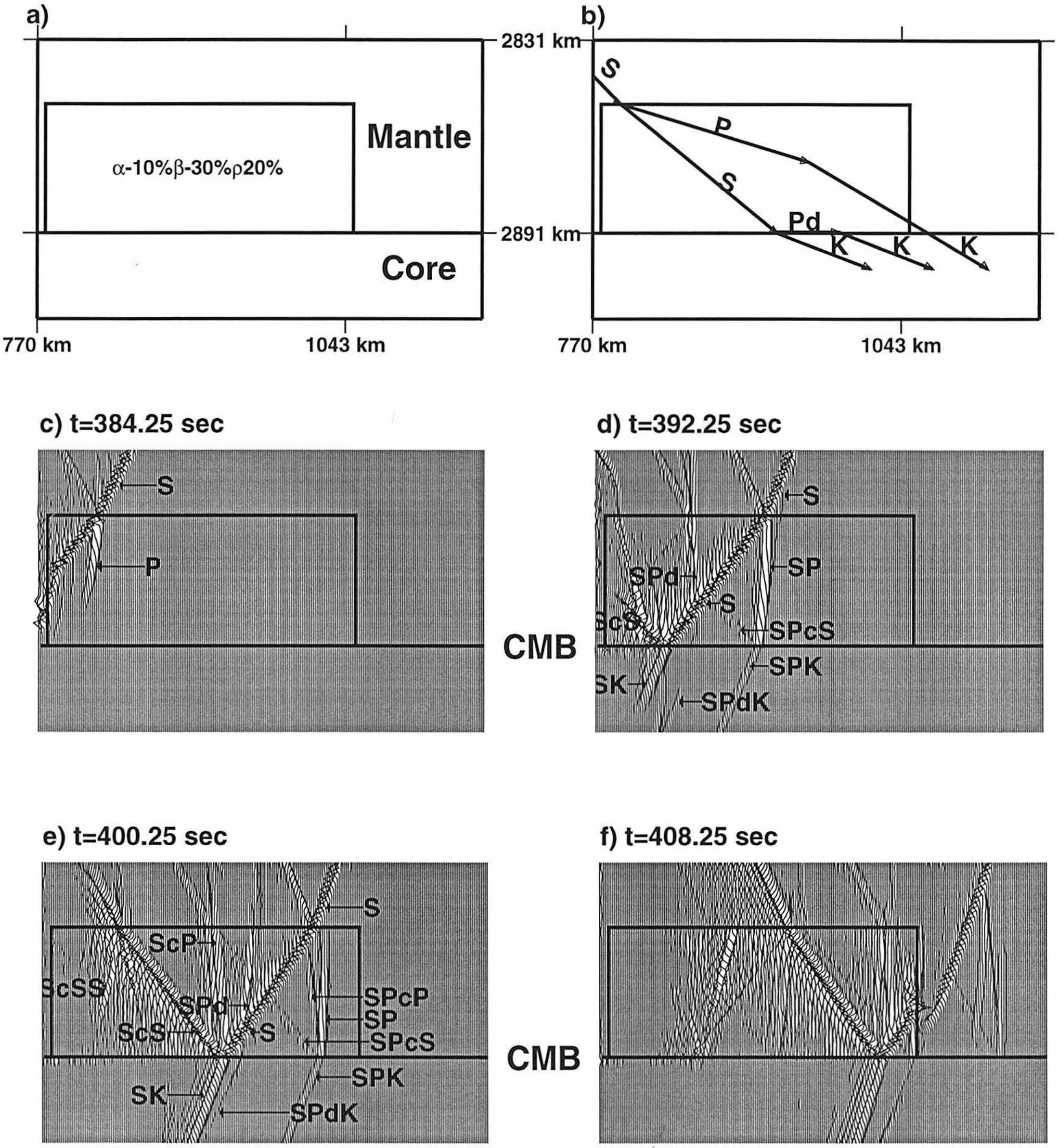

Figure 6.4: Same as Figure 6.2, except that the low velocity region is a boxcar.

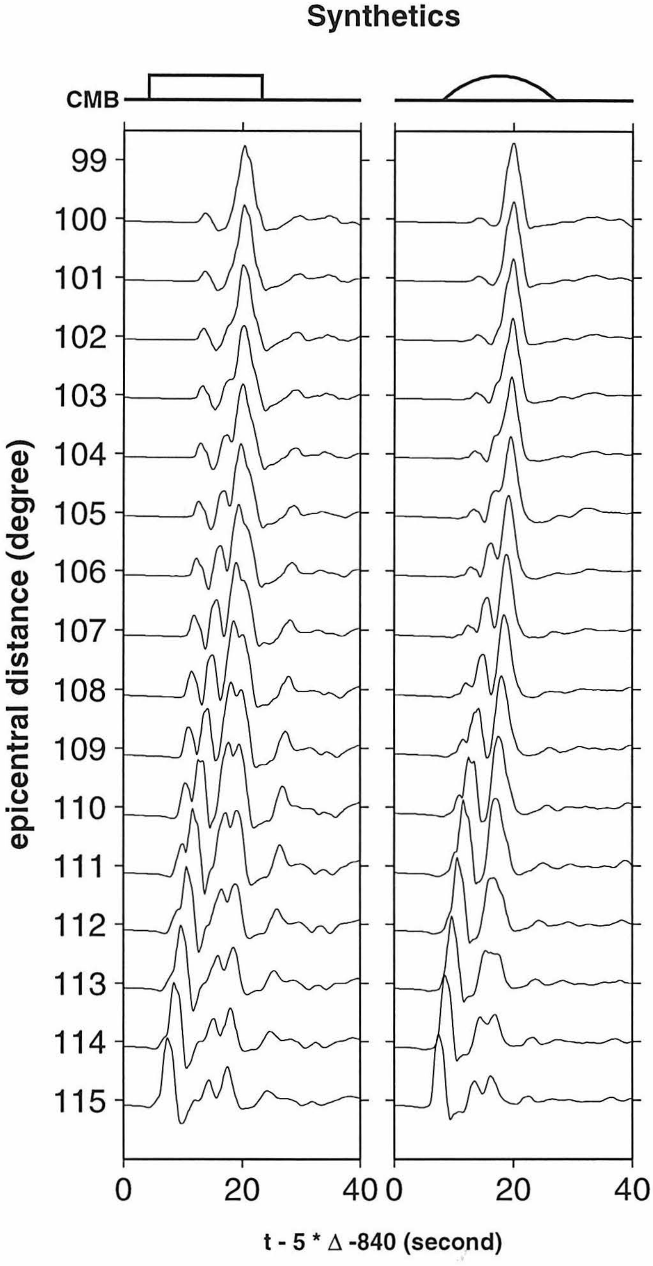

Figure 6.5: The broadband synthetic SKS-SPdKS waveforms for models shown in Figures 6.2 and 6.4. The synthetics are obtained by convolving the Green's functions with a source time trapezoidal function (1,1,1) and $t^* = 1$.

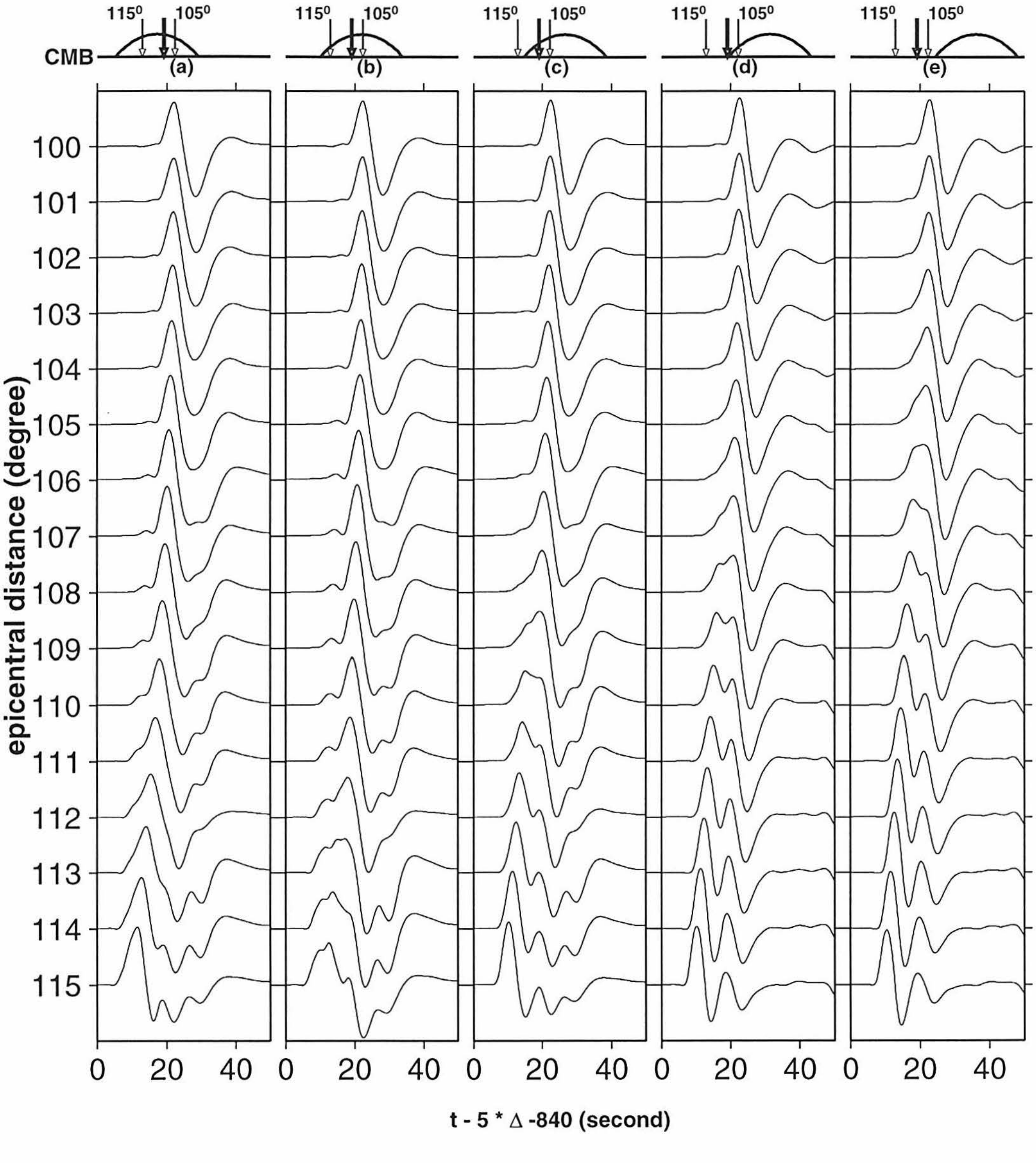

Figure 6.6: Synthetic SKS-SPdKS waveforms for models with dome-like structures just above the core-mantle boundary on the source side. Domes have a horizontal scale of 267 km, a thickness of 40 km, a P velocity reduction of 10%, an S velocity reduction of 30% and a density increase of 20% with respect to PREM. Different panels of synthetics correspond to different positions of the dome-like structures. The entry points of SKS phase for distance ranges at 105^0 and 115^0 are shown in the figure and the critical distance for SKS at the core-mantle boundary are indicated by heavy arrows. All synthetics have been convolved with the long period WWSSN instrument response with $t^* = 1$ and with a source time trapezoidal function (2,2,2). The source depth is 500 km and PREM is assumed elsewhere.

critical angle, the location of two-dimensional structures becomes a controlling factor in modeling SKS-SPdKS waveforms, as demonstrated in the synthetic record sections for dome-like structures located in various positions above the core-mantle boundary (Figure 6.6). The synthetics are convolved with a trapezoidal (1,1,1) source time function and the long period WWSSN instrument response. The SV critical points (heavy arrows) and the SKS entry points for epicentral distances 105^0 and 115^0 at the core-mantle boundary are shown in the figure. In panel (a), the dome-structure is in the position that affects SKS phase very little, for epicentral distances less than 105^0; small precursors are present for the distance ranges 103^0-109^0 and the dome-structure distorts SKS severely for distance ranges 111^0-115^0. Synthetics in panel (b) show the same characteristics as those in panel (a), except that the separation between SKS and SPKS becomes more obvious at distance ranges 111^0-115^0. Note the complex waveforms at those distances in panel (b). In panel (c), the dome-structure has little effect on the SKS phase at distances greater than 114^0, since anomalies are no longer beneath the entry points of SKS at those distances. The dome-structure becomes important in affecting the timing and waveshape of SKS-SPdKS phases, as is obvious in the synthetics at distance ranges 108^0-113^0. The second phase appears even stronger than the first one at some distances (e.g., 109^0). Waveform distortions appear at smaller distances in the synthetics shown in panels (d)-(e).

Long period SKS-SPdKS synthetics are also sensitive to the dimensions (height and width) and seismic parameters of the dome-shaped structures, although some trade-offs exist among these parameters (Figure 6.7). The synthetics in panel (a) are calculated with a 40 km high and 136 km wide dome-shaped structure, located 136 km beyond the SV critical point. Synthetics produced with this dome-shaped structure, though different from those produced by PREM, are near the threshold of detectability of difference. Synthetics in panels (b)-(c) are obtained for models of 40 km high domes with horizontal length scales of 267 and 534 km. The domes are now located just after the critical distance for SV waves. Note the significant difference between synthetics in these two panels. The SPdKS phases are very small for the model with a 534 km dome because the dome structure attenuates SPdKS-

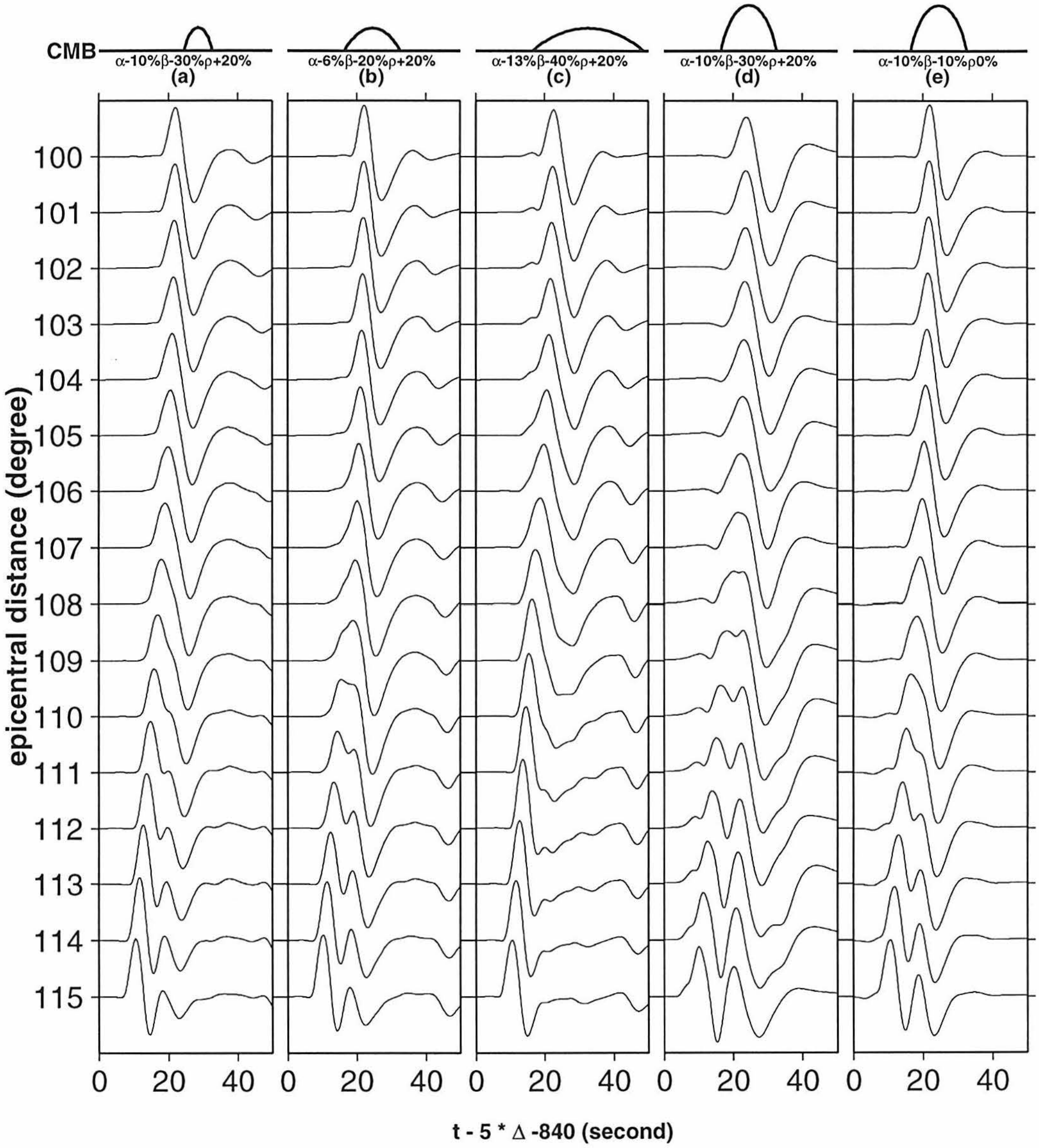

Figure 6.7: Synthetic SKS-SPdKS waveforms for models with different dome structures just above the core-mantle boundary. All synthetics have been convolved with the long period WWSSN instrument response with $t^* = 1$ and with a source time trapezoidal function (2,2,2). The source depth is 500 km and PREM is assumed elsewhere. The horizontal length scales for models from panel (b)-(e) are 267 km, whereas that for model panel (a) is 133.5 km. The heights of the dome are 40 km in panel (a)-(c) and 80 km in panel (d)-(e).

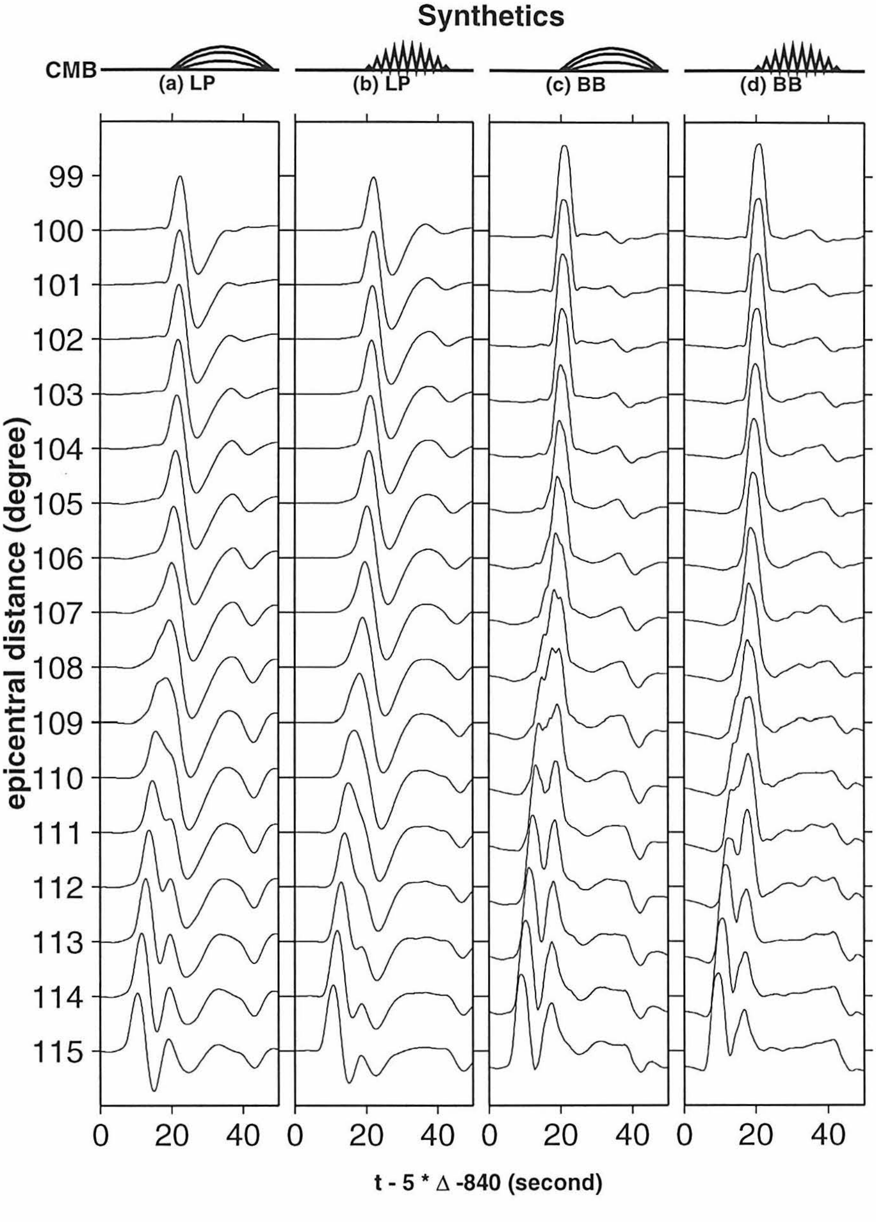

Figure 6.8: Long period (LP) and broadband (BB) synthetics for models with different dome structures just above the core-mantle boundary. Synthetics in (c) and (d) have been convolved with $t^* = 1$ and with a source time trapezoidal function (2,2,2). Synthetics in (a) and (b) have also been convolved with the long period WWSSN instrument response. The source depth is 500 km and PREM is assumed elsewhere. The model used in (a) and (c) consists of three layers with P velocity reductions of 3%, 6% 10%, SV velocity reductions of 10%, 20%, 30%, and density increases of 7%, 14%, 20% from outer to the inner layers. The models used in (b) and (d) have roughness and a P velocity reduction of 10%, an SV velocity reduction of 30% and a density increase of 20%. All structures have horizontal length scales of 250 km. Note that SKS-SPdKS synthetics are not sensitive to the smoothness of the transition to the localized structures and the roughness of those seismic structures.

SKS phases over a longer distance. The second phase and the SPdKS phase become very weak compared to the first SKS phase. Synthetics for an 80 km high dome with a width of 136 km are shown in panel (d). The SPdKS phases appear stronger than the SKS phase in this case, and this structure produces strong precursors to the SKS phase, especially at distance ranges 109^0-112^0. The panel (e) shows synthetics for the same dome with different velocity reductions. A substantial trade-off exists between velocity reduction and the vertical dimension of dome structures. While a higher dome tends to increase the strength of the P-diffraction, delay its arrival time and thus make it a more recognizable phase, a lower S-velocity, on the other hand, tends to move the critical angle to a closer distance, reduce the strength of SKS and thus produce a similar waveform. Note that the synthetics from the 40 km dome with a drop of 20% in S-velocity (Figure 6.7b) look similar to those of an 80 km dome with a drop of 10% in S-velocity (Figure 6.7e). For the larger dome, however, precursors appear in SKS-SPdKS synthetics at distance ranges 109^0-113^0 and stronger SPdKS arrivals exist at larger distance ranges.

Long period SKS-SPdKS waveforms are not very sensitive to the smoothness and roughness of those seismic structures, since these long period waveforms are the average effects of the structure (Figure 6.8). Long-period synthetics for a dome with multi-layers (panels a and c) are similar to those of models with a single dome and long-period synthetics from an extremely rough curvature (panels b and d) are similar to those with smooth structures.

6.4 Ultra low velocity zones beneath the south-west Pacific

The above sensitivity studies have demonstrated a variety of SKS-SPdKS waveform complexities required for matching anomalous observed waveshapes not explainable with flat-layer-models. A unique interpretation of this two-dimensional modeling of the data becomes more problematic because of the trade-offs among parameters.

From example, the trade-off between the density change and geometry of the structure makes the density change unresolvable. Nevertheless, useful information about these localized structures, such as the P-velocity reduction, general dimensions, and S-velocity drops required, can be extracted from the data. For example, a P-velocity drop of 10% is required to fit the travel times of the SPdKS phases, localized structures with horizontal length scales of at least 136 km are required to produce anomalous SKS-SPdKS phases, localized structures with vertical length scales of more than 80 km will generate noticeable precursors to SKS phase, and an S velocity drop of 30% rather than 10% is favored, etc.

The observed SKS-SPdKS waveforms shown in Figure 6.1 can be explained by a simple dome-like structure just above the core-mantle boundary. For example, the observed waveforms for the Fiji 1 event can be explained by the synthetics shown in Figure 6.6e; the observed waveforms for the Fiji 2 event can be explained by the synthetics shown in Figure 6.6b,c; and the observed waveforms for the Kermadec event can be explained by the synthetics shown in Figure 6.6d,e. Figure 6.9 shows some comparisons of some of the most anomalous observations with these synthetics. Only observations along the most similar azimuth are chosen (see upper panel for geometry). The corresponding synthetics are selected from Figure 6.6, where the only variable is the position relative to the critical angle. The observed waveforms at BLC and AAM can simply be explained by shifting the dome position by 100 km. The observation of SCB and SCP has been fit by just averaging b and c as a rough approximation of a smaller shift interval. Our best simplified picture of the ultra low velocity zones based on this fit is given in the middle panel of Figure 6.9.

It should be emphasized again that, because of the nature of long period data, the structure shown in Figure 6.9 should be considered a tentative picture. Some of the uniqueness questions can be addressed by broadband data and information from other phases, such as SKKS, PKP, PcP, ScP and ScS, etc. For example, the amplitude ratio of SKKS/SKS can be useful in distinguishing the synthetics of a 40 km high dome with a 20% drop in S-velocity from those of an 80 km high dome with a 10% drop in S-velocity. The roughness and smoothness can also be constrained by short period

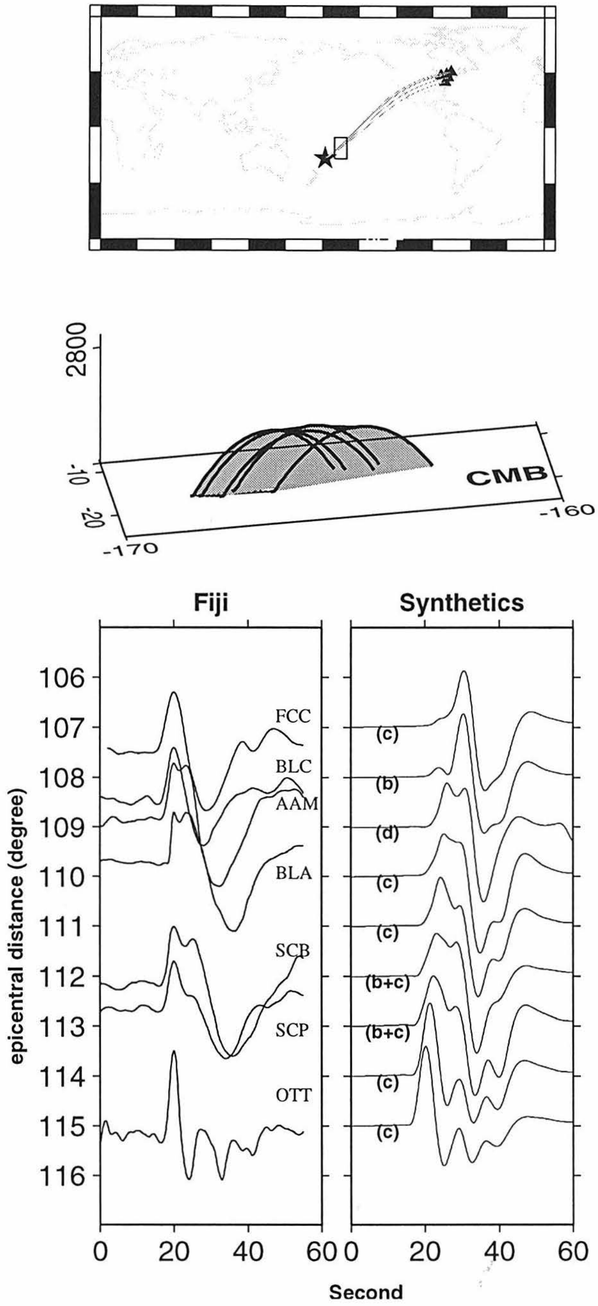

Figure 6.9: The comparison of synthetics and observed waveforms for a Fiji event and the geometry of a three-dimensional structure for producing the synthetics. The seismic anomaly has a P velocity drop of 10%, an S velocity drop of 30% and a density increase of 20% with respect to PREM. Synthetics are chosen from Figure 6.6 and labeled.

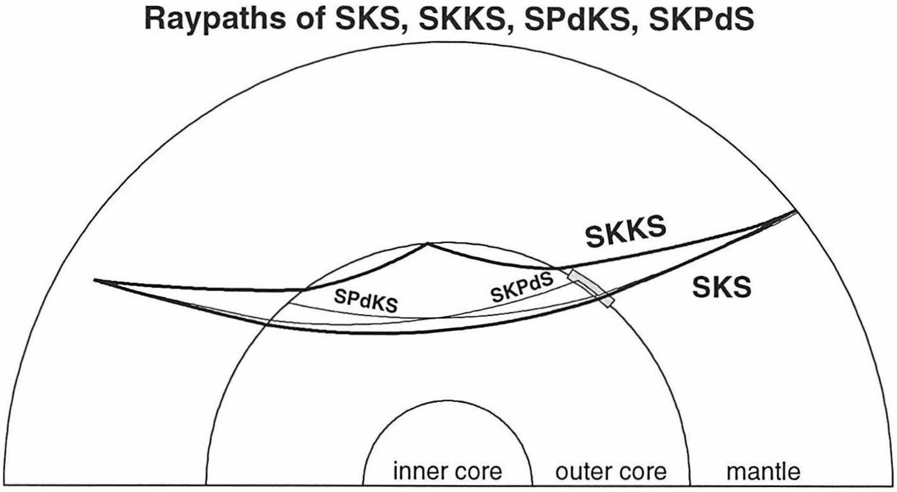

Figure 6.10: Cross section through PREM showing the ray paths of SKS, SKKS, and two diffracted phases SPdKS (source-side) and SKPdS (receiver-side) at a distance of 118^0.

or broadband data, as demonstrated in the studies of short period and broadband scattered precursors to PKP [*Vidale and Hedlin*, 1997; *Wen and Helmberger*, 1997]. How much of this scattered energy distorts the family of PKP phases are addressed in chapter 7. Three-dimensional effects of the seismic structures are also potentially important.

6.5 Ultra low velocity zones beneath Iceland

In this section, we introduce SKKS phase to further constrain ULVZ structures. SKS, SKKS and SKPdS provide ideal sampling to localized structures in the core-mantle boundary region (Figure 6.10). The deep South American earthquakes recorded in Europe provide a good opportunity to image a particularly anomalous region beneath the North Atlantic. Although the SKS family of phases provide quality information, they require relatively deep sources to separate surface reflections (sSKS) from SKKS. Thus, the source regions available are restricted mostly to subduction zones. We selected 20 deep focus earthquakes beneath South America based on their distribution and data quality as observed on long-period WWSSN stations. A sample of these recordings are displayed in Figure 6.11. They are separated into two groups: normal

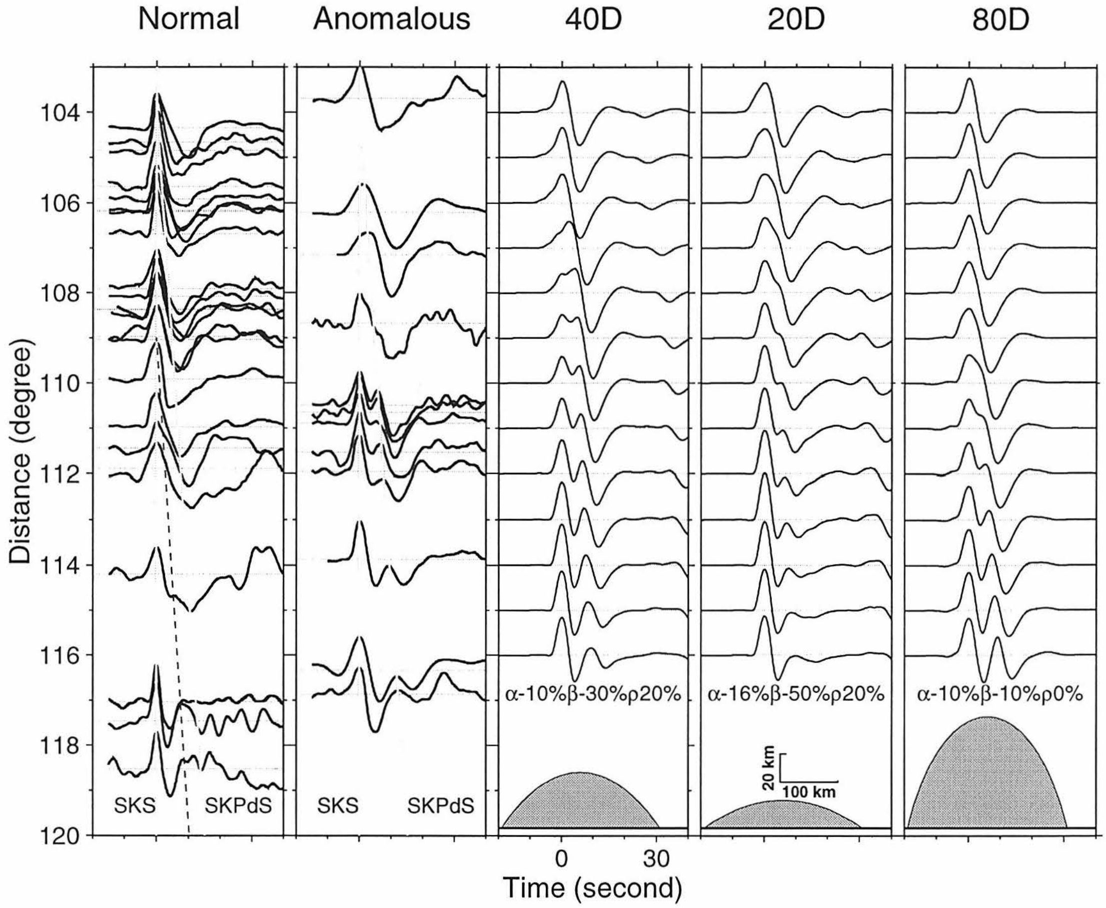

Figure 6.11: Observations of South American events recorded in Europe divided into two groups along with three sets of synthetics. The observations are aligned on SKS with lines indicating the approximate positions of the diffracted phase SKPdS. The synthetics were generated from models containing two-dimensional dome structures with a horizontal scale of 250 km. The dome height varies from 20 to 80 km with corresponding S-wave velocity drops of 50 to 10% and P-wave velocity drops of 16 to 10%.

and anomalous. Some profiles of synthetics are included and will be discussed later. The criterion for normal is that the diffracted phases produce negligible distortion of SKS before 110^0 or PREM-like, essentially waveforms appear similar with range over this interval. These observations show some differences which is mostly caused by variations in source time histories. The records beyond 111^0 show some slight complications which are expected at this region. However, the observations on the right indicate a strong distortion which appears to start developing near 106^0. The station locations, the projected path segments (SPdKS and SKPdS), and the core entry and exit points of SKS and SKKS are displayed in Figure 6.12. Only observations along paths to KEV, KRK, and KBS appear anomalous as displayed in Figure 6.11. Note that if SPdKS were anomalous, it would have affected NUR and UME since the source side segments are nearly identical near the CMB, as indicated in Figure 6.10. Moreover, waveforms observed in the relatively fast regions surrounding the Pacific such as South America and the circum-Pacific belt as denoted in tomographic models [e.g., *Su et al.*, 1994] generally display normal SKS patterns [*Garnero and Helmberger*, 1997]. We conclude that the anomaly must be in SKPdS.

While the SKPdS phase is very anomalous at KEV, the observed separation between the SKKS and the SKS phase is normal as displayed in Figure 6.13. Since SKKS does not reach the S to P critical angle, it remains relatively simple at these ranges and allows easy alignment of observations as indicated. The PREM synthetic fits NUR quite well except for the amplitude ratio of SKKS to SKS, which could be caused by source mechanism. This was not investigated. However, the differential times (SKKS-SKS) for the European observations displayed in Figure 6.13 appear quite normal and PREM-like synthetically.

The paths to Africa encounter the large lower mantle structure which is displayed in Figure 6.12 [*Grand et al.*, 1997]. Most tomography models show this feature but computed differential times between SKKS-SKS correlate poorly from model to model. The two samples displayed in Figure 6.13, to NAI and AAE, indicate their anomalous behavior, but it proves difficult to separate the ULVZ structure that is disturbing AAE from the larger scale neighboring complexity. In contrast, the ULVZ

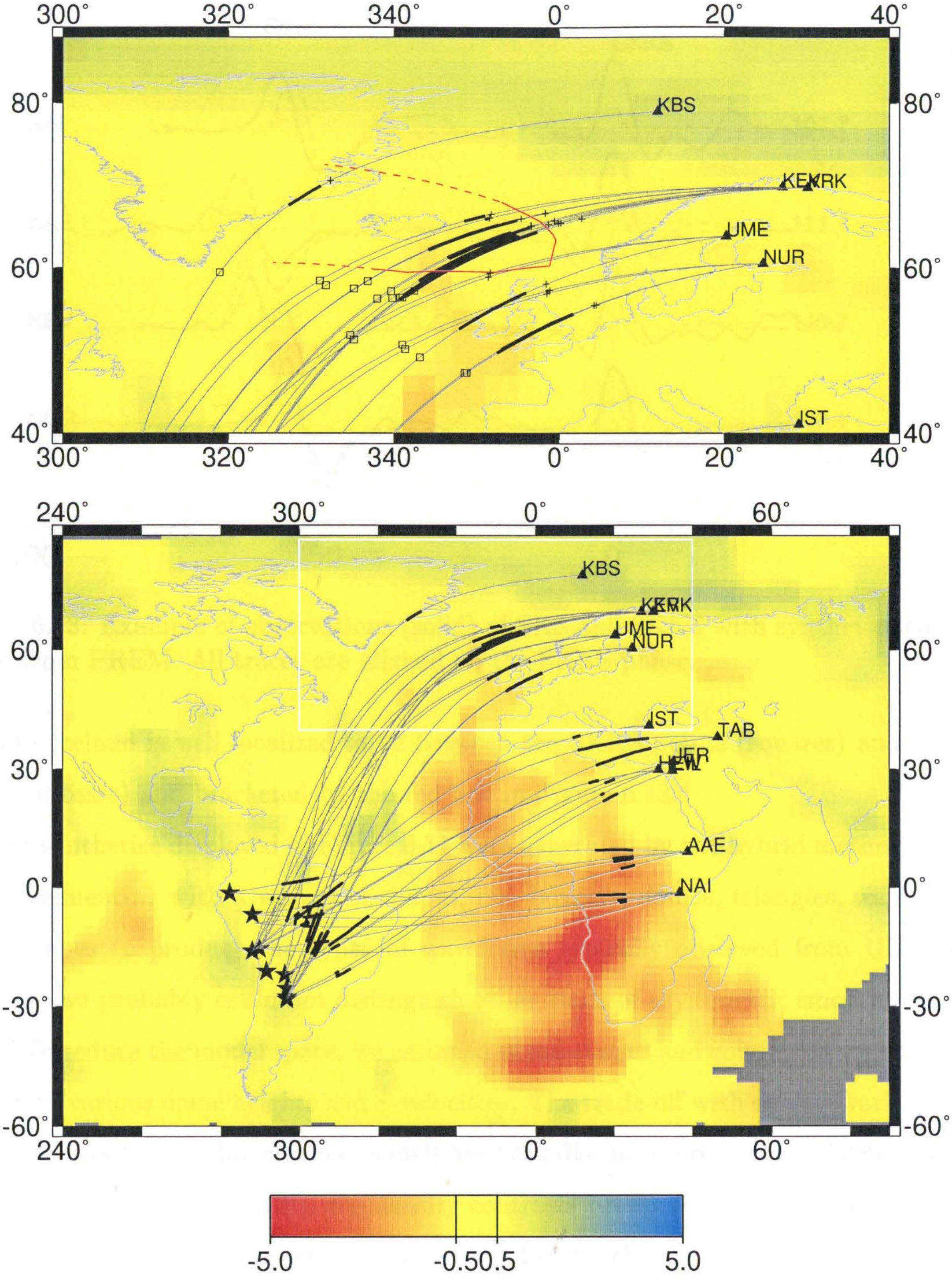

Figure 6.12: Great-circle paths from South American events (stars) to WWSSN stations (triangles) are displayed in the lower map. The heavy line segments indicates the diffracted paths along the core-mantle-boundary. The upper panel shows a blow up of the region beneath the North Atlantic indicating the core-exit points of SKS (crosses) and SKKS (squares). The anomalous structure appears to be bracketed by the red line enclosure located between Norway and Iceland. The background colors indicate the D" velocity structure from [*Grand et al.*, 1997].

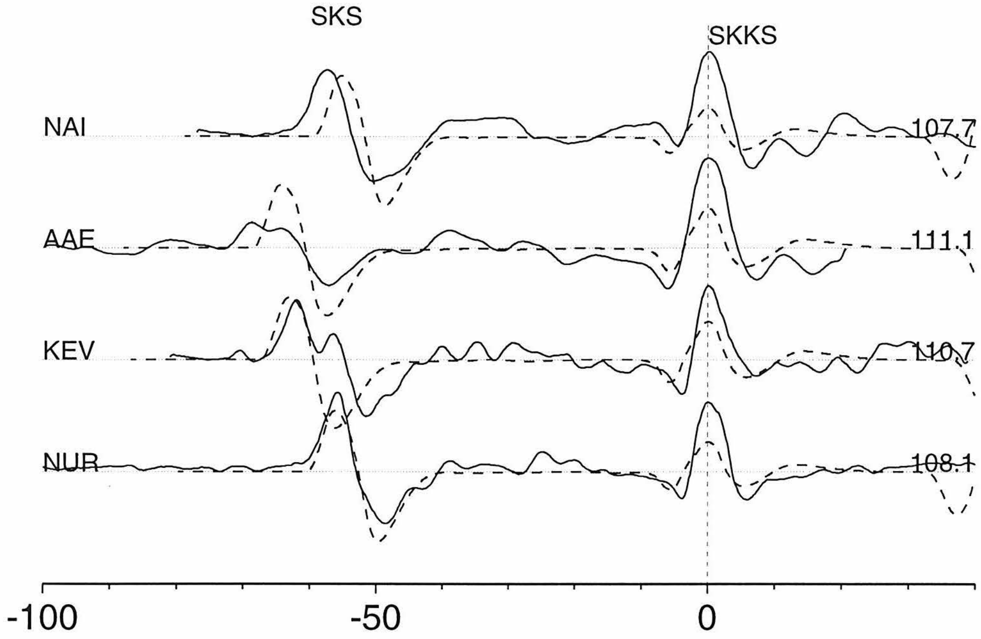

Figure 6.13: Example of observations (solid) of SKS and SKKS with synthetics computed from PREM. All traces are aligned on the SKKS phase.

beneath Iceland is well localized to be between the SKKS points (squares) and SKS points (crosses) and bracketed by the red line in Figure 6.12.

The synthetics displayed in Figure 6.11 were generated by the hybrid method. After experimenting with a variety of shapes, i.e., boxcars, domes, triangles, we found dome-shapes to produce the types of waveforms typically observed from ULVZ's, although we probably could not distinguish other kinds of asymmetric smooth structures. To reduce the model space, we assumed dome-shapes and conducted sensitivity tests with various dome heights and S-velocities. The trade-off with density variations and S-velocity for one-dimensional models has been discussed previously [*Garnero and Helmberger*, 1997]. Essentially, the density contrasts produce effects quite similar to the S-velocity, except that we do not expect density changes to be as great. We selected three sets of synthetics to convey these results as displayed in Figure 6.11. Synthetics for model 40D is considered to provide the overall best fit as determined by waveform matching (overlay). The 20D model with the reduced shear velocity of 50% fits the top set of records 106^0 to 109^0 the best, but the KBS record (109^0) may not be sampling the same structure. The recording of NUR (105^0) is not anomalous but

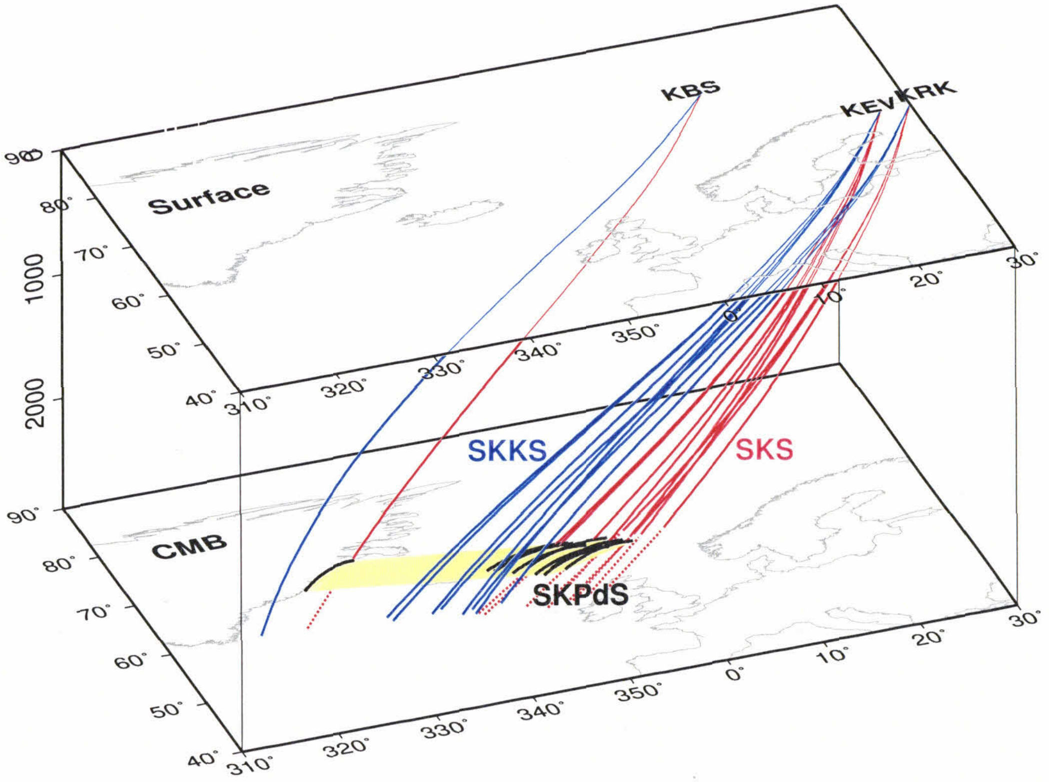

Figure 6.14: Ray paths of SKS, SKPdS and SKKS phases used to constrain the three-dimensional ultra low velocity region (yellow) above the core-mantle boundary beneath Iceland.

comes from the same event, producing KEV at 106^0 to demonstrate that the broadness at KEV is not caused by the source. Zones with thicknesses less than 20 km with large S-velocity drops are particularly good at producing broad pulses. Thicker zones generally produce a stronger SKPdS phase and the prominent waveform distortions beyond 110^0. The 80D model with the S-velocity drop of 10% produces too much ringing at the larger distances. However, given the number of idealizations made with respect to the exact location and geometry involved, it proves difficult to argue for uniqueness at this stage by modeling only the diffracted wavefield. But the compatibility with the width estimate (250 km) from travel time differentials, essentially the zone enclosed by the red contour in the upper panel of Figure 6.12, with the waveform data is quite supportive of this waveform analysis. The ray paths of SKS, SKPdS and SKKS constrain the three-dimensional structure of ultra low velocity zones beneath Iceland (Figure 6.14).

6.6 Conclusion

We apply the hybrid method to study the wave propagation problem for an ultra-low velocity zone near the core-mantle boundary. Localized dome-shaped structures with a horizontal length scale of about 250 km, a vertical length scale of 40 km, a P wave velocity reduction of 10%, an S wave velocity 30% and a density increase of 20% produce SKS-SPdKS waveforms which fit the most anomalous records not explainable by one-dimensional models. The general structural shape and location of the localized structure are constructed from the modeling of the Fiji and Iceland data, since the complexity of waveforms is sensitive to the position of the localized structure above the core-mantle boundary, although several important issues, such as the density change and the roughness of the localized structures and the smoothness of the transition from these structures, remain unresolved due to the nature of the data. Broadband data and information from other phases are required to resolve these fine structures.

Chapter 7 Ultra low velocity zones at the core-mantle boundary from broadband PKP precursors

7.1 Abstract

Short and long period precursors of PKP phase have been found and we use these to map detailed seismic structures of ultra low velocity zones (ULVZ) at the core mantle boundary (CMB). Synthetics are computed from a new hybrid method allowing for two-dimensional complex structures. Long period precursors are explained by 60-80 km high Gaussian shaped ULVZs with P-velocity drops by at least 7% over 100-300 km. Short period precursors suggest the presence of smaller scales anomalies adjacent to the larger Gaussian-shaped structures. These fine structures may be indicatives of partial melt caused by vigorous small-scale convection or the instability of a thermal boundary layer at the mantle's base.

7.2 PKP precursors and ultra low velocity zones at the core mantle boundary

The scale, magnitude and geometry of seismic heterogeneities near the core-mantle boundary (CMB) region provide important implications on mineralogy [e.g., *Williams and Garnero*, 1996; *Holland and Ahrens*, 1997] and the geodynamical [e.g., *Olsen et al.*, 1987; *Hedlin et al.*, 1997] evolution of the Earth. While global seismic tomography is revealing large scale seismic structure of a slower than average mid-Pacific surrounded by a donut-shaped faster than average circum-Pacific region with velocity perturbations of up to ±3% in the lower mantle [e.g., *Liu and Dziewonski*, 1994], recent studies of core phases suggest the existence of ultra-low velocity layers (zones) beneath Iceland [*Helmberger et al.*, 1997] and Western Pacific regions [*Garnero and Helmberger*, 1995; *Mori and Helmberger*, 1995; *Wen and Helmberger*, 1998; *Vidale and Hedlin*, 1997]. The Western Pacific region appears to be unique in that the deep seismicity associated with the Tonga-Fiji seismic belt produces excellent quality seismograms recorded globally. Figure 7.1 shows the sampled CMB regions in the Western Pacific from previous studies, along with seismic velocity perturbations in the lowermost mantle [*Su et al.*, 1994]. Unfortunately, the detailed structures of those ultra low velocity zones (layers) are poorly constrained [e.g., *Wen and Helmberger*, 1998].

While short PKP precursors have been noted on the world-wide standard seismic network (WWSSN) for many years [*Haddon and Cleary*, 1974], they have not been used in combination with long period precursors. Long period energy arriving before PKP has been noted earlier by *Buchbinder* [1974]; however, these signals were attributed to PKP diffractions unrelated to CMB structures. We consistently observe both long and short period precursors of PKP at stations in Eastern Europe for earthquakes occurred in Fiji subduction zone. With these observations and recent development of techniques for calculating synthetic seismograms, we are able to map detailed localized seismic structures in the CMB region satisfying both data types. Here, we present results for an example event. The PKP ray paths for two representive stations of a Fiji event (magnitude 5.9) on September 12, 1968, (179.4W,21.6S, 635 km depth) are also shown in Figure 7.1. The heavy lines in Figure 7.1 indicate the source-side core-mantle boundary regions sampled by the precursors. Seismograms recorded by long and short period WWSSN instruments at stations TAB and UME are shown in Figures 7.2a,b. The short period records (right) in Figures 7.2a,b display a distribution of strong precursors to the geometric PKP arrivals, similar to the observation of *Vidale and Hedlin* [1997]. Similar results are seen at other stations with different degrees of complexity. Some long period motions arriving before the PKP phases in synthetics of one-dimensional models, such as PREM (Preliminary Earth Reference Model) [*Dziewonski and Anderson*, 1981], are essentially caused by diffraction into the fluid core shadow zone, but they are very long period in character as shown in the synthetics labeled PREM in Figures 7.2a,b [*Kind and Müller*, 1975; *Cormier and Richards*, 1977]. In short, these long period observations show clear arrivals with periods similar to PKP.

At epicentral distances 120-144^0, the first arrival is PKP (PKIKP or PKPdf) (Figure 7.3). For a radially symmetrical Earth model such as PREM, there is no geometrical arrival possible because of the shadow zone resulting from the P velocity drop from the mantle to the core. However, if there are scatterers in the lowermost mantle, seismic rays effectively change their ray parameter and propagate back to the Earth's surface via other paths. Some of those perturbated rays can arrive earlier than the PKP phase and appear as precursors to PKP [*Cleary and Haddon*, 1972; *Haddon and Cleary*, 1974; *Cormier*, 1995]. Figure 7.3 also shows ray paths of those precursors and the shaded region indicates scatterer locations which will produce seismic arrivals prior to the PKP phase. The arrival time of the precursor depends on the radial and lateral locations of the scatterers and the amplitude of the precursor constrains the size and geometry of the scatterers. Thus, the timing and amplitude of precursors, especially broadband observations, provide a unique opportunity to explore the scale, magnitude, and geometry of fine seismic structures in the lowermost mantle. Figure 7.4 shows the relative travel time of precursors to PKP phase as a function of lateral distance of the corresponding scatterers, assuming four different depths of the scattering. Each trace corresponds to an event-receiver pair at a certain distance. It is obvious that there is a trade-off between the depth and lateral location of scatterers for a precursor arriving in a certain time window, and furthermore, scatterers beneath receivers can cause scattering as well.

Several independent lines of evidence suggest that the broadband PKP precursors in Figures 7.2a,b are caused by source side scattering: 1) source side regions appear also to have slower than average velocity in global seismic tomographic models [e.g., *Su et al.*, 1994]; 2) the adjacent regions in source side appear to be very anomalous, as indicated by boxes in Figure 7.1. For these reasons, we assume that the scattering occurred in the source side only, although our data could be explained by the receiver-

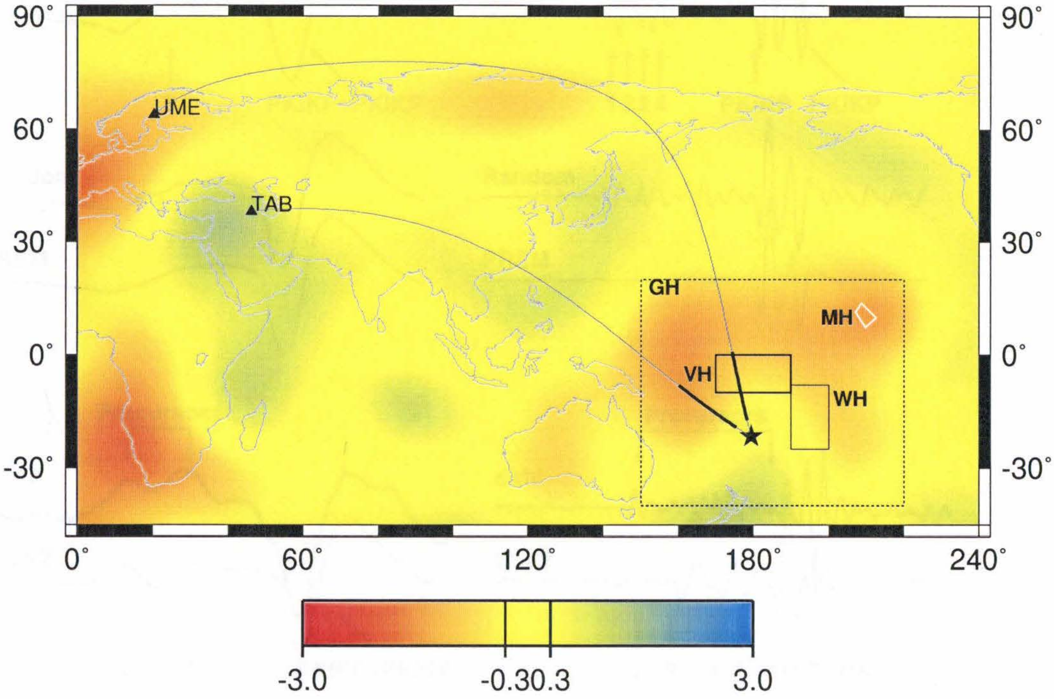

Figure 7.1: The sampled CMB regions in the Western Pacific from previous studies, along with the large scale seismic velocity structure of *Su et al.* [1994] of the lowermost mantle. The dash box GH contains results of *Garnero and Helmberger* [1995] on the ultra low velocity layers with P velocity reduction of up to 10% from long period SKS (SV wave in the mantle and P wave in the fluid core) and SPdKS (containing a P diffracted segment along the CMB); the light box WH reports on modeling a two-dimensional structure 40 km high with a P velocity drop of 10% and an S velocity drop of 30% and a horizontal length scale of 250 km from long period SKS and SPdKS phases [*Wen and Helmberger*, 1998]; the white box MH reports on strong P velocity reductions to explain the precursors to short period PcP (reflected wave from the CMB) by *Mori and Helmberger* [1995]; and heavy line box is reported to contain strong scatterers to explain intense short-period precursors to PKP phase, which are observed at NORSAR, a seismic station array near UME [*Vidale and Hedlin*, 1997]. The shaded lines are the CMB regions sampled by the PKP precursors at stations TAB and UME studied in this report.

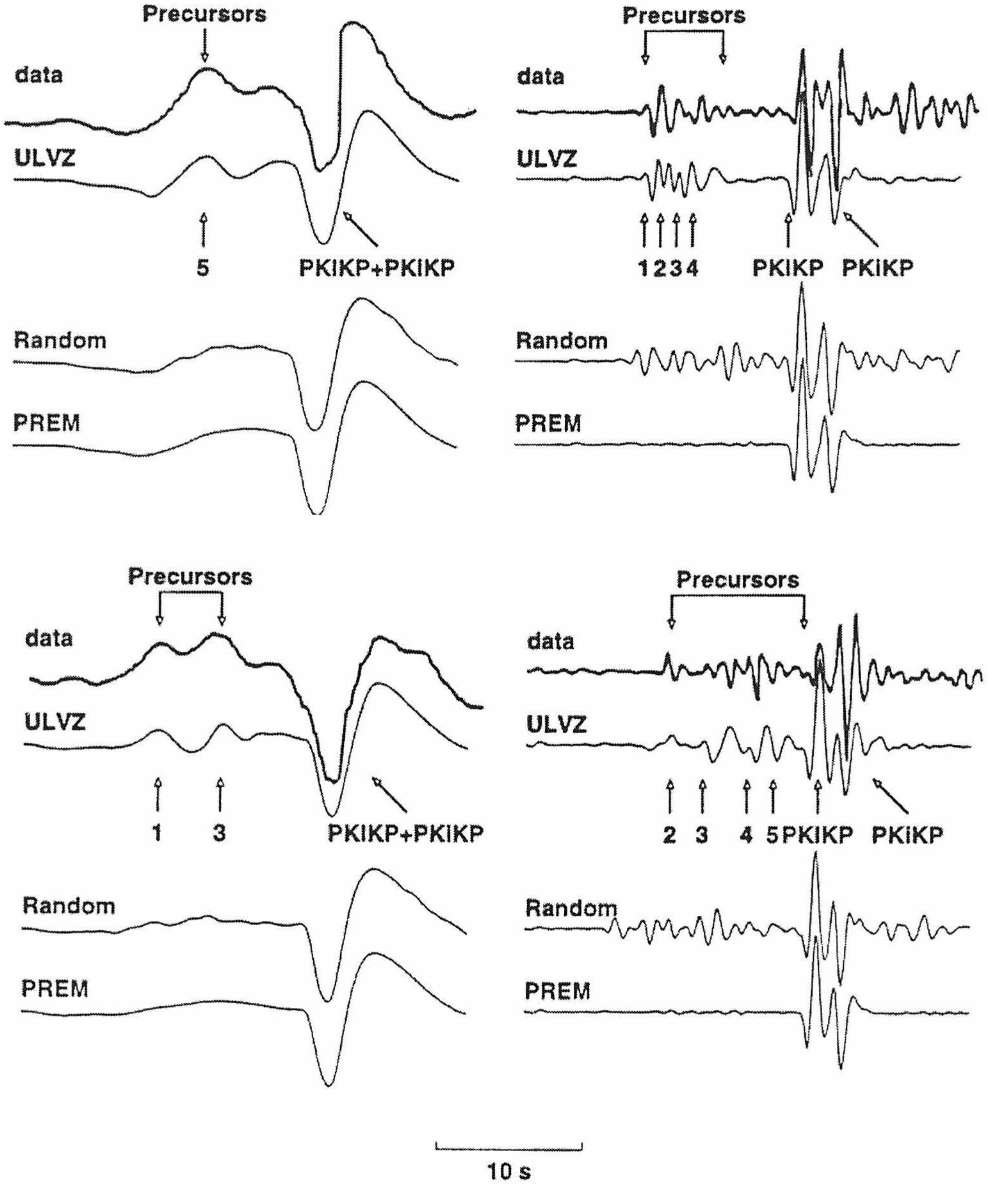

Figure 7.2: The observed long and short period PKP phase and precursors along with synthetics produced by various models at TAB (a) and UME (b). Three sets of synthetics are displayed, based on PREM, a random model (correlation length of 8 km and r.m.s. variation of 8%) and the ultra-low velocity structures shown in Figure 7.5. The arrows indicated by the numbers correspond to the precursors produced by the structures as indexed in Figure 7.5. All synthetics are calculated by the hybrid method [*Wen and Helmberger*, 1998]. The PKIKP is the P wave propagating from the mantle into the inner core and returning to the Earth's surface. PKiKP travels a similar path except that it reflects off the inner core boundary. The smaller observed PKIKP phases compared to synthetics of one-dimensional models have been attributed to the absorption of the upper-most inner core [*Cormier*, 1995; *Song and Helmberger*, 1995a]. Therefore, the precursors should be compared to PKiKP in assessing their strength.

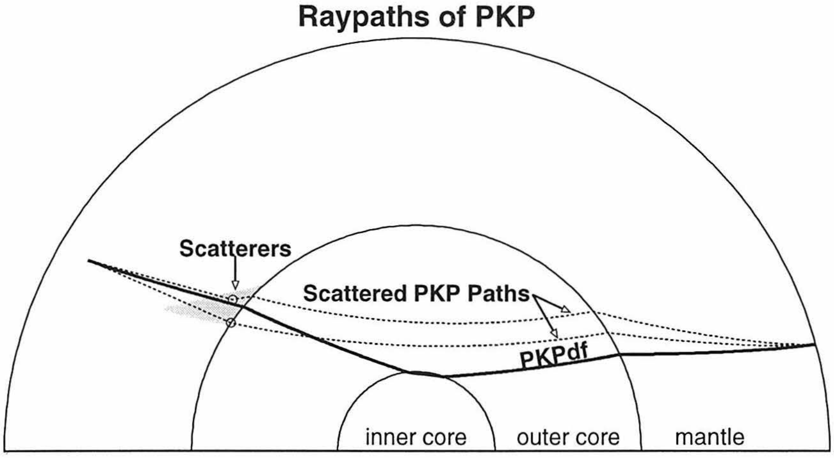

Figure 7.3: A display of ray paths of PKIKP and precursors of PKP at an epicentral distance of 136^0. The shaded region indicates the scatterer locations which will produce seismic arrivals prior to PKIKP phase. The reference model is PREM [*Dziewonski and Anderson*, 1981].

side scattering as well.

To generate synthetics containing extreme scattering expected from complex structures, we used a hybrid method, which interfaces the numerical finite-difference technique with analytical methods. This allows high resolution study since the finite-difference technique is applied only in heterogeneous regions [*Wen and Helmberger*, 1998]. Adopting the value of correlation length (8 km) of scattering obtained from global average data based on the assumption of uniform scattering [*Hedlin et al.*, 1997], at least 8% of r.m.s velocity perturbation is required to explain the observed short period scattered energy. Synthetics for this random model and the PREM are shown in Figures 7.2a,b. Note that although the amplitudes of the short period precursors are well predicted by this random model, the waveforms do not fit the data. Moreover, random models do not produce significant long period energy precursors. Note that the long period waveforms from the random model are very similar to those produced by the PREM. Coherent and continuous larger-scale structures are required to explain the long-period precursors.

The earliest arrival of precursor recorded at TAB is consistent with scatterers located at the lowermost 150 km of the mantle. However, because of the trade-off

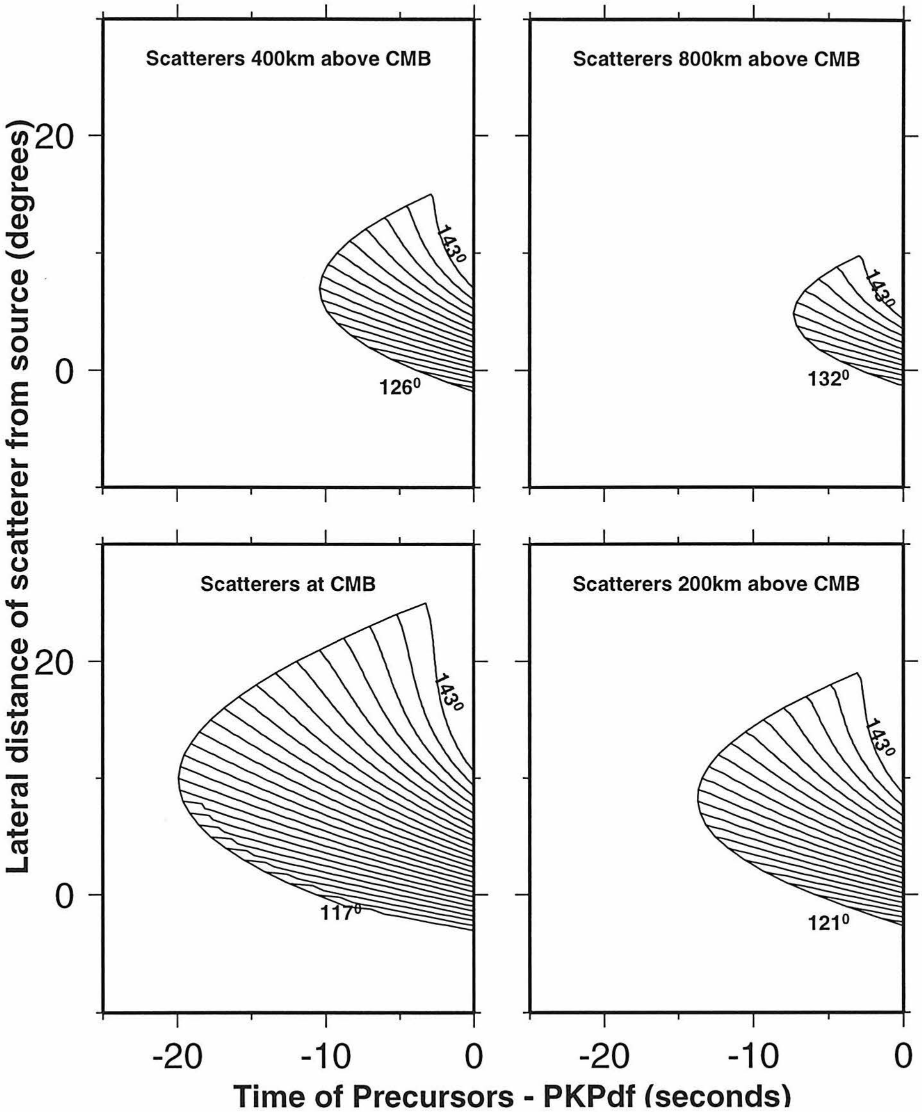

Figure 7.4: Plots of travel time of precursors as a function of lateral distance of scatterers from seismic source. Each panel assumes a different depth of scatterer and each trace corresponds to an event-receiver pair. The increment of epicentral distance between traces is 1^0.

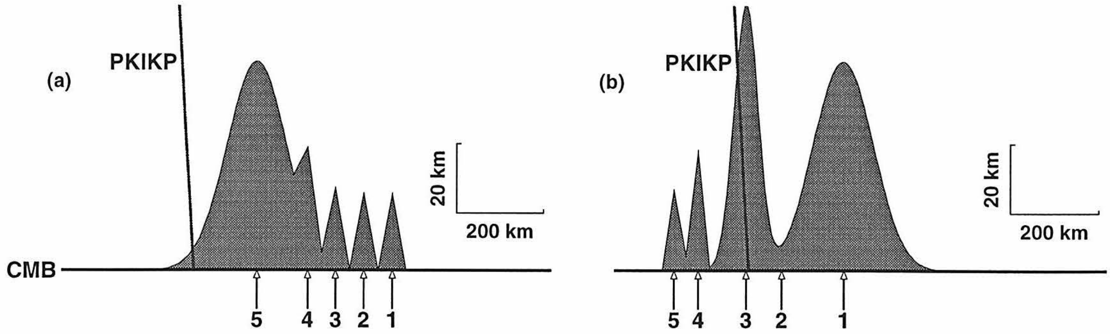

Figure 7.5: The two-dimensional cross sections of seismic structure derived by fitting the broadband PKIKP precursors observed at TAB (a) and UME (b). The geographic locations of these two-dimensional cross sections are indicated by heavy lines in Figure 7.1. The numbers indicate structures which produce precursors as indexed in Figure 7.2. The shaded regions have a P velocity drop of 10%.

between depth and lateral location of those scatterers, the exact location of scatterers cannot be constrained from UME data alone. We assume that the scatterers are located at the bottom of the mantle, in agreement with the position suggested by PcP precursors. Numerical tests indicate that structures with horizontal and vertical length scales of 100-300 km and 60-80 km respectively and P velocity drops of at least 7% are required to explain the observed long-period precursors. That no short period precursors are associated with the onsets of long period arrivals suggests that the structures with these length scales have smooth edges, as opposed to dome-shaped structures used in modeling long period SPdKS phase [*Wen and Helmberger*, 1998]. The timing of short period precursors suggests that small scale structures accompany, rather than being superimposed on these large scale structures. Two-dimensional cross sections of the structure are shown in Figures 7.5. Both long and short period synthetics produced by these two structures (Figures 7.2a,b, labeled as ULVZ) fit the data well. The seismic energy produced by the corresponding structures are indicated by the index numbers. Although the details of real structure may be different from our two-dimensional models, the overall structure of our two-dimensional models is representative of the scale, magnitude and geometry of real structures. Since the behaviors of short period observation are affected by many factors, we have not made further efforts to modify our two-dimensional models to find a better fit to the short period precursors.

We tested a number of other possible explanations, i.e., topographic reliefs as proposed by [*Doornbos*, 1978]. However, topography at the core-mantle boundary even with magnitude of 5 km produces little long period energy. The same is true with the structures with increased P velocity. Although the topography at the core-mantle boundary may contribute some portion of precursor energy, it is unlikely that the topographic effects are the dominating factor in explaining the data. The long period precursors are generated by the wide angle reflection from the right-hand side of the Gaussian-like structures. However, there is a trade-off between P velocity drop and heights of the structures, but structures with P velocity drops of at least 7% are required to produce synthetics which fit these particular records.

It is clear that broadband precursors can be explained by ULVZs with different length scales. Thin (e.g., 5 km) ULVZ will produce short period precursors, as normally observed, if it is sufficiently rough. Structures with these length scales are, however, less detectable from SKS and SKPdKS waveforms [*Helmberger et al.*, 1996]. It is conceivable that many ULVZs are undetected in mid-Pacific and other hotter than average regions, because of their less detectability and data coverage. It is interesting to note that PKP precursors are absent from paths sampling beneath the Americas [*Bataille et al.*, 1990; *Song and Helmberger*, 1995b], which is faster, and presumably colder, than average mantle [e.g., *Su et al.*, 1994] The correlation of absence (presence) of ULVZ and little (strong) PKP precursors suggests that ULVZs with different length scales may be a major contributor to broadband PKP precursors.

The magnitudes of P velocity drops of these ULVZs and S velocity drop of 30% of other ULVZs [*Wen and Helmberger*, 1998] are consistent with partial melt [*Williams and Garnero*, 1996]. The length scale and geometry of these ULVZs suggest that these ULVZs may be indicatives of small-scale mantle convection or instability of the bottom thermal boundary layer of the mantle. It may be possible to use the length scale, magnitude and geometry of the ULVZs to constrain local Rayleigh number of small scale convection thereby providing an estimate of the radial and lateral viscosity structure of the CMB region.

Bibliography

Alexander, S. S., and R. A. Phinney, A study of the core-mantle boundary using P waves diffracted by the Earth's core, *J. Geophys. Res.*, *71*, 5,943–5,958, 1966.

Allan, D. W., W. B. Thompson, and N. O. Weiss, Convection in the Earth's mantle, in *Mantles of the Earth and Terrestrial Planets*, edited by S. K. Runcorn, pp. 507–512, Interscience, London, 1967.

Alterman, Z. S., and F. C. Karal, Propagation of elastic waves in layered media by finite-difference methods, *Bull. Seism. Soc. Am.*, *58*, 367–398, 1968.

Anderson, D. L., Recent evidence concerning the structure and composition of the Earth's mantle, in *Physics and chemistry of the Earth*, vol. 6, pp. 1–131, Pergamon Press, 1966.

Anderson, D. L., Phase change in the upper mantle, *Science*, *157*, 1165–1173, 1967.

Anderson, D. L., *Theory of the Earth*, Blackwell, Boston, 1989.

Anderson, D. L., and J. D. Bass, Mineralogy and composition in the upper mantle, *Geophys. Res. Lett.*, *11*, 637–640, 1984.

Anderson, D. L., T. Tanimoto, and Y.-S. Zhang, Plate tectonics and hotspots: The third dimension, *Science*, *256*, 1645–1651, 1992.

Balachandar, S., Eigenfunctions of the two-point correlations for optimal characterization of mantle convection: possibility of additional discontinuity around 850km, *EOS*, *76*, F618, 1995.

Bataille, K., R.-S. Wu, and S. M. Flatte, Inhomogeneities near the core-mantle boundary evidenced from scattered waves: A review, *PAGEOPH*, *132*, 151–173, 1990.

Bercovici, D., A simple model of plate generation from mantle flow, *Geophys. J. Int.*, *114*, 635–650, 1993.

Bercovici, D., Plate generation in a simple model of lithosphere-mantle flow with dynamic self-lubrication, *Earth Planet. Sci. Lett.*, *144*, 41–51, 1996.

Boore, D. M., Finite-difference methods for seismic wave propagation in heterogeneous materials, in *Methods of Computational Physics*, edited by M. R. B. Alder, S. Fernbach, vol. 12, pp. 1–37, Academic Press, London, 1972.

Buchbinder, G. R., Diffraction from the PKP caustic B, *Bull. Seism. Soc. Am.*, *64*, 33–43, 1974.

Bunge, H.-P., M. A. Richards, and J. R. Baumgardner, Effect of depth-dependent viscosity at the plateform of mantle convection, *Nature*, *379*, 436–438, 1996.

Cadek, O., and Z. Martinee, Spherical harmonic expansion of the Earth's crustal thickness up to degree and order 30, *Stud. Geophys. Geod.*, *35*, 151–165, 1991.

Cadek, O., Y. Ricard, Z. Martinec, and C. Matyska, Comparison between Newtonian and non-Newtonian flow driven by internal loads, *Geophys. J. Int.*, *112*, 103–114, 1993.

Cazenave, A., K. Dominh, C. J. Allegre, and J. G. Marsh, Global relationship between oceanic geoid and topography, *J. Geophys. Res.*, *91*, 11439–11450, 1986.

Cazenave, A., A. Souriau, and K. Dominh, Global coupling of the Earth surface topography with hotspots, geoid and mantle heterogeneity, *Nature*, *340*, 54–57, 1989.

Cazenave, A., and B. Lago, Long wavelength topography, seafloor subsidence and flattening, *Geophys. Res. Lett.*, *18*, 1257–1260, 1991.

Cazenave, A., and C. Thoraval, Mantle dynamics constrained by degree 6 surface topography, seismic tomography and geoid: Inference on the origin of the South Pacific Superswell, *Earth Planet. Sci. Lett.*, *122*, 207–219, 1994.

Chapman, C. H., Exact and approximate generalized ray theory in vertically inhomogeneous media, *Geophys. J. R. Astron. Soc.*, *46*, 201–233, 1976.

Chapman, C. H., and J. A. Orcutt, The computation of body wave synthetic seismograms in laterally homogeneous media, *Rev. Geophys.*, *23*, 105–163, 1985.

Choy, G. L., Theoretical seismograms of core phases calculated by frequency-dependent full wave theory, and their interpretation, *Geophys. J. R. Astron. Soc.*, *51*, 275–312, 1977.

Christensen, U. R., and H. Harder, 3-D convection with variable viscosity, *Geophys. J. Int.*, *104*, 213–226, 1991.

Cleary, J. R., and R. A. W. Haddon, Seismic wave scattering near the core-mantle boundary: a new interpretation of precursors to PKP, *Nature*, *240*, 549–551, 1972.

Colin, P., and L. Fleitout, Topography of the ocean floor: thermal evolution of the lithosphere and interaction of mantle heterogeneities with the lithosphere, *Geophys. Res. Lett.*, *11*, 1961–1964, 1990.

Cormier, V. F., Time-domain modelling of PKIKP precursors for constraints on the heterogeneity in the lowermost mantle, *Geophys. J. Int.*, *121*, 725–736, 1995.

Cormier, V. F., and P. G. Richards, Full-wave theory applied to a discontinuous velocity increase: The inner core boundary, *J. Geophys.*, *43*, 3–31, 1977.

Crough, S. T., and D. M. Jurdy, Subducted lithosphere, hotspots and the geoid, *Earth Planet. Sci. Lett.*, *48*, 15–22, 1980.

de Jonge, M. R., M. J. R. Wortel, and W. Spakman, Regional scale tectonic evolution and the seismic velocity structure of the lithosphere and the upper mantle: The Mediterranean region, *J. Geophys. Res.*, *99*, 12091–12108, 1994.

Doornbos, D. J., Characteristics of lower mantle heterogeneities from scattered waves, *Geophys. J. R. Astron. Soc.*, *44*, 447–470, 1976.

Doornbos, D. J., On seismic wave scattering by a rough core-mantle boundary, *Geophys. J. R. Astron. Soc.*, *53*, 643–662, 1978.

Doornbos, D. J., Multiple scattering by topographic relief with application to the core-mantle boundary, *Geophys. J. Int.*, *92*, 465–478, 1988.

Doornbos, D. J., and T. Hilton, Models of the core-mantle boundary and the travel times of internally reflected core phases, *J. Geophys. Res.*, *94*, 15741–15751, 1989.

Dziewonski, A., and D. L. Anderson, Preliminary reference Earth model, *Phys. Earth Planet. Int.*, *25*, 297–356, 1981.

Elsasser, W. M., Convection and stress propagation in the upper mantle, in *The Application of Modern Physics to the Earth and Planetary Interiors*, edited by S. K. Runcorn, Wiley-Interscience, 1969.

Emmerich, H., 2-D wave propagation by a hybrid method, *Geophys. J. Int.*, *99*, 307–319, 1989.

Estey, L. H., and B. J. Douglas, Upper mantle anisotropy: a preliminary model, *J. Geophys. Res.*, *91*, 11393–11406, 1986.

Fleitout, L., Source of lithospheric tectonic stress, *Phil. Trans. R. Soc. Lond.*, *A 337*, 73–81, 1991.

Forte, A. M., and W. R. Peltier, Plate tectonics and aspherical Earth structure: The importance of poloidal-toroidal coupling, *J. Geophys. Res.*, *92*, 3645–3679, 1987.

Forte, A. M., and W. R. Peltier, Viscous flow models of global geophysical observables, 1, Forward problems, *J. Geophys. Res.*, *96*, 20131–20159, 1991.

Forte, A. M., A. M. Dziewonski, and R. L. Woodward, Aspherical structure of the mantle tectonics, nonhydrostatic geoid and the topography of the core-mantle boundary, in *Dynamics of the Earth's Deep Interior and Earth Rotation,* Geophys. Monogr Ser., edited by J. L. Mouel, D. E. Smylie, and T. Herring, vol. 72, pp. 135–166, Washington, D. C., 1993.

Forte, A. M., W. R. Peltier, A. M. Dziewonski, and R. L. Woodward, Dynamic surface topography: A new interpretation based upon mantle flow models derived from seismic tomography, *Geophys. Res. Lett.*, *20*, 225–228, 1993b.

Forte, A. M., A. M. Dziewonski, and R. J. O'Connell, Continent ocean chemical heterogeneity in the mantle based on seismic tomography, *Science*, *268*, 386–388, 1995.

Fukao, Y., M. Obayashi, H. Inoue, and M. Nenbai, Subducting slabs stagnant in the mantle transition zone, *J. Geophys. Res.*, *97*, 4809–4822, 1992.

Gable, C. W., R. J. O'Connell, and B. J. Travis, Convection in three dimensions with surface plates: Generation of toroidal flow, *J. Geophys. Res.*, *96*, 8391–8405, 1991.

Gantmacher, F. R., The Theory of Matrices, vol. 2, translated from Russian by K. A. Hirsch, Chelsea, New York, 1960.

Garnero, E. J., S. P. Grand, and D. V. Helmberger, Low P-wave velocity at the base of the mantle, *Geophys. Res. Lett.*, *23*, 977–980, 1993.

Garnero, E. J., and D. V. Helmberger, A very slow basal layer underlying large-scale low-velocity anomalies in the lower mantle beneath the Pacific: evidence from core phases, *Phys. Earth Planet. Int.*, *91*, 161–176, 1995.

Garnero, E. J., and D. V. Helmberger, Seismic detection of a thin laterally varying boundary layer at the base of the mantle beneath the central-Pacific, *Geophys. Res. Lett.*, *23*, 977–980, 1996.

Garnero, E. J., and D. V. Helmberger, Further constraints and uncertainties in modeling a thin laterally varying ultra low velocity layer at the base of the mantle, *J. Geophys. Res.*, *Submitted*, 1997.

Gordon, R. G., and D. M. Jurdy, Cenozoic global plate motions, *J. Geophys. Res.*, *91*, 12389–12406, 1986.

Grand, S. P., Mantle shear structure beneath the Americas and surrounding oceans, *J. Geophys. Res.*, *99*, 11591 – 11622, 1994.

Grand, S. P., R. D. van der Hilst, and S. Widiyantoro, Global seismic tomography: a snapshot of convection in the Earth, *GSA today*, *7*, 1–7, 1997.

Gurnis, M., A reassessment of the heat transport by variable viscosity convection with plates and lids, *Geophys. Res. Lett.*, *16*, 179–182, 1989.

Gurnis, M., Bounds on global dynamic topography from Phanerozoic flooding of continental platforms, *Nature*, *344*, 754–756, 1990.

Gurnis, M., and S. Zhong, Dynamics influences of plates with faulted and mobile margins on slab penetration through the 670-km phase change, *Eos Trans, AGU, Spring Meeting Suppl.*, *76*, S57, 1995.

Gwinn, C. R., T. A. Herring, and I. I. Shapiro, Geodesy by radio interferometry: Studies of the forced nutations of the Earth 2. Interpretation, *J. Geophys. Res.*, *91*, 4755–4765, 1986.

Haddon, R. A., and J. R. Cleary, Evidence for scattering of seismic PKP waves near the core-mantle boundary, *Phys. Earth Planet. Int.*, *8*, 211–234, 1974.

Hager, B. H., and R. J. O'Connell, Kinematic models of large-scale flow in the Earth's mantle, *J. Geophys. Res.*, *84*, 1031–1048, 1979.

Hager, B. H., and R. J. O'Connell, A simple global model of plate dynamics and mantle convection, *J. Geophys. Res.*, *86*, 4843–4878, 1981.

Hager, B. H., Subducted slabs and the geoid: Constraints on mantle rheology and flow, *J. Geophys. Res.*, *89*, 6003–6015, 1984.

Hager, B. H., R. W. Clayton, M. A. Richards, R. P. Comer, and A. M. Dziewonski, Lower mantle heterogeneity, dynamic topography and the geoid, *Nature*, *313*, 541–545, 1985.

Hager, B. H., and R. W. Clayton, Constraints on the structure of mantle convection using seismic observations, flow models, and the geoid, in *Mantle Convection*, edited by W. R. Peltier, pp. 657–764, Gordon and Breach, Newark, N. J., 1989.

Hager, B. H., and M. A. Richards, Long-wavelength variations in Earth's geoid: physical models and dynamical implications, *Phil. Trans. Roy. Soc.*, *A 328*, 309–327, 1989.

Hara, T., and R. Geller, The geological origin of long wavelength lateral heterogeneity at depths of 300-400 km, *Geophys. Res. Lett.*, *21*, 907–910, 1994.

Hedlin, M. A. H., P. M. Shearer, and P. S. Earle, Seismic evidence for small-scale heterogeneity throughout the Earth's mantle, *Nature*, *387*, 145–150, 1997.

Heestand, R. L., and S. T. Crough, The effect of hotspots on the oceanic age-depth relation, *J. Geophys. Res.*, *86*, 6107–6114, 1981.

Helmberger, D. V., The crust-mantle transition in the Bering Sea, *Bull. Seism. Soc. Am.*, *58*, 179–214, 1968.

Helmberger, D. V., Theory and application of synthetic seismograms, in *Earthquakes: Observation, Theory and Interpretation*, edited by H. Kanamori, pp. 173–222, Soc. Italiana di Fisica, Bologna, Italy, 1983.

Helmberger, D. V., E. J. Garnero, and X. Ding, Modeling two-dimensional structure at the core-mantle boundary, *J. Geophys. Res.*, *101*, 13,963–13,972, 1996.

Helmberger, D. V., L. Wen, and X. Ding, Ultra low velocity zone beneath Iceland, *Nature*, *submitted*, 1997.

Holland, K. G., and T. J. Ahrens, Melting of (Mg, Fe)$_2$SiO$_4$ at the core-mantle boundary of the Earth, *Science*, *275*, 1,623–1,625, 1997.

Hong, T. L., and D. V. Helmberger, Glorified optics and wave propagation in nonplanar structure, *Bull. Seism. Soc. Am.*, *68*, 1,313–1,330, 1978.

Igel, H., and M. Weber, P-SV wave propagation in the Earth's mantle using finite-difference: Application to heterogeneous lowermost mantle structure, *Geophys. Res. Lett.*, *23*, 415–418, 1996.

Ivins, E. R., C. G. Sammis, and C. F. Yoder, Deep mantle viscous structure with prior estimate and satellite constraint, *J. Geophys. Res.*, *98*, 4579–4609, 1993.

Jeanloz, R., Effects of phase transitions and possible compositional changes on the seismological structure near 650 km depth, *Geophys. Res. Lett.*, *18*, 1743–1746, 1991.

Jordan, T. H., The continental tectosphere, *Rev. Geophys. Space Phys.*, *13*, 1–12, 1975.

Jordan, T. H., and W. S. Lynn, A velocity anomaly in the lower mantle, *J. Geophys Res.*, *79*, 2679–2685, 1974.

Karato, S., Importance of anelasticity in the interpretation of seismic tomography, *Geophys. Res. Lett.*, *20*, 1623–1626, 1993.

Kaula, W. M., Product-sum conversion of spherical harmonics with application to thermal convection, *J. Geophys. Res.*, *80*, 225–231, 1975.

Kawakatsu, H., and F. Niu, Seismic evidence for a 920-km discontinuity in the mantle, *Nature*, *371*, 301–305, 1994.

Kedar, S., D. L. Anderson, and D. J. Stevenson, Relationship between hotspots and mantle structure: Correlation with whole mantle seismic tomography, in *Proceedings of the Nato Advanced Study Institute on Dynamic Modeling and Flow in the Earth and Planets*, edited by D. B. Stone and S. K. Runcorn, pp. 249–259, Kluwer Academic Publisher, 1993.

Kesson, S. E., J. D. F. Gerald, and J. M. G. Shelley, Mineral chemistry and density of subducted basaltic crust at lower-mantle pressures, *Nature*, *372*, 767–769, 1994.

Kido, M., and T. Seno, Dynamic topography compared with residual depth anomalies in oceans and implications for age-depth curves, *Geophys. Res. Lett.*, *21*, 717–720, 1994.

Kind, R., and G. Müller, Computations of SV waves in realistic Earth models, *J. Geophys.*, *41*, 149–172, 1975.

King, S. D., and D. L. Anderson, An alternative mechanism of flood basalt formation, *Earth Planet. Sci. Lett.*, *136*, 269–279, 1995.

King, S. D., and G. Masters, An inversion for radial viscosity structure using seismic tomography, *Geophys. Res. Lett.*, *19*, 1551–1554, 1992.

Kobayashi, Y., Anisotropy of thermal diffusivity in olivine, pyroxene and dunite, *J. Phys. Earth*, *22*, 395–373, 1974.

Lachenbruch, A. H., and J. H. Sass, The stress heat-flow paradox and thermal results from Cajon Pass, *Geophys. Res. Lett.*, *15*, 981–984, 1988.

Landau, L. D., and E. M. Lifshitz, Fluid Mechanics, p. 536, Pergamon, New York, 1959.

Lerch, F. J., S. M. Klosko, R. E. Laubscher, and C. A. Wagner, Gravity improvement using GEOS3 (GEM9 and 10), *J. Geophys. Res.*, *84*, 3897–3916, 1979.

Lerner-Lam, A. L., and T. H. Jordan, How thick are the continents? *J. Geophys. Res.*, *92*, 14007–14026, 1987.

Levander, A. R., Fourth-order finite-difference P-SV seismograms, *Geophysics*, *53*, 1425–1436, 1988.

Lithgow-Bertelloni, C., and M. A. Richards, Cenozoic plate driving forces, *Geophys. Res. Lett.*, *22*, 1317–1320, 1995.

Liu, X.-F., and A. M. Dziewonski, Lowermost mantle shear velocity structure, *Eos Trans. AGU*, *75(44)*, Fall Meet. Supp., 663, 1994.

Liu, X. F., and J. Tromp, Uniformly valid body-wave ray theory, *Geophys. J. Int.*, *127*, 461–491, 1996.

Lysmer, J., and L. A. Drake, A finite element method for seismology, in *Methods in Computational Physics*, edited by B. A. Bolt, vol. 11, pp. 181–216, Academic Press, New York, 1972.

Marsh, J. G., F. J. Lerch, B. H. Putney, T. L. Felsentreger, and B. V. Sanchez, GEM-T2 gravitational model, *J. Geophys. Res.*, *95*, 22043–22071, 1990.

Marty, J. C., and A. Cazenave, Regional variations in subsidence rate of lithospheric plates: Implication for thermal cooling models, *Earth Planet. Sci. Lett.*, *94*, 301–315, 1989.

Masters, G., T. H. Jordan, P. G. Silver, and F. Gilbert, Aspherical earth structure from fundamental spheroidal-mode data, *Nature*, *298*, 609–613, 1982.

Minster, J. B., and T. Jordan, Present-day plate motions, *J. Geophys. Res.*, *83*, 5331–5354, 1978.

Montagner, J.-P., and B. Romanowicz, Degree 2, 4, 6 inferred from seismic tomography, *Geophys. Res. Lett.*, *20*, 631–634, 1993.

Morelli, A., and A. M. Dziewonski, Topography of the core-mantle boundary and lateral heterogeneity of the liquid core, *Nature*, *325*, 678–683, 1987.

Morgan, W. J., Hotspot tracks and the opening of the Atlantic and Indian oceans, in *The Sea*, edited by C. Emiliani, pp. 443–487, Wiley-Interscience, New York, 1981.

Mori, J., and D. V. Helmberger, Localized boundary layer below the mid-Pacific velocity anomaly identified from PcP precursor, *J. Geophys. Res.*, *100*, 20,359–20,365, 1995.

Müller, G., The reflectivity method: a tutorial, *J. Geophys. Res.*, *58*, 153–174, 1985.

Müller, R. D., W. R. Roest, J.-Y. Royer, L. M. Gahagan, and J. G. Sclater, A digital age map of the ocean floor, in *SID Reference Series*, pp. 93–303, Scripps Inst. of Oceanogr., Univ. of Calif., San Diego, La Jolla, 1993.

Nataf, H.-C., I. Nakanishi, and D. L. Anderson, Upper mantle heterogeneity and anisotropy, *J. Geophys. Res.*, *91*, 7261–7307, 1986.

Nataf, H.-C., and Y. Ricard, 3SMAC: An a priori tomographic model of the upper mantle based on geophysical modeling, *Phys. Earth Planet. Int.*, *95*, 101–222, 1996.

Niu, F., and H. Kawakatsu, Depth variation of the mid-mantle seismic discontinuity, *Geophys. Res. Lett.*, *24*, 429–432, 1997.

O'Connell, R. J., C. W. Gable, and B. H. Hager, Toroidal-poloidal partitioning of lithospheric plate motion, in *Glacial Isostasy, Sea Level and Mantle Rheology*, edited by K. L. R. Sabadini and E. Boshci, pp. 513–535, Kluwer, Acad., Norwell, Mass., 1991.

Olsen, P., and D. Bercovici, On the equipartitioning of kinetic energy in plate tectonics, *Geophys. Res. Lett.*, *18*, 1751–1754, 1991.

Olsen, P., G. Schubert, and C. Anderson, Plume formation in the D"-layer and the roughness of the core-mantle boundary, *Nature*, *327*, 409–413, 1987.

Parsons, B. E., and J. G. Sclater, An analysis of the variation of ocean floor bathymetry and heat flow with age, *J. Geophys. Res.*, *82*, 803–827, 1977.

Pekeris, C. L., Thermal convection in the interior of the earth, *Monthly Notices Roy. Astron. Soc., Geophys. Suppl.*, *3*, 343–367, 1935.

Phipps-Morgan, J., and P. M. Shearer, Seismic constraints on mantle flow and topography of the 660 km discontinuity: Evidence for whole mantle convection, *Nature*, *365*, 506–511, 1993.

Phipps-Morgan, J., and P. M. Shearer, Seismic and geoid constraints on mantle flow: Evidence for whole mantle convection, *Unpublished manuscript*, 1994.

Polet, J., and D. L. Anderson, Depth extent of cratons as inferred from tomographic studies, *Geology*, *23*, 205 – 208, 1995.

Ray, T. W., and D. L. Anderson, Spherical disharmonics in the Earth sciences and spatial solution: Ridges, hotspots, slabs, geochemistry and tomography correlations, *J. Geophys. Res.*, pp. 9605–9614, 1994.

Revenaugh, J., and T. H. Jordan, Mantle layering from ScS reverberations: 2 The transition zone, *J. Geophys. Res.*, *96*, 19763–19780, 1991.

Ribe, N., The dynamics of thin shell with variable viscosity and the origin of toroidal flow in the mantle, *Geophys. J. Int.*, *110*, 537–552, 1992.

Ricard, Y., L. Fleitout, and C. Froidevaux, Geoid heights and lithospheric stresses for a dynamic Earth, *Ann. Geophys.*, *2*, 267–286, 1984.

Ricard, Y., C. Froidevaux, and L. Fleitout, Global plate motions and the geoid: A physical model, *Geophys. J. Int.*, *93*, 477–484, 1988.

Ricard, Y., and C. Vigny, Mantle dynamics with induced plate tectonics, *J. Geophys. Res.*, *94*, 17543–17559, 1989.

Ricard, Y., and B. Wuming, Inferring the viscosity and the 3-D density structure of the mantle from the geoid, topography, and plate velocities, *Geophys. J. Int.*, *105*, 561–571, 1991.

Ricard, Y., C. Doglioni, and R. Sabadini, Differential rotation between lithosphere and mantle: A consequence of lateral mantle viscosity variation, *J. Geophys. Res.*, *96*, 8407–8415, 1991.

Ricard, Y., M. A. Richards, C. Lithgow-Bertelloni, and Y. LeStunff, A geodynamic model of mantle density heterogeneity, *J. Geophys. Res.*, *98*, 21895–21909, 1993.

Richards, M. A., and D. C. Engebretson, Large-scale mantle convection and the history of subduction, *Nature*, *335*, 437–440, 1992.

Richards, M. A., and B. H. Hager, Geoid anomalies in a dynamic Earth, *J. Geophys. Res.*, *89*, 5987–6002, 1984.

Richards, M. A., and B. H. Hager, Effects of lateral viscosity variations on long-wavelength geoid anomalies and topography, *J. Geophys. Res.*, *94*, 10299–10313, 1989.

Richards, M. A., B. H. Hager, and N. H. Sleep, Dynamically supported geoid highs over hotspots: observation and theory, *J. Geophys. Res.*, *93*, 7690–7708, 1988.

Richter, F., Dynamic models for sea floor spreading, *Rev. Geophys. Space Phys.*, *11*, 223–287, 1973.

Ritzwoller, M. H., and E. M. Lavely, Three-dimension seismic models of the Earth's mantle, *Rev. Geophys.*, *33*, 1–66, 1995.

Schubert, G., C. Froidevaux, and D. A. Yuen, Oceanic lithosphere and asthenosphere: Thermal and mechanical structure, *J. Geophys. Res.*, *81*, 3525–3540, 1976.

Sclater, J. G., B. Parsons, and C. Jaupart, Oceans and continents: Similarities and differences in the mechanisms of heat loss, *J. Geophys. Res.*, *86*, 11535–11552, 1981.

Scrivner, C., and D. L. Anderson, The effect of post Pangea subduction of global mantle tomography and convection, *Geophys. Res. Lett.*, *19*, 1053–1056, 1992.

Shearer, P. M., and G. Masters, Global mapping of topography on the 660-km discontinuity, *Nature*, *355*, 791–796, 1992.

Shtivelman, V., Two-dimensional acoustic modeling by a hybrid method, *Geophysics*, *50*, 1,273–1,284, 1985.

Song, X. D., and D. V. Helmberger, A P-wave velocity model of Earth's core, *J. Geophys. Res.*, *100*, 9817–9830, 1995a.

Song, X. D., and D. V. Helmberger, Depth dependency of anisotropy of Earth's inner core, *J. Geophys. Res.*, *100*, 9805–9816, 1995b.

Spohn, T., and G. Schubert, Modes of mantle convection and the removal of heat from the Earth's interior, *J. Geophys. Res.*, *87*, 4682–4696, 1982.

Stead, R. J., and D. V. Helmberger, Numerical-analytical interfacing in two dimensions with applications to modeling NTS seismograms, *Pure Appl. Geophys.*, *128*, 153–174, 1988.

Stein, C. A., and S. Stein, A model for the global variation in oceanic depth and heat flow with lithospheric age, *Nature*, *359*, 123–129, 1992.

Stewart, C. A., Thermal convection in the Earth's mantle: Mode coupling induced by temperature-dependent viscosity in a three-dimensional spherical shell, *Geophys. Res. Lett.*, *19*, 337–340, 1992.

Stunff, Y. L., and Y. Ricard, Topography and geoid due to lithosphere mass anomalies, *Geophys. J. Int.*, *122*, 982–990, 1995.

Su, W. J., R. L. Woodward, and A. M. Dziewonski, Degree 12 model of shear velocity heterogeneity in the mantle, *J. Geophys. Res.*, *99*, 6945–6980, 1994.

Tackley, P. J., Effects of strongly temperature-dependent viscosity on time-dependent three-dimensional models of mantle convection, *EOS Trans. AGU*, *74, F(43)*, Fall Meet. Suppl., 79, 1993.

Tackley, P. J., D. J. Stevenson, G. A. Glatzmaier, and G. Schubert, Effects of an endothermic phase transition at 670 km depth in a spherical model of convection in the Earth's mantle, *Nature*, *361*, 699–704, 1993.

Thoraval, C., P. Machetel, and A. Cazenave, Locally layered convection inferred from dynamic models of the Earth's mantle, *Nature*, *375*, 777–779, 1995.

Toksoz, M. N., and D. L. Anderson, Phase velocities of long-period surface waves and structure of the upper mantle, *J. Geophys. Res.*, *71*, 1649–1658, 1966.

Turcotte, D. L., and E. R. Oxburgh, Finite amplitude convective cells and continental drift, *J. Fluid Mech.*, *28*, 29–42, 1967.

van der Hilst, R., Complex morphology of subducted lithosphere in the mantle beneath the Tonga trench, *Nature*, *374*, 154–157, 1995.

van der Hilst, R., R. Engdahl, W. Spakman, and N. Nolet, Tomographic imaging of subducted lithosphere below northwest pacific island arcs, *Nature*, *353*, 37–43, 1991.

Vidale, J. E., and H. M. Benz, A sharp and flat section of the core-mantle boundary, *Nature*, *359*, 627–629, 1992.

Vidale, J. E., and M. Hedlin, Intense scattering at the core-mantle boundary north of Tonga: evidence for partial melt, *Nature*, *submitted*, 1997.

Virieux, J., SH-wave propagation in heterogeneous media: Velocity-stress finite-difference method, *Geophysics*, *49*, 1,933–1,957, 1984.

Virieux, J., P-SV wave propagation in heterogeneous media: Velocity-stress finite-difference method, *Geophysics*, *51*, 889–901, 1986.

Wen, L., and D. L. Anderson, The fate of the slabs inferred from 130 Ma subduction and seismic tomography, *Earth Planet. Sci. Lett.*, *133*, 185–198, 1995.

Wen, L., and D. L. Anderson, Slabs, hotspots, cratons and mantle convection revealed from residual seismic tomography in the upper mantle, *Phys. Earth Planet. Int.*, *99*, 131–143, 1997a.

Wen, L., and D. L. Anderson, Layered mantle convection: A model for geoid and topography, *Earth Planet. Sci. Lett.*, *146*, 367–377, 1997b.

Wen, L., and D. V. Helmberger, Ultra low velocity zones near the core-mantle boundary from broadband PKP precursors, *Science*, *accepted*, 1997.

Wen, L., and D. V. Helmberger, A 2-D P-SV hybrid method and its application to modeling localized structures near the core-mantle boundary, *J. Geophys. Res.*, *in press*, 1998.

Williams, Q., and E. J. Garnero, Seismic evidence for partial melt at the base of Earth's mantle, *Science*, *273*, 1,528–1,530, 1996.

Zhang, S., and U. R. Christensen, Some effects of lateral viscosity variations on geoid and surface velocities induced by density anomalies in the mantle, *Geophys. J. Int.*, *114*, 531–547, 1993.

Zhang, Y. S., and T. Tanimoto, High-resolution global upper mantle structure and plate tectonics, *J. Geophys. Res.*, *98*, 9790–9823, 1993.

Zhong, S., and M. Gurnis, Mantle convection with plates and mobile, faulted plate margins, *Science*, *267*, 838–843, 1995.

Zhong, S., and M. Gurnis, Interaction of weak faults and non-newtonian rheology produces plate tectonics in a 3D model of mantle flow, *Nature*, *385*, 245–247, 1996.

Zhou, H.-W., and D. L. Anderson, Search for deep slabs in the northwest Pacific mantle, *Proc. Natl. Acad. Sci., USA*, *86*, 8602–8606, 1989.

Appendix A Newtonian viscous flow formulations

Viscous flow in a self-gravitating fluid is governed by the equation of continuity, constitutive equations, and the equations of motion. In spherical coordinates, the incompressible equation of continuity can be written [*Landau and Lifshitz*, 1959]:

$$\frac{1}{r^2}\frac{\partial(r^2U_r)}{\partial r}+\frac{1}{r\sin\theta}\frac{\partial(U_\theta\sin\theta)}{\partial\theta}+\frac{1}{r\sin\theta}\frac{\partial U_\phi}{\partial\phi}=0 \tag{A.1}$$

where U_r, U_θ and U_ϕ are three components of velocities in spherical coordinates.

The equations of motion, with variable viscosity, including self-gravitation and neglecting inertial effects, can be written in terms of the components of the deviatoric stress tensor as [*Landau and Lifshitz*, 1959]:

$$\begin{aligned}-\frac{\partial P}{\partial r}+\rho\frac{\partial\Phi}{\partial r}+\frac{1}{r^2}\frac{\partial(r^2\tau_{rr})}{\partial r}+\frac{1}{r\sin\theta}\frac{\partial(\tau_{r\theta}\sin\theta)}{\partial\theta}&\\+\frac{1}{r\sin\theta}\frac{\partial\tau_{r\phi}}{\partial\phi}-\frac{\tau_{\theta\theta}+\tau_{\phi\phi}}{r}-\delta\rho g_0=0&\end{aligned} \tag{A.2}$$

$$\begin{aligned}-\frac{1}{r}\frac{\partial P}{\partial\theta}+\rho\frac{1}{r}\frac{\partial\Phi}{\partial\theta}+\frac{1}{r^2}\frac{\partial(r^2\tau_{r\theta})}{\partial r}+\frac{1}{r\sin\theta}\frac{\partial(\tau_{\theta\theta}\sin\theta)}{\partial\theta}&\\+\frac{1}{r\sin\theta}\frac{\partial\tau_{\theta\phi}}{\partial\phi}+\frac{\tau_{r\theta}}{r}-\frac{\cot\theta\tau_{\phi\phi}}{r}=0&\end{aligned} \tag{A.3}$$

$$\begin{aligned}-\frac{1}{r\sin\theta}\frac{\partial P}{\partial\phi}+\rho\frac{1}{r\sin\theta}\frac{\partial\Phi}{\partial\phi}+\frac{1}{r^2}\frac{\partial(r^2\tau_{r\phi})}{\partial r}+\frac{1}{r}\frac{\partial(\tau_{\theta\phi})}{\partial\theta}&\\+\frac{1}{r\sin\theta}\frac{\partial\tau_{\phi\phi}}{\partial\phi}+\frac{\tau_{r\phi}}{r}+\frac{2\cot\theta\tau_{\theta\phi}}{r}=0&\end{aligned} \tag{A.4}$$

where P is pressure, Φ is the perturbation of the gravitational potential, g_0 is gravitational acceleration, τ is the deviatoric stress tensor and $\delta\rho$ is the density perturbation.

The constitutive relationship between stress and velocities for a Newtonian fluid is:

$$\tau_{r\theta} = \eta(-\frac{U_\theta}{r} + \frac{\partial U_\theta}{\partial r} + \frac{1}{r}\frac{\partial U_r}{\partial\theta}) \tag{A.5}$$

$$\tau_{r\phi} = \eta(-\frac{U_\phi}{r} + \frac{\partial U_\phi}{\partial r} + \frac{1}{r\sin\theta}\frac{\partial U_r}{\partial\phi}) \tag{A.6}$$

$$\tau_{rr} = 2\eta\frac{\partial U_r}{\partial r} \tag{A.7}$$

$$\tau_{\theta\theta} = 2\eta(\frac{1}{r}\frac{\partial U_\theta}{\partial\theta} + \frac{U_r}{r}) \tag{A.8}$$

$$\tau_{\phi\phi} = 2\eta(\frac{1}{r\sin\theta}\frac{\partial U_\phi}{\partial\phi} + \frac{U_r}{r} + \frac{U_\theta\cot\theta}{r}) \tag{A.9}$$

$$\tau_{\theta\phi} = \eta(-\frac{\cot\theta U_\phi}{r} + \frac{1}{r}\frac{\partial U_\phi}{\partial\theta} + \frac{1}{r\sin\theta}\frac{\partial U_\theta}{\partial\phi}) \tag{A.10}$$

where $\eta = \eta(\theta, \phi)$ is the viscosity.

The three components of velocity and components of non-hydrostatic stress can be expressed as infinite series in terms of spherical harmonics $Y_{lm}(\theta, \phi)$:

$$U_r = Z_1^{lm} Y_{lm}(\theta, \phi) \tag{A.11}$$

$$U_\theta = Z_2^{lm} Y_{lm}^{10}(\theta, \phi) + Z_5^{lm} Y_{lm}^{01}(\theta, \phi) \tag{A.12}$$

$$U_\phi = Z_2^{lm} Y_{lm}^{01}(\theta, \phi) - Z_5^{lm} Y_{lm}^{10}(\theta, \phi) \tag{A.13}$$

$$r(-P + \tau_{rr} + \rho\Phi)/\eta_0 = Z_3^{lm} Y_{lm}(\theta, \phi) \tag{A.14}$$

$$r(\tau_{r\theta})/\eta_0 = Z_4^{lm} Y_{lm}^{10}(\theta, \phi) + Z_6^{lm} Y_{lm}^{01}(\theta, \phi) \tag{A.15}$$

$$r(\tau_{r\phi})/\eta_0 = Z_4^{lm} Y_{lm}^{01}(\theta, \phi) - Z_6^{lm} Y_{lm}^{10}(\theta, \phi) \tag{A.16}$$

where Z_2^{lm} and Z_4^{lm} are the poloidal components of velocity and stress and Z_5^{lm} and Z_6^{lm} are the toroidal components of velocity and stress. Einstein summation convention is used and

$$Y_{lm}^{10}(\theta,\phi) = \frac{\partial Y_{lm}(\theta,\phi)}{\partial\theta}$$

$$Y_{lm}^{01}(\theta,\phi) = \frac{1}{\sin\theta}\frac{\partial Y_{lm}(\theta,\phi)}{\partial\phi}$$

Substituting equations (A.11)-(A.16) into (A.1)-(A.6) and taking each spherical harmonic by using the orthogonalities, after tedious algebra, we have following equations:

$$\begin{aligned}
\frac{\partial Z_1^{lm}}{\partial\mu} &= -2Z_1^{lm} + LZ_2^{lm} && \text{(A.17)}\\
\frac{\partial Z_2^{lm}}{\partial\mu} &= -Z_1^{lm} + Z_2^{lm} + 1/\eta^* A_{lml'm'} Z_4^{l'm'} \\
&\quad +1/\eta^* B_{lml'm'} Z_6^{l'm'} && \text{(A.18)}\\
\frac{\partial Z_3^{lm}}{\partial\mu} &= 12\eta^* C_{lml'm'} Z_1^{l'm'} - 6L'\eta^* C_{lml'm'} Z_2^{l'm'} \\
&\quad +Z_3^{lm} + LZ_4^{lm} + r^2\delta\rho^{lm} g_0/\eta_0 && \text{(A.19)}\\
\frac{\partial Z_4^{lm}}{\partial\mu} &= -2Z_4^{lm} - Z_3^{lm} - 6\eta^* C_{lml'm'} Z_1^{l'm'} \\
&\quad +\eta^* D_{lml'm'} Z_2^{l'm'} + \eta^* E_{lml'm'} Z_5^{l'm'} && \text{(A.20)}\\
\frac{\partial Z_5^{lm}}{\partial\mu} &= Z_5^{lm} - 1/\eta^* B_{lml'm'} Z_4^{l'm'} \\
&\quad +1/\eta^* A_{lml'm'} Z_6^{l'm'} && \text{(A.21)}\\
\frac{\partial Z_6^{lm}}{\partial\mu} &= -2Z_6^{lm} - \eta^* F_{lml'm'} Z_2^{l'm'} \\
&\quad +\eta^* G_{lml'm'} Z_5^{l'm'} && \text{(A.22)}
\end{aligned}$$

$$\begin{aligned}
A_{lml'm'} &= \frac{1}{L}\int\int \frac{1}{T(\theta,\phi)}(Y_{l'm'}^{10}(\theta,\phi)Y_{lm}^{*10}(\theta,\phi) \\
&\quad +Y_{l'm'}^{01}(\theta,\phi)Y_{lm}^{*01}(\theta,\phi)) * ds \\
B_{lml'm'} &= \frac{1}{L}\int\int \frac{1}{T(\theta,\phi)}(Y_{l'm'}^{01}(\theta,\phi)Y_{lm}^{*10}(\theta,\phi) \\
&\quad -Y_{l'm'}^{10}(\theta,\phi)Y_{lm}^{*01}(\theta,\phi)) * ds \\
C_{lml'm'} &= \int\int (T(\theta,\phi)Y_{l'm'}(\theta,\phi)Y_{lm}^{*}(\theta,\phi)) * ds
\end{aligned}$$

$$\begin{aligned}
D_{lml'm'} &= 2 * A1 + 4L'C_{lml'm'} \\
E_{lml'm'} &= \frac{1}{L}(\int\int 2T(\theta,\phi)(L'Y_{l'm'}(\theta,\phi) \\
&\quad +2Y^{20}_{l'm'}(\theta,\phi)) * (\cot\theta Y^{*01}_{lm}(\theta,\phi) - Y^{*11}_{lm}(\theta,\phi)) \\
&\quad -(\cot\theta Y^{01}_{l'm'}(\theta,\phi) - Y^{11}_{l'm'}(\theta,\phi)) * (LY^{*}_{lm}(\theta,\phi) \\
&\quad +2Y^{*20}_{lm}(\theta,\phi)) * ds \\
F_{lml'm'} &= E_{lml'm'} \\
G_{lml'm'} &= 2 * A1 + L'C_{lml'm'}
\end{aligned}$$

$$\begin{aligned}
A1 &= \frac{1}{L}(\int\int T(\theta,\phi)(L'Y_{l'm'}(\theta,\phi)Y^{*20}_{lm}(\theta,\phi) + L \\
&\quad Y^{20}_{l'm'}(\theta,\phi)Y^{*}_{lm}(\theta,\phi) + 2Y^{20}_{l'm'}(\theta,\phi)Y^{*20}_{lm}(\theta,\phi) * ds \\
&\quad + \int\int 2T(\theta,\phi)(Y^{11}_{l'm'}(\theta,\phi) - \cot\theta Y^{01}_{l'm'}(\theta,\phi)) \\
&\quad *(Y^{*11}_{lm}(\theta,\phi) - \cot\theta Y^{*01}_{lm}(\theta,\phi)) * ds
\end{aligned}$$

where

$$T(\theta,\phi) = \eta(\theta,\phi)/\overline{\eta}$$

$$\eta^{*} = \overline{\eta}/\eta_0$$

$$L = l(l+1)$$

$$L' = l'(l'+1)$$

$$\mu = \ln(\frac{r}{a})$$

η_0 is the reference viscosity, $\overline{\eta}$ is the average viscosity in the shell and a is the radius of the Earth. Equation (A.17) is derived from the continuity equation (A.1); equations (A.18) and (A.21) come from constitutive relationship equations (A.5) (A.6); equations (A.19) comes from momentum equation (A.2) and equations (A.20) (A.22) come from momentum equations (A.3) (A.4). Again Einstein summation convention is used.

Note that for a spherical shell with no lateral variation in viscosity, $T(\theta, \phi) = 1$, the coefficients $B_{lml'm'} = E_{lml'm'} = F_{lml'm'} = 0$, $A_{lml'm'} = C_{lml'm'} = \delta_{ll'}\delta_{mm'}$, $A1 = -\delta_{ll'}\delta_{mm'}$. The above equations are simplified to the identical equations in a radially symmetric structure [*Kaula*, 1975]. In that case, equations for each spherical harmonic are independent with those in other harmonics and they can be solved degree by degree.

For spherical shells with lateral variations in viscosity, the above equations are no longer separated by each mode, i.e., modes are coupled with each other through those coupling coefficients $A_{lml'm'} - G_{lml'm'}$. Since the above summations go to infinity, we have no obvious way to solve these equations. However, if we truncate all the quantities up to a spherical harmonic degree (l_{max}), i.e., we neglect the coupling effects of spherical harmonic degrees $l > l_{max}$, we have these linear equations by putting all the equations at degrees $l = 1 - l_{max}$ together.

$$\frac{dZ}{d\mu} = B * Z + b; \tag{A.23}$$

where

$$Z = [Z_1^{10} ... Z_6^{10}, ..., Z_1^{lm} ... Z_6^{lm}]^T \tag{A.24}$$

$$b = [0, 0, r^2 g \delta\rho^{10}/\eta_0, 0, 0, 0..., 0, 0, r^2 g \delta\rho^{lm}/\eta_0, 0, 0, 0]^T \tag{A.25}$$

and B is a $3l_{max}(l_{max} + 3) \times 3l_{lmax}(l_{lmax} + 3)$ matrix with elements given by equations (A.17)-(A.22).

A.1 Propagator matrix method

In a shell, with same lateral variation in viscosity, the elements in B are constants. Equation (A.23) can be solved by standard propagator matrix method. The solution of equation (A.23) is

$$\begin{aligned} Z(\mu) &= \exp[B(\mu-\mu_0)]Z(\mu_0) + \int_{\mu_0}^{\mu} \exp[B(\mu-\epsilon)]b(\epsilon)d\epsilon \\ &= P_B(\mu,\mu_0)Z(\mu_0) + \int_{\mu_0}^{\mu} P_B(\mu,\epsilon)b(\epsilon)d\epsilon \end{aligned} \tag{A.26}$$

The analysis can be simplified if $\delta\rho^{lm}(r)$ is approximated as a series of J discrete sheets or surface anomalies [*Hager and Clayton*, 1989].

$$\sigma_j^{lm} = \sum_{r_j-\epsilon}^{r_j+\epsilon} \delta\rho^{lm}(r)dr$$

Analogous to equation (4.40) in *Hager and Clayton* [1989], (A.26) becomes

$$Z(\mu) = P_B(\mu,\mu_0)Z(\mu_0) + \sum_{j=1}^{J} P_B(\mu,\epsilon)b_j \tag{A.27}$$

where

$$b_j = [0,0,rg\sigma_j^{lm}/\eta_0,0,0,0,...0,0,rg\sigma_j^{lm}/\eta_0,0,0,0]^T \tag{A.28}$$

The form of the propagator matrix P_B can be estimated in terms of its eigenvalues λ_i of matrix B. For example, for a matrix B with no repeated eigenvalues, the propagator matrix P_B is given by [*Gantmacher*, 1960]:

$$P_B = \sum_{i=1} \exp[\lambda_i(\mu-\mu_0)] \prod_{s\neq i} (\lambda_s I - B)/(\lambda_s - \lambda_i) \tag{A.29}$$

where I is the identity matrix.

When the dimension of matrix B is large, the above method is not practical, since it involves many matrix multiplications.

When the thickness of the shell is small, P_B can be obtained directly from its definition with some approximations.

$$\begin{aligned} P_B(\mu, \mu_0) &= \exp[B(\mu - \mu_0)] \\ &= I + \sum_{n=1}^{n=N} \frac{(\mu - \mu_0)^n}{n!} B^n \end{aligned} \tag{A.30}$$

N is the truncated power. Numerical tests indicate that, for a shell with thickness of 20 km, P_B can be obtained within an error of 0.001% with $N = 4$.

A.2 Boundary conditions

Velocities (U_r, U_θ, U_ϕ), stresses $(\tau_{rr}, \tau_{r\theta}, \tau_{r\phi})$ and Φ are continuous at any boundary in the mantle, i.e., Z is continuous across any boundary. For boundary between layers with different viscosity but same intrinsic density, Z is continuous; for boundary in which intrinsic density changes (chemical boundary) and stratification of flow occurs, $Z_1^{lm} = 0$ $(U_r = 0)$, Z_3^{lm} has a jump of dZ_3^{lm}.

Shear tractions and vertical velocities at the CMB and surface are zero, simply because the viscosities in the atmosphere and core are negligible compared to that of the mantle. At the CMB,

$$\begin{aligned} Z(1) = [\quad & 0, Z_2^{10}(1), Z_3^{10}(1), 0, Z_5^{10}(1), 0, \ ..., \\ & 0, Z_2^{lm}(1), Z_3^{lm}(1), 0, Z_5^{lm}(1), 0]^T \end{aligned} \tag{A.31}$$

$Z(1)$ is propagated to the surface of Earth by propagator matrices. At the surface of Earth, we have the boundary condition:

$$\begin{aligned} Z(0) = [\quad & 0, Z_2^{10}(0), Z_3^{10}(0), 0, Z_5^{10}(0), 0, \ ..., \\ & 0, Z_2^{lm}(0), Z_3^{lm}(0), 0, Z_5^{lm}(0), 0]^T \end{aligned} \tag{A.32}$$

There are $3l_{max}(l_{max}+1)$ unknowns and $3l_{max}(l_{max}+1)$ linear equations for whole mantle flow, $7l_{lmax}(l_{max}+1)/2$ unknowns (one more (dZ_3^{lm}) for each spherical harmonic degree and order) and $7l_{max}(l_{max}+1)/2$ linear equations (one more $(U_r = 0)$ across the chemical boundary for each spherical harmonic degree and order) for layered flow.

Appendix B Finite difference formulations in the interfaces of three defined regions

We follow the notation of [*Virieux*, 1986]. For region, where n = 3 and m > 3:

$$
\begin{aligned}
U_{i,j}^{k+1/2} &= U_{i,j}^{k-1/2} + B_{i,j}[(\Sigma^{k}_{i+1/2,j} - \Sigma^{k}_{i-1/2,j}) \\
&\quad +((\Xi^{k}_{i,j+1/2} + \Xi^{0,k}_{i,j+1/2}) - \Xi^{k}_{i,j-1/2})], \\
V^{k+1/2}_{i+1/2,j+1/2} &= V^{k-1/2}_{i+1/2,j+1/2} + B_{i+1/2,j+1/2}[(\Xi^{k}_{i+1,j+1/2} \\
&\quad -\Xi^{k}_{i,j+1/2}) + (\Gamma^{k}_{i+1/2,j+1} - (\Gamma^{k}_{i+1/2,j} \\
&\quad -\Gamma^{0,k}_{i+1/2,k}))], \\
\Sigma^{k+1}_{i+1/2,j} &= \Sigma^{k}_{i+1/2,j} + (L+2M)_{i+1/2,j}(U^{k+1/2}_{i+1,j} \\
&\quad -U^{k+1/2}_{i,j}) + L_{i+1/2,j}((V^{k+1/2}_{i+1/2,j+1/2} \\
&\quad +V^{0,k}_{i+1/2,j+1/2}) - V^{k}_{i+1/2,j-1/2}), \\
\Gamma^{k+1}_{i+1/2,j} &= \Gamma^{k}_{i+1/2,j} + L_{i+1/2,j}(U^{k+1/2}_{i+1,j} - U^{k+1/2}_{i,j}) \\
&\quad +(L+2M)_{i+1/2,j}((V^{k+1/2}_{i+1/2,j+1/2} \\
&\quad +V^{0,k}_{i+1/2,j+1/2}) - V^{k}_{i+1/2,j-1/2}), \\
\Xi^{k+1}_{i,j+1/2} &= \Xi^{k}_{i,j+1/2} + M_{i,j+1/2}[((U^{k+1/2}_{i,j+1} \\
&\quad -U^{0,k+1/2}_{i,j+1}) - U^{k+1/2}_{i,j}) + (V^{k+1/2}_{i+1/2,j+1/2} \\
&\quad -V^{k}_{i-1/2,j+1/2})].
\end{aligned}
$$

Where k is the index of time steps, i and j are for x-axis and z-axis discretizations. $(U, V) = (u_x, u_z)$, $(\Sigma, \Gamma, \Xi) = (\tau_{xx}, \tau_{zz}, \tau_{xz})$, $L = \lambda * \frac{dt}{dx}, M = \mu * \frac{dt}{dx}$ and $B = \frac{1}{\rho} * \frac{dt}{dx}$. dx and dt are space and time discretizations and λ, μ are Lamb's parameters. $(U^0, V^0, \Sigma^0, \Gamma^0, \Xi^0)$ are solutions for the direct incident wave (I_0). Here, the relationship $T = I_0 + R$ is used.

For the left boundary, m=3:

$$\begin{aligned}
U^{k+1/2}_{i,j} &= U^{k-1/2}_{i,j} + B_{i,j}[((\Sigma^{k}_{i+1/2,j} - \Sigma^{0,k}_{i+1/2,j}) \\
&\quad -\Sigma^{k}_{i-1/2,j}) + (\Xi^{k}_{i,j+1/2} - \Xi^{k}_{i,j-1/2})], \\
V^{k+1/2}_{i+1/2,j+1/2} &= V^{k-1/2}_{i+1/2,j+1/2} + B_{i+1/2,j+1/2}[(\Xi^{k}_{i+1,j+1/2} \\
&\quad -(\Xi^{k}_{i,j+1/2} + \Xi^{0,k}_{i,j+1/2})) + (\Gamma^{k}_{i+1/2,j+1} \\
&\quad -\Gamma^{k}_{i+1/2,j})], \\
\Sigma^{k+1}_{i+1/2,j} &= \Sigma^{k}_{i+1/2,j} + (L+2M)_{i+1/2,j}(U^{k+1/2}_{i+1,j} \\
&\quad -(U^{k+1/2}_{i,j} + U^{0,k+1/2}_{i,j})) + L_{i+1/2,j} \\
&\quad (V^{k+1/2}_{i+1/2,j+1/2} - V^{k}_{i+1/2,j-1/2}), \\
\Gamma^{k+1}_{i+1/2,j} &= \Gamma^{k}_{i+1/2,j} + L_{i+1/2,j}(U^{k+1/2}_{i+1,j} - (U^{k+1/2}_{i,j} \\
&\quad +U^{0,k+1/2}_{i,j})) + (L+2M)_{i+1/2,j} \\
&\quad (V^{k+1/2}_{i+1/2,j+1/2} - V^{k}_{i+1/2,j-1/2}), \\
\Xi^{k+1}_{i,j+1/2} &= \Xi^{k}_{i,j+1/2} + M_{i,j+1/2}[(U^{k+1/2}_{i,j+1} - U^{k+1/2}_{i,j}) \\
&\quad +((V^{k+1/2}_{i+1/2,j+1/2} - V^{0,k+1/2}_{i+1/2,j+1/2}) \\
&\quad -V^{k}_{i-1/2,j+1/2})].
\end{aligned}$$

Where $(U^0, V^0, \Sigma^0, \Gamma^0, \Xi^0)$ are solutions for whole wavefield (T_0) due to one-dimensional structure for grids n $>$ 3 and reflected wave field (R_0) for grids n $<$ 3. Here, the relationships $S = T - T_0$ and $S = R - R_0$ are used.

Special treatment is needed for the triple junction point (m = 3, n = 3) of those three regions:

$$\begin{aligned}
V^{k+1/2}_{i+1/2,j+1/2} &= V^{k-1/2}_{i+1/2,j+1/2} + B_{i+1/2,j+1/2}[(\Xi^{k}_{i+1,j+1/2} \\
&\quad -(\Xi^{k}_{i,j+1/2} + \Xi^{0,k}_{i,j+1/2}) + ((\Gamma^{k}_{i+1/2,j+1} \\
&\quad -\Gamma^{0,k}_{i+1/2,j+1}) - \Gamma^{k}_{i+1/2,j})], \\
\Sigma^{k+1}_{i+1/2,j} &= \Sigma^{k}_{i+1/2,j} + (L+2M)_{i+1/2,j}(U^{k+1/2}_{i+1,j} \\
&\quad -(U^{k+1/2}_{i,j} + U^{0,k+1/2}_{i,j})) + L_{i+1/2,j} \\
&\quad (V^{k+1/2}_{i+1/2,j+1/2} - (V^{k}_{i+1/2,j-1/2} \\
&\quad +V^{0,k}_{i+1/2,j-1/2})), \\
\Gamma^{k+1}_{i+1/2,j} &= \Gamma^{k}_{i+1/2,j} + L_{i+1/2,j}(U^{k+1/2}_{i+1,j} - (U^{k+1/2}_{i,j} \\
&\quad +U^{0,k+1/2}_{i,j})) + (L+2M)_{i+1/2,j} \\
&\quad (V^{k+1/2}_{i+1/2,j+1/2} - (V^{k}_{i+1/2,j-1/2} \\
&\quad +V^{0,k}_{i+1/2,j-1/2})),
\end{aligned}$$

Where (V^0, Γ^0) are the solutions for the direct wave (I_0), (U^0) is the solution of T_0, and (Ξ^0) is the solution of R_0. $\Xi^k_{3,3-1/2}$ can be calculated as those in n < 3 and $U^k_{3,3}$ can be calculated as those in n > 3.